Politecnico di Milano

Dipartimento di Fisica

Nonlinear Light-Matter Interactions in Lead Halide Perovskites and the Role of Crystal Structure

Doctoral Dissertation of:

Stefanie Claudia Neutzner

Supervisor:

Dr. Annamaria Petrozza

Tutor:

Prof. Guglielmo Lanzani

Chair of the Doctoral Program:

Prof. Paola Taroni

Doctoral Program in Physics

2018 - XXXth Cycle

Contents

List of Figures

List of Tables

Abbreviations

1Q	One-Quantum.
2Q	Two-Quantum.
ASE	Amplified Spontaneous Emission.
BBO	Barium Borate.
BoxCARS	Box-Coherent Anti-Stokes Raman Scattering.
CBM	Conduction Band Minimum.
CCD	Charged Coupled Device.
CFROG	Collinear Frequency Resolved Optical Gating.
COLBERT	Coherent Optical Laser BEam Recombination Technique.
DFT	Density Functional Theory.
DMF	N,N-Dimethylformamide.
DMSO	Dimethyl-Sulfoxide.
DOE	Diffractive Optical Element.
ECPL	Excitation Correlation Photoluminescence.
EDBE	2,2'-(Ethylenedioxy)bis(ethylammonium).
EHP	Electron-Hole Plasma.
ESA	Excited-State Absorption.
FA	Formamidinium.
FE	Free Exciton.
FET	Field-Effect Transistor.
FWHM	Full Width at Half Maximum.
FWM	Four-Wave-Mixing.
GDD	Group Delay Dispersion.
GSB	Ground State Bleach.
HOIP	Hybrid Organic-Inorganic Perovskite.
HOMO	Highest Occupied Molecular Orbital.

JDOS	Joint Density of States.
LED	Light-Emitting Device.
LO	Longitudinal Optical.
LUMO	Lowest Unoccupied Molecular Orbital.
MA	Methylammonium.
NBT	N-Butyl-ethylammonium.
NCs	Nanocrystals.
NMR	Nuclear Magnetic Resonance.
NOPA	Nonlinear Optical Parametric Amplifier.
OPA	Optical Parametric Amplifier.
PCE	Power Conversion Efficiency.
PEA	Phenylethylammonium.
PIA	Photo-Induced Absorption.
PL	Photoluminescence.
PLQY	Photoluminescence Quantum Yield.
PMMA	Poly-Methyl-Methacrylate.
PV	Photovoltaic.
SE	Stimulated Emission.
SHG	Second Harmonic Generation.
SLM	Spatial Light Modulator.
SNR	Signal-to-Noise Ratio.
SOC	Spin Orbit Coupling.
SRH	Shockley-Read-Hall.
STE	Self-Trapped Exciton.
TA	Transient Absorption.
TO	Transversal Optical.
TRPL	Time Resolved Photoluminescence.
VBM	Valence Band Maximum.
WAXS	Wide-Angle X-ray Scattering.
XRD	X-Ray Diffraction.

Preface

Semiconductors are the building blocks of the current technological development, influencing practically all aspects of our modern society. Their success is based on their diversity and therefore the potential to engineer their opto-electronic and structural properties. Perpetual progress allows miniaturization of semiconductor based devices down to the quantum mechanical limit and their electro-optical peculiarities advance a vast variety of applications affecting our daily life, starting from computer chips, renewable energy sources, display technologies, solid state lighting up to telecommunication.

Technological advances demand for abundant, low cost and easy to process materials. In several technological fields, organic semiconductors started to supersede inorganic materials, due to excellent luminescence properties, low temperature processability and flexibility of their chemistry allowing easy adjustment of the material to meet certain requirements. On the other hand, they exhibit several drawbacks, including poor thermal and mechanical stability and restricted carrier mobilities at room temperature, due to weak van der Waals interactions between the molecules. In the effort to overcome these limitations and to combine the desired characteristics of organic and inorganic materials in a single molecular-scale compound, hybrid semiconductors have been extensively studied with the goal to compose materials with superior electro-optic properties. One class of hybrid materials in particular, the hybrid lead halide perovskites have drawn global attention of the scientific community by virtue of their success as active material in photovoltaic devices, with performances exceeding 20 % and demonstrations of perovskite based electroluminescent and lasing devices.

This class of materials can be self assembled by simple chemical deposition of the constituent compounds which permits fine-tuning of the electro-optical properties, promising for a broad variety of applications. Nevertheless, several challenges have to be addressed to exploit their full potential. Owing to their nature of forming a relatively soft ionic crystal structure, hybrid perovskites are intrinsically complex systems and extremely sensitive to processing parameters. Structural disorder, various interactions between the organic and inorganic constituents and the resulting rich defect landscape affect charge transport and excitonic effects and determine their distinct electro-optical properties. Detailed understanding of the structure-function relationship in these materials is essential to disentangle the different contributions, gain full control to engineer their properties and to expedite perovskite based technologies. In contrast to the rapid improvements in the field of photovoltaics, fundamental research lags behind and a complete picture of the complex photophysics in these materials is still missing. In the present thesis we investigate the light-matter interaction of hybrid perovskites using a variety of non-

linear spectroscopic methods with the objective to expand the photophysical understanding towards the impact of structure and to provide useful information for further material optimization and engineering. The work can be divided into two parts:

i Ultrafast dynamics and optical nonlinearities in three dimensional hybrid lead halide perovskites

ii The role of crystal structure in two dimensional lead halide perovskites and excitonic many body effects

The main parts are summarized as followed.

1. **Nonlinearities in the light emission characteristics of lead halide perovskites and the role of defects**

   Non-radiative processes like carrier trapping within intra-gap defect states or multiparticle Auger recombination form the dominant loss-channels in optoelectronic materials limiting photovoltaic and light emission efficiencies and result in nonlinearities in the photoluminescence characteristics of a material. We use Excitation Correlation Photo-Luminescence (ECPL) spectroscopy to study representative lead bromide perovskite systems exhibiting different photoluminescence efficiencies. In contrast to traditional transient photoluminescence spectroscopy, we excite the materials with two pump beams, modulated at different frequencies and use a heterodyne detection scheme to extract exclusively the nonlinear part of the photoluminescence due to population mixing. We exploit the superior sensitivity of this method to identify the nature and energetics of trap states in lead bromide perovskites and to complement the Shockley-Read Hall formalism currently employed to describe the carrier dynamics in these materials. The technique directly reveals the thresholds between different competing nonlinear processes and constitutes a valuable tool to provide guidelines for material engineering.

2. **Ultrafast dynamics and amplified spontaneous emission at the structural phase transition of hybrid lead iodide perovskites**

   In this part we specifically address the high excitation density regime in lead iodide perovskites. Polycrystalline $MAPbI_3$ films undergo an incomplete structural phase transition from the tetragonal to orthorhombic crystal structure at low temperatures, leading to a temperature dependent distribution of small tetragonal inclusions within the orthorhombic phase. Although the absorption is dominated by the orthorhombic band edge, the material exhibits an unusual red shifted emission, spectrally located at the position of the room temperature phase. Using transient absorption spectroscopy, we assign this emission behaviour to excitation transfer between the two crystal phases whose dynamics depend on the relative distribution and domain sizes of the tetragonal inclusions.

We demonstrate, that efficient transfer can lower the threshold for amplified spontaneous emission in the material from which we deduce design principles for mixed phase architectures to tackle the problem of Auger recombination and to suggest materials for lasing applications.

3. **The role of crystal structure in the optical properties and excitonic many-body effects in two dimensional lead-halide perovskites**

Electro-optical properties of materials are inherently linked to the symmetry and dimensionality of a material system. Excitons in two dimensional semiconductors are strongly bound and exhibit a broad variety of physical phenomena promising for quantum optoelectronics. Two dimensional layered perovskites form a subclass in the perovskite family and self-assemble in a multiple quantum well like configuration, resulting in charge confinement within the inorganic layers and high exciton binding energies. Consequently, these materials usually show the narrowband finger print of free exciton absorption and emission. Nevertheless, a small group of them feature broad photoluminescence bands, and some compounds develop a distinct excitonic fine structure at low temperatures. To shed light on the underlying mechanisms of these peculiar optical characteristics we use a combination of structural and optical probes to study three structurally different compounds, (EDBE)PbI_4, $(NBT)_2PbI_4$ and $(PEA)_2PbI_4$ showing broad and narrow-band emission, and a pronounced excitonic fine structure respectively. We demonstrate that these optical effects are closely linked to the intrinsic crystal structure. Deformations of the inorganic cage induced by the self-organization of the organic cation within the crystal lattice result in deactivated Raman modes in the system and affect defectivity and charge localization energy, causing the broad photoluminescence features. We show that the excitonic fine structure is influenced by strong polaronic effects and discuss possible origins leading to a reduction of crystal symmetry. Using two dimensional coherent spectroscopy, a technique with superior spectral and time resolution with respect to more conventional transient absorption spectroscopy, we provide evidence for the presence of this fine-structure even at room temperature and investigate the influence of lattice deformations and structural disorder on the excitonic many-body effects in these materials. We provide the first direct observation of stable biexcitons in $(PEA)_2PbI_4$ and point out the influence of lattice fluctuations and induced disorder on many-body effects, which are of paramount importance for the mechanisms of photonic or polaritonic lasing and therefore to advance hybrid perovskites towards progressive technologies.

Summary

Understanding the underlying photophysical processes describing the structure-function relationship in hybrid lead halide perovskites is of fundamental importance to control and engineer their opto-electronic properties for advanced technologies. This dissertation aims to elucidate aspects of the light-matter interaction based on the lattice structure of these complex material systems using a variety of time resolved non-linear and linear spectroscopic techniques.

The PhD thesis describes the research activity carried out by the author between 2014 and 2017 at the Center for Nanoscience and Technology. The presented work was predominantly performed by the author, unless otherwise stated and is structured as follows:

Chapter 1 outlines the contextual and theoretical framework to interpret the results of the thesis. We present the basic concepts of light-matter interaction in semiconductors with focus on their relevance to understand the photophysics of hybrid lead halide perovskites.

Chapter 2 provides an overview of the experimental techniques used with a short theoretical introduction into the spectroscopic methods of this thesis, including a brief description of the employed spectroscopic equipment and a summary of sample fabrication.

Chapter 3 describes the experimental results on the excited state dynamics of three exemplary lead bromide perovskite systems using excitation correlation photoluminescence spectroscopy, a technique, particularly sensitive to the nonlinear part of the photoluminescence. We give evidence for the existence of different predominant defect types depending on the synthesis route in the material, present a refinement of existing photophysical models and report about a correlated carrier regime at high excitation densities.

Chapter 4 presents an investigation of the photo-physics at the structural phase transition of methylammonium lead iodide ($MAPbI_3$) using femtosecond transient absorption spectroscopy. A short introduction into the key concepts of the particular transition and current understanding of its photo-physics is given, followed by investigations of the emission behaviour at high excitation densities. We demonstrate experimental evidence of a lowered threshold for spontaneous amplified emission at the phase transition of the material due to

transfer between the two structural phases and suggest design principles for potential lasing architectures in this material class.

Chapter 5 deals mainly with a subclass of hybrid lead halide perovskites, the so called Ruddlesden Popper lead halide perovskites and can be divided into two parts. First, we investigate the structure-function relationship in this class of materials using a combination of optical and structural spectroscopic techniques. Based on steady state measurements and Raman spectroscopy, we demonstrate that the organic cation can strongly deform the lead-halide octahedra, therefore hampering specific vibrational modes of the inorganic framework and influencing the defect landscape in the material, leading to white light emission in heavily distorted compounds. Additionally, we show that this class of materials develops an exciton fine structure at low temperatures and we discuss possible origins of this phenomenon. Finally, we present a two-dimensional spectroscopic study on the compound phenylethylammonium lead iodide ($(PEA)_2PbI_4$), which was carried out in collaboration with the group of Prof. Carlos Silva of the University of Montreal. We give evidence for the underlying fine-structure even at room temperature and elucidate multi-exciton interactions in the material.

Chapter 1

Introduction

The first publication on organic-inorganic perovskites dates over a century back [1] and further work on this group of materials remained scarce for decades [2]. As a matter of fact, almost 100 years later, in 1978, Weber [3] presented early work on methyl-ammonium (MA) based lead perovskites, followed by several publications on variations of the employed metal cation [4, 5]. Particular interest in this class of materials started to grow at the end of the previous century, addressing mainly the two-dimensional layered counterpart of the three-dimensional parent [6–11] and demonstrating its suitability for optoelectronic applications, notably light-emitting device (LED) [12, 13] and field effect transistor (FET) operation [14, 15].

The success story of hybrid perovskites began with their discovery for photovoltaic applications in 2006 [16]. Kojima *et al.* deposited $MAPbBr_3$ as sensitizer on a mesoporous titania layer in a dye sensitized solar cell structure (DSSC). Despite a low power conversion efficiency (PCE) ($\sim$ 2%), the obtained photovoltage was promising and encouraged further studies on DSSC architectures (e. g. [17–20]). In 2012, Snaith and coworkers demonstrated, that the device still works when substituting the electron transport material TiO_2 with an aluminum dioxide (Al_2O_3) scaffold [21], preventing electron injection. A PCE of 10.9% evidenced that hybrid lead halide perovskites can not only generate electron-hole pairs but also efficiently transport them and within just five years, solar cell efficiencies were surpassing 20% [22].

Despite the rapid progress of the technology, we still lack a comprehensive understanding of the photophysics of these materials and results often seem to be ambiguous or even contradictory. Especially one of the most compelling aspects of hybrid perovskites, the possibility of simple and cheap fabrication by solution processing [23] exposes the material to a multitude of external factors, influencing the crystallization and therefore defect landscape, a topic that will be addressed in chapter 3.

At certain temperatures, perovskite systems can undergo changes in their crystal structure, which lower the symmetry of the material and modify their electronic properties. These transitions can happen gradually and give rise to anomalous optical phenomena as chapter 4 will illustrate.

Another crucial contribution to the complexity of their electro-optical properties is of intrinsic nature. Organic-inorganic perovskites are self-assembled crystals, formed by ionic bonds

between the inorganic moieties and hydrogen bonds with the organic constituents. The organic part exhibits high rotational mobility [24], yielding a fluctuating structure in which disorder due to lattice deformations induced by reorientations of the organic molecule influences the electro-optical properties and some consequences of this phenomena will be discussed in chapter 5.

The objective of this introductory chapter is to summarize the basic photophysical principles of light-matter interaction in semiconductors and to provide a quick reference for the concepts discussed in the following. First, the crystallographic and electronic properties of hybrid perovskites will be introduced. Subsequently, we recall the absorption characteristics of direct bandgap semiconductors and the contribution of excitons. In this framework we briefly outline the thermodynamic population balance between bound excitons and uncorrelated electron-hole pairs based on the Saha equation. Being intrinsically connected to the absorption, we proceed with the luminescent properties and present a common framework to describe the recombination mechanisms in hybrid perovskites based on a Shockley-Read Hall formalism. We close the chapter with a short description of electron-phonon coupling and the correlated signatures in the optical spectra of semiconductors.

1.1 Crystal structure

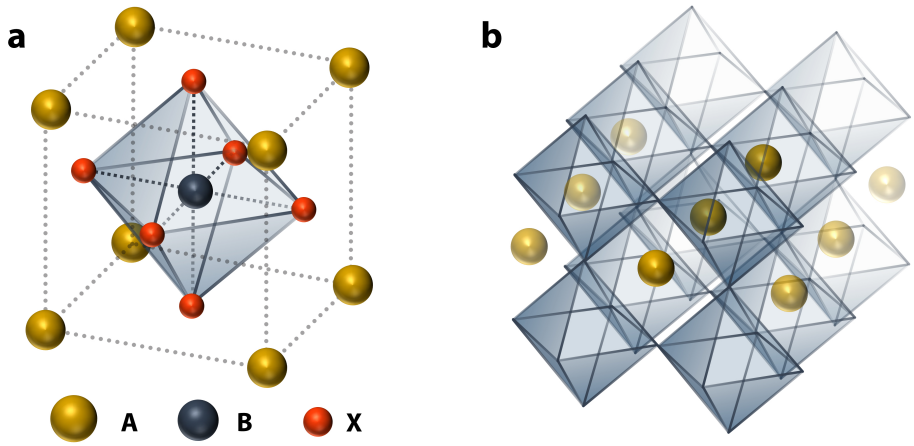

Figure 1.1
(a) Cubic unit cell of an archetypical 3D perovskite structure illustrating the octahedral arrangement of the BX_6 units. **(b)** Three dimensional perovskite lattice arrangement.

1.1.1 3D perovskites

The term perovskite originally denominates the mineral compound calcium titanium oxide $CaTiO_3$, which was first described by the German mineralogist Gustav Rose in 1839 [25] and named after the Russian mineralogist Lev Aleksevich Perovski (1792-1856). After progress in research, it became the eponym of a whole class of materials exhibiting similar crystal structure [26].

Perovskites and perovskite-type compounds have been intensively studied and exhibit a variety of phenomena, ranging from piezoelectricity [27], giant magnetoresistance [28] to superconductivity [29, 30]. The perovskite crystalline structure is prevalent in oxides, but can be found as well in other ternary compounds such as halides, with the nowadays most prominent representative, the hybrid lead halide perovskites that constitute our principal field of interest of the research presented in this thesis.
The generic stoichiometry for perovskite compounds is ABX_3 whereupon the atoms arrange ideally in a cubic ($a = b = c$) lattice of symmetry $Pm\bar{3}m$ with a 12-fold coordination of the A cation and a 6-fold coordination of the B cation (Fig. 1.1 (a)). The crystal structure consists of a network of corner sharing BX_6 octahedra, hosting the A cation at the corners of the face centered cubic halide arrangement (Fig. 1.1 (b)). The term perovskite encompasses also structures resulting from small deviations and distortions on the bonding angles within the octahedra keeping the main topology unaltered. This encloses tetragonal ($a = b \neq c$) or or-

thorhombic ($a \neq b \neq c$) configurations, often encountered since these materials have a natural predisposition towards undergoing structural phase transitions at various temperature points. Tilting of the BX_6 octahedra directly influences the pseudocubic lattice parameters and therefore the symmetry space groups [31]. Whereas the octahedral tilting corresponds to coordinated displacements, some compounds exhibit independent atomic displacements, distorting the octahedra or the positions of the other ions. These distortions further lower the symmetry and can break the inversion symmetry of the system, giving rise to new electro-optic and magnetic properties. These topics will be discussed in more detail in the last chapter.
Whether a certain chemical compound crystallizes in a perovskite structure depends on the effective radii R of the involved ions. In 1926 Goldschmidt [32] introduced the tolerance factor

$$t = \frac{R_A + R_X}{\sqrt{2}(R_B + R_X)} \tag{1.1}$$

treating all involved ions as rigid spheres and considering closed packing. The concept was extended by an octahedral factor in 2008 by Li *et al.* [33]

$$\mu = \frac{R_B}{R_X}. \tag{1.2}$$

Empirically, it was found that the tolerance factor for a stable halide perovskite structure falls within the range $\approx [0.813 - 1.107]$ together with an octahedral factor in between $\approx [0.441 - 0.895]$ [33]. As a rough estimate, we expect a symmetry reduction when the tolerance factor is smaller than 1 and a more stable structure for 1 or slightly above.
The material studied in this thesis are the halide perovskites, where the anion belongs to the VIIA group of the periodic table. Therefore, to obtain the charge-neutral ABX_3 stoichiometry, the halogen anion needs to be complemented by a monovalent and divalent A and B species, that can be an alkali metal like for example Cs^+ in fully inorganic lead halide perovskites and a divalent molecule, typically given by Pb_2^+, Ge_2^+ or Sn_2^+[1]. Hybrid perovskites are also denominated R-ammonium metallo-organic perovskites, described by the general formula RMX_3. In hybrid lead halide perovskites, the R site is occupied by a small organic molecule of single positive charge. The most common organic compounds are methylammonium (MA), $CH_3NH_3^+$ and formamidinium (FA) $H_2NCHNH_2^+$.

1.1.2 Hybrid Ruddlesden-Popper phase

Larger organic molecules require different arrangements for a stable configuration. The crystal in this case consists of inorganic layers, formed by the metal halide octahedra and separated by the organic molecules. The basic structures usually contain aliphatic or aromatic mono- ($R\text{-}NH_3)_2X_4$ and diammonium cations ($NH_3\text{-}R\text{-}NH_3)MX_4$ and strictly speaking do not represent

[1] Further possibilities include Cu_2^+, Ni_2^+, Co_2^+, Fe_2^+, Mn_2^+, Pd_2^+, Cd_2^+ and the rare earth ions such as Ca_2^+, Eu_2^+, Yb_2^+.

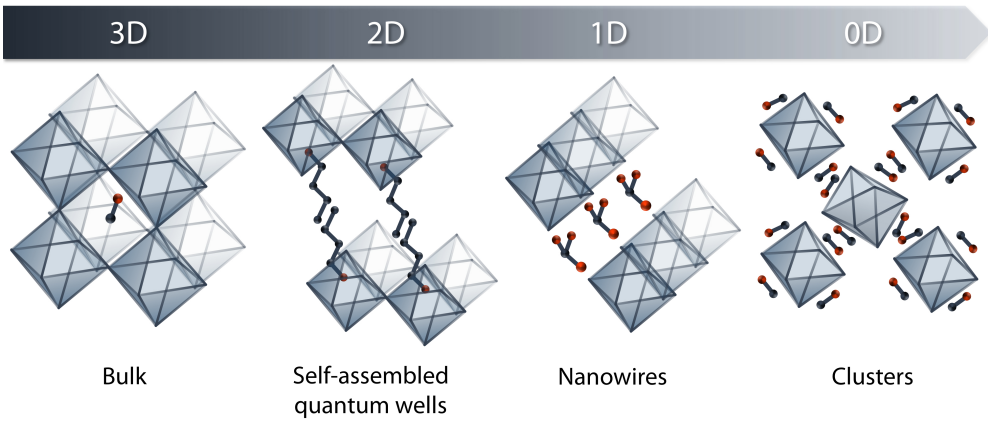

Figure 1.2
Illustration of the different crystal structures from a prototypical **3D** perovskite $CH_3NH_3PbI_3$ over **2D** $(CH_3NH_3)_2PbI_4$, **1D** $[NH_2C(I)=NH_2]_3PbI_5$ to **0D** $(CH_3NH_3)_4PbI_6{\cdot}2H_2O$.

perovskites in the classical sense. They are commonly referred to as layered perovskite-type motifs or two dimensional perovskites since the inorganic layers derive from the three dimensional AMX_3 crystal structure by taking a 'cut' along one of the main crystal directions [34]. Compounds with monoammonium cations self-assemble through the formation of organic bilayers between the inorganic sheets, either by $\pi - \pi$ stacking (when the organic unit contains aromatic groups) or Van der Waals interaction (when the molecular backbone consists of alkyl chains).

Although the size restrictions of the organic unit are relaxed in comparison to prerequisites for the 3-D compound there exist constraints to the dimension of the molecule. Being too wide renders it impossible to fit into the area provided by the inorganic framework, whereas being smaller, allows the organic unit for tilting to adapt to the provided space [35]. Nevertheless, the distance between the inorganic sheets can be varied by incorporating longer organic molecules.

The ammonium group represents the functional group interacting with the inorganic cage. Its hydrogen bonding scheme (bridging or terminal halide configuration [36]) together with the structural restrictions given by the organic tail determine the conformation of the organic interlayer with respect to the inorganic substructure. Thus proper choice of the organic molecule regulates along which crystalline direction of the 3-D parent the octahedral framework will be oriented [35]. Synthesizing the compound with a fraction of one of the smaller cations, generally used in the 3-D compounds (given that the two organic compounds have comparable solubility [36]), enables control over the dimensionality of the system by forming inorganic multilayers separated by longer organic moieties. The obtained number of perovskite sheets can be controlled by adjusting the relative ratio between the two organic cations, resulting in the general stoichiometry $R_2(A)_{n-1}M_nX_{3n+1}$ (n indicates the number of inorganic layers in between the separating long organic ligands). For the sake of completeness, we point out that

cuts along the <110> and <111> crystalline direction of the 3-D compound can result in even lower dimensional systems, namely chain like one dimensional (1D) and zero-dimensional systems (0D) consisting of isolated octahedral clusters [36, 37]. The lower dimensional hybrid perovskites (2D-0D) constitute quantum confined systems, whose particular properties will be part of the following sections.

1.2 Electronic structure

The energetic conformation of semiconductors can be canonically described through an electronic band structure. In the framework of quantum theory, considering an ideal three dimensional periodic arrangement of the atoms forming the system and neglecting or simplifying many-body interactions, the formation of conduction and valence bands can be depicted by two intuitive approximations, the free electron and tight-binding approach respectively. In the latter, the wavefunctions of the outlying valence electrons of the individual atoms are considered to overlap slightly, resulting in inter-atomic bonds, in which these electrons are shared between the nuclei. By increasing the number of atoms in the network the splitting energy levels finally merge into electronic bands. The free-electron approach solves the one-particle Schrödinger equation by introducing an effective periodic potential to account for the partially screened interaction between one delocalized conduction electron, ions and all other electrons. Both approaches have in common that the solutions for the electronic energies are based on the translation symmetry of the system and given by a dispersion relation $E(\vec{k})$ that depends on the electron wave vector rather than on the original atomic quantum numbers. The curvature of $E(\vec{k})$ can be interpreted in terms of an effective electron mass m_e^* by means of the dispersion relation $\hbar^2/m_i^* = d^2E_i(\vec{k})/d\vec{k}^2$ in the parabolic approximation.

1.2.1 3D perovskites

The band structure of hybrid lead halide perovskites has been determined theoretically via density-functional theory (DFT) [38, 40] and is shown exemplarily for the most studied compound $MAPbI_3$ (see Fig. 1.3 (a). For the sake of simplicity only the cubic phase is shown). The valence band maximum (VBM) is essentially composed of antibonding states resulting from the hybridization of lead 6s and iodine 5p orbitals, whereas empty 6p orbitals of lead form the conduction band minimum(CBM). The presence of a heavy molecule like lead, results in splitting of the conduction bands due to spin-orbit coupling (SOC) and thus lowering of the band gap[2]. The strong absorption onset at 1.6 eV corresponds to the optically allowed transition at the high symmetry R point. The connection between R and M point in the reciprocal space gives rise to the observed absorption continuum in the visible with contributions from allowed transitions in higher lying bands at the R point [40]. Since the electronic structure is dominated

[2]It is noteworthy that hybrid perovskites exhibit an inverse behaviour with respect to regular semiconductors, where SOC manifests in conduction band splitting instead

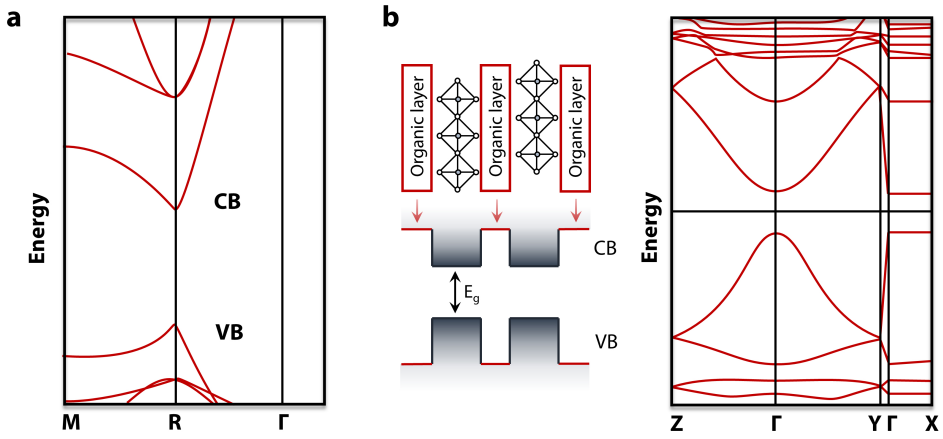

Figure 1.3
(a) Electronic band structure for cubic $MAPbI_3$ with spin-orbit coupling (adapted from [38]). **(b)** Schematic of layered organic-inorganic perovskite structure after Mitzi *et al.* [34] and calculated electronic band structure of 4F-$(PEA)_2PbI_4$, including spin-orbit coupling (adapted from [39]).

by the lead-halide network, halide substitution has the most distinct impact on the band-gap as has been shown theoretically and experimentally ([41–43]). Increasing the atomic size of the halide (Cl→ Br→ I) will lead to a decrease in bandgap energy and allows further fine-tuning by synthesizing mixed halide perovskites[3]. The semiconductor bandgap is a temperature dependent property, depending on the thermal expansion of the crystal lattice and the influence of lattice vibrations (phonons). The temperature dependence can be described by an empirical Varshni law [47]

$$E_g(T) = E_0 - \alpha \frac{T^2}{T + \beta} \tag{1.3}$$

with E_0 representing the bandgap value at zero temperature and α, β constituting intrinsic material parameters. In most semiconductors (e.g. GaAs), lattice dilation leads to a red shift in band-edge energy with increasing temperature.Pb-based compounds instead, show the opposite behaviour [48].
At first glance, the role of the organic cation within the electronic properties of the material seems to be negligible. It does not contribute to the main bonding orbitals, therefore it does not concur in optical absorption close to the band edge and seems to constitute merely a structural role. Nevertheless, the hydrogen bonding between the metal-halide network and its amine group as well as strong orientational disorder due to its rotational mobility [24, 49] can induce

[3] methyl-ammonium based compounds undergo halide segregation upon light illumination due to the defectivity of the material [44]. Current approaches to overcome this problem employ mixtures of the R-cation to restrict the crystal structures for the pure halides [45] or adding stabilizing organic cations to hamper ion migration in the material [46].

deformations of the lead-halide octahedra and therefore influence the electronic band structure. Consequently, when increasing the molecular size of the A cation ($Cs^+ \rightarrow MA^+ \rightarrow FA^+$) the bandgap slightly decreases from 1.7 eV to 1.5 eV due to a change in the Pb-X bonding angle [50–52]. It had been suggested, that formamidinium favours hydrogen bonding to the inorganic cage and takes the role of an ordering element in the final crystal structure causing less octahedral tilt with respect to methyl-ammonium [52]. Even without changing the chemical composition of the material, the electronic structure can be affected by influencing the orientation of the organic cation, e.g. decreasing grain sizes in a thin film leads to a blue shift of the absorption edge [53, 54].

1.2.2 Hybrid Ruddlesden-Popper phase

Based on the observation that these materials self-assemble in form of alternating inorganic and organic layers, Mitzi and coworkers proposed a quantum well concept [34] to describe the energetic structure of two dimensional hybrid perovskites (see Fig. 1.3 (b)). Accordingly, due to the high HOMO-LUMO (Highest Occupied Molecular Orbital and Lowest Unoccupied Molecular Orbital) energy gap in the organic compounds, the inorganic octahedra form ”wells” in between the organic ”barriers” and the system can be considered as self-organized type I multiple quantum well structure. In this context, the well width is determined by the metal halide bond length, the depth is given by the metal halide band gap and the barrier width depends on the length of the organic cation. Despite being an ostensive picture Even *et al.* showed [55], that the standard model for type I quantum wells with finite barriers (basing on effective masses and envelope functions) cannot reproduce experimental trends and predicts superlattice effects (e.g. miniband formation) which are not observed experimentally. Coulomb interactions due to the dielectric contrast between the organic and inorganic layers have a strong influence on the electronic structure and therefore on confinement effects [6, 56–58]. Even *et al.* demonstrated [55], that two-dimensional HOIPs can be described as composite material with merely weak interactions between the inorganic layers. Representatively, Figure 1.3 (b) shows the calculated band structure of the compound 4F-$(PEA)_2PbI_4$ [39].The material exhibits a direct band gap and large conduction band splitting due to SOC, similar to the three dimensional counterpart. The valence band minimum is composed of the antibonding hybridization of lead 6s and iodide 5p orbitals. The $\Gamma - X$ direction corresponds to the stacking axis in reciprocal space and does not show any dispersion, resulting from the dielectric mismatch between the inorganic and organic layer, strongly indicating the absence of super-lattice effects [39]. A direct consequence of zero dispersion is the lower dimensional density of states close to the band gap which shows the typical step function behaviour of two dimensional semiconductors.

1.3 Optical properties

One of the compelling points of hybrid perovskites contributing to their extensive investigation for photovoltaic applications, bases on their strong optical absorption. Excellent light-harvesting properties allow to employ sufficiently thin active layers in devices with good charge-collection efficiencies. Light absorption by the creation of electron hole pairs and photon emission by recombination of the latter are correlated via the principle of detailed balance [59].[4] In theory, a perfect solar cell would also constitute a perfect LED. In reality, neither device exists due to intrinsic nonradiative loss channels in semiconducting materials, either induced by trapping within intra-gap defect states or multi-particle Auger recombination. In the following we present an overview of the semi-classical theory of light-matter interactions in semiconductors, encompassing the main concepts to understand the absorption and emission characteristics with the related limitations in these materials.

1.3.1 Optical absorption

In a semiconductor, a photon with sufficiently high energy ($\hbar\omega > E_g$) excites an electron into the conduction band leaving its initial state in the valence band unoccupied, the hole. The photon wavevector is small in comparison with the typical electron wavevector and in the dipole approximation [60], only vertical transitions are optically allowed $\delta k = 0$. Consequently, electron and hole have opposite momentum and if initially unbound, move independently through the crystal with kinetic energy $\hbar k^2/(2m_c^*)$ (with $c = e,\ h$ for electron and hole respectively). The redistribution of photon energy among them depends on their respective effective masses. The effective masses of electrons and holes in hybrid perovskites are almost identical $m_e^* \approx m_e^*$ and the energy of an absorbed photon is shared equally. Electrons are fermions and their occupation probability follows Fermi-Dirac statistics

$$f(E) = \frac{1}{1 + e^{(E-E_F)/k_B T}} \tag{1.4}$$

with the Boltzmann constant k_B and the Fermi energy E_F. In an intrinsic semiconductor, the Fermi energy will be situated in the middle of the bandgap, resulting in a completely filled valence and empty conduction band at zero temperature. After photo-excitation, several relaxation stages occur before the system returns to thermal equilibrium. Following the classification of J. Shah [61], these processes can be divided into four temporally overlapping stages, starting from coherent relaxation over non-thermal processes, hot-carrier and finally isothermal relaxation.

In the coherent regime, the photo-excitation in a semiconductor has a well-defined phase relation with the incoming radiation field and many fundamental quantum-mechanical processes influencing electron and multi-particle interactions arise in this time span. Unlike atomic systems, scattering processes in semiconductors are extremely fast and destroy the generated co-

[4] Under general presumptions this is equivalent to the Kubo-Martin-Schwinger relation.

herence within picoseconds. Consequently, the study of coherent phenomena requires the use of ultrafast spectroscopic techniques.
A non-resonant optical excitation leads to an initially sharp energy distribution function of the free carriers in the conduction band, peaking at the photon energy, which cannot be characterized by a temperature. Various scattering processes (e.g. electron-electron elastic scattering and inelastic processes) establish a thermal redistribution of energy within the carrier population on a timescale of hundreds of femtoseconds to tens of picoseconds, introducing the hot carrier regime. Now, an effective temperature T_c can be assigned to the carrier population, exceeding the temperature of the crystal lattice T_L. The photocarrier ensemble subsequently relaxes by electron-phonon interactions within ps to hundreds of ps until all photoexcited species are in thermal equilibrium with the lattice. [5] In the isothermal regime, radiative and non-radiative recombination processes between electrons and holes bring the excited state carrier population back to the ground state and therefore towards the thermodynamic equilibrium. Comprehensive review articles on the effects of hot carriers can be found in the references [64–66]

Excitons

In direct semiconductors, the attractive Coulomb interaction between electron and hole leads to a new charge-neutral bound state, the exciton. Its binding energy is a measure for the degree of stabilization of the quasi-particle. Electron and hole of an exciton orbit each other, similar to electron and proton in a hydrogen atom. Hence, by considering only the Coulomb interaction, the two-particle problem can be solved in analogy to the hydrogen atom by introducing simply one important modification. Screening due to other charged particles in the semiconductor is introduced by an effective dielectric function, assuming that the electron-hole pair is sufficiently large to treat the surrounding environment as homogeneous medium. This results in the well known Wannier-Mott exciton model (found in [60, 67, 68]), whose derivation will be outlined in the following. The Hamiltonian for the bound electron-hole system can be written as

$$\hat{\mathcal{H}}_X = -\frac{\hbar^2 \nabla_e^2}{2m_e^*} - \frac{\hbar^2 \nabla_h^2}{2m_h^*} - \frac{e^2}{4\pi\varepsilon_0\varepsilon_r \mid \vec{r}_e - \vec{r}_h \mid} \tag{1.5}$$

where ε_0 is the permittivity of free space, ε_r takes into account the dielectric environment inside the semiconductor and $\vec{r}_e$, $\vec{r}_h$ are the spatial coordinates of electron and hole. The close

[5] Carrier cooling in semiconductors happens on two timescales, with an initial rapid decay due to interactions with longitudinal optical (LO) phonons and a slower decay due to acoustic phonon scattering, arising for example from the Klemens channel, when a LO phonon relaxes into counter-propagating acoustic phonons. However, a "hot-phonon bottleneck" can reduce the carrier thermalization rate and had been reported for $MAPbI_3$ [62, 63]. This effect can occur for example at high excitation densities, inducing a non-equilibrium phonon population which increases the probability of phonon re-absorption, in quantum confined structures and due to an inefficient Klemens channel in case of large energy separation between LO and acoustic phonon branches. Long living hot carrier populations constitute an interesting topic for the photovoltaic community, since efficient extraction would allow to increase the open circuit voltages and therefore the PEC.

resemblance to the Hamiltonian for the hydrogen atom allows to solve the corresponding Schrödinger equation in the same way, by substituting the characteristic length and energy parameters by rescaled quantities. Introducing the center-of-mass coordinate $\vec{R} = (m_e^*\vec{r}_e + m_h^*\vec{r}_h)/(m_e^* + m_h^*)$ and relative coordinate $\vec{r} = \vec{r}_e - \vec{r}_h$ it is possible to decouple the motion of the whole exciton from the relative motion of its constituents and to use a factorized wave function as ansatz in the stationary Schrödinger equation $\hat{\mathcal{H}}_X\psi_X = E_X\psi_X$ leading to two equations solely depending on the new coordinates:

$$\left(-\frac{\hbar^2}{2m_X}\nabla_{\vec{R}}^2\varphi(\vec{R})\right) = E_{\vec{R}}\varphi(\vec{R}) \tag{1.6}$$

$$\left(-\frac{\hbar^2}{2\mu_X}\nabla_{\vec{r}}^2 - \frac{e^2}{4\pi\varepsilon_0\varepsilon_r\,|\,\vec{r}\,|}\right)\phi(\vec{r}) = E_{\vec{r}}\phi(\vec{r}). \tag{1.7}$$

$m_X = m_e^* + m_h^*$ refers to the effective exciton mass, and equation 1.6 describes the excitonic motion through the crystal with wave vector $\vec{K}_X$. The quantity $\mu_X = (1/m_e^* + 1/m_h^*)^{-1}$ represents the reduced exciton mass and equation 1.7 designates the rotating motion of electron and hole and is called Wannier equation. The procedure (transformation to spherical/polar coordinates for 3D/2D systems respectively and factorization of the ansatz) to solve equation 1.7 can be found in many text-books for quantum mechanics (e. g. [60, 69, 70]) and we report merely the final exciton energy which results from bound solutions $E < E_g$ considering both equations

$$E_X = E_g - \frac{R_y^*}{n^2} + \frac{\hbar K_X^2}{2m_X}, \quad n = 1, 2, 3\ldots \quad \text{for 3D} \tag{1.8}$$

$$E_X = E_g - \frac{R_y^*}{(n-\frac{1}{2})^2} + \frac{\hbar K_{\parallel X}^2}{2m_X}, \quad n = 1, 2, 3\ldots \quad \text{for 2D} \tag{1.9}$$

where E_g is the semiconductor bandgap, the second term describes the energy eigenvalues of the exciton arising from the hydrogen problem with $R_y^* = \mu_X/(m_0\varepsilon_r^2)R_y$ being the exciton Rydberg energy, rescaled with respect to the hydrogen Rydberg constant $R_y = 13.61$ eV and the last term representing the kinetic energy of the exciton. The unbound solutions of equation 1.7 correspond to the free carrier continuum. Due to the small reduced mass and usually large dielectric constant, the exciton binding energy (the energy difference between bandgap and first excitonic transition)is much weaker than the energy of the hydrogen atom and the exciton radius is comparably large. The formation of excitons influences the linear absorption spectrum of semiconductors with the occurrence of strong transitions below the bandgap.

Elliott formula

The absorption close to the band edge in direct bandgap semiconductors with exciton binding energies distinctly smaller than the bandgap can be modeled using Elliott's theory of Wannier excitons [71], a formalism that had already been successfully employed to describe the ab-

sorption of inorganic semiconductors like GaAs [72]. To derive the expression for the optical absorption in the presence of excitons the full Hamiltonian

$$\hat{\mathcal{H}} = \hat{\mathcal{H}}_0 + \hat{\mathcal{H}}_C + \hat{\mathcal{H}}_I \tag{1.10}$$

encompassing coulomb interaction $\hat{\mathcal{H}}_C$ and interaction with the light field $\hat{\mathcal{H}}_I$ has to be taken into account and the time dependent Schrödinger equation has to be solved

$$i\hbar\frac{\partial}{\partial t}\psi(\vec{r},t) = \hat{\mathcal{H}}\psi(\vec{r},t) \tag{1.11}$$

Haug *et al.* [60] show that the problem leads to the inhomogeneous equation

$$\left[i\hbar\frac{\partial}{\partial t} + \frac{\hbar^2\nabla_{\vec{r}}^2}{2\mu_X} - V(\vec{r})\right]P(\vec{r},t) = -d_{cv}E(t)\delta\vec{r} \tag{1.12}$$

with the Wannier equation 1.7 as homogeneous part. d_{cv} represents the electron-hole interband dipole matrix element between valence and conduction band and $P(\vec{r},t)$ the polarization of the material. By knowing the energy values and exciton and continuum wavefunctions from the Wannier equation, the problem can be solved by expanding the polarization into the Wannier wavefunctions $P(\vec{r},t) = \sum_\nu b_\nu\psi(\vec{r})$. This leads to the Elliott formula [60, 71] for the absorption in a semiconductor, which results in the three dimensional case to

$$\alpha_{3D}(\hbar\omega) \propto \hbar\omega(d_{cv})^2\left[\sum_{n=1}^{\infty}\frac{4\pi R_y^{*3/2}}{n^3}\delta(\hbar\omega - E_g + \frac{R_y^*}{n^2}) + \Theta(\hbar\omega - E_g)\frac{2\pi\sqrt{R_y^*}}{1 - e^{-2\pi\sqrt{\frac{R_y^*}{\hbar\omega - E_g}}}}\right] \tag{1.13}$$

and considering an ideal two dimensional ultrathin quantum well yields

$$\alpha_{2D}(\omega) \propto \hbar\omega\frac{(d_{cv})^2}{L_c}\left[\sum_{n=0}^{\infty}\frac{4R_y^*}{(n-\frac{1}{2})^3}\delta(\hbar\omega - E_g + \frac{R_y^*}{(n-\frac{1}{2})^2}) + \Theta(\hbar\omega - E_g)\frac{2}{1 + e^{-2\pi\sqrt{\frac{R_y^*}{\hbar\omega - E_g}}}}\right]. \tag{1.14}$$

Here, L_c determines the well width. The absorption spectrum in the presence of excitons is composed of a series of sharp transitions, represented by the first term in equations 1.13 and 1.14 with rapidly decreasing oscillator strength $\propto n^{-3}$ and $\propto (n-\frac{1}{2})^{-3}$ respectively. The continuum contribution from the absorption of the ionized states is given by the second term. A comparison with the expected continuum absorption of free non-interacting carriers ($\alpha_{free}(\hbar\omega) \propto \sqrt{\hbar\omega - E_g}$ in 3D and $\propto const.$ in 2D) shows, that Coulomb interaction also modifies the appearance of this absorption band. We can write

$$\alpha_{cont} \propto \alpha_{free}C_{3D,2D}(\omega) \tag{1.15}$$

with

$$C_{3D}(\omega) = \frac{2\pi}{1 - e^{-2\pi\sqrt{\frac{R_y^*}{\hbar\omega - E_g}}}} \sqrt{\frac{R_y^*}{\hbar\omega - E_g}} \tag{1.16}$$

and

$$C_{2D}(\omega) = \frac{2}{1 + e^{-2\pi\sqrt{\frac{R_y^*}{\hbar\omega - E_g}}}} \tag{1.17}$$

respectively, the Sommerfeld or Coulomb correction factors [60]. For $\hbar\omega \to E_g$ we see that the Coulomb interaction approaches a constant value in the 3D case and 2 in the 2D case, therefore the free carrier absorption is strongly enhanced close to the band edge [60]. To apply Elliott's formula to real semiconductors we convolve the above expression for the absorption with a hyperbolic secant function, describing an inhomogeneously broadened transition. Additionally, we introduce a correction factor a to account for a slight non-parabolicity of the electronic bands $\varepsilon = \frac{\hbar^2 k^2}{2m^*} - ak^4$. With the substitution $\varepsilon_0 = \frac{\hbar^2 k^2}{2m^*}$ we get

$$d\varepsilon_0 = \frac{1}{1 - a\frac{8m^{*2}}{\hbar^4}\varepsilon_0} d\varepsilon \tag{1.18}$$

and finally

$$\begin{aligned} \alpha(\hbar\omega) &= \alpha_{3D} * \sec\left(\frac{\hbar\omega}{\Gamma}\right) \\ &\propto \hbar\omega (d_{cv})^2 \Big[\sum_{n=0}^{\infty} \frac{4\pi R_y^{*3/2}}{n^3} \sec\left(\frac{\hbar\omega - Eg + \frac{R_y^*}{n^2}}{\Gamma}\right) \\ &\quad + \int_{E_g}^{\infty} \sec\left(\frac{\hbar\omega - \varepsilon}{\Gamma}\right) \frac{2\pi\sqrt{R_y^*}}{1 - e^{-2\pi\sqrt{\frac{R_y^*}{\hbar\omega - E_g}}}} \frac{1}{\left[1 - \frac{a8m^*}{\hbar^4}\left(\varepsilon - E_g\right)\right]} d\varepsilon \Big] \end{aligned} \tag{1.19}$$

for the 3D case and

$$\begin{aligned} \alpha(\hbar\omega) &= \alpha_{2D} * \sec\left(\frac{\hbar\omega}{\Gamma}\right) \\ &\propto \hbar\omega \frac{(d_{cv})^2}{L_c} \Big[\sum_{n=1}^{\infty} \frac{4R_y^*}{\left(n - \frac{1}{2}\right)^3} \sec\left(\frac{\hbar\omega - Eg + \frac{R_y^*}{\left(n-\frac{1}{2}\right)^2}}{\Gamma}\right) \\ &\quad + \int_{E_g}^{\infty} \sec\left(\frac{\hbar\omega - \varepsilon}{\Gamma}\right) \frac{2}{1 + e^{-2\pi\sqrt{\frac{R_y^*}{\hbar\omega - E_g}}}} \frac{1}{\left[1 - \frac{a8m^*}{\hbar^4}\left(\varepsilon - E_g\right)\right]} d\varepsilon \Big] \end{aligned} \tag{1.20}$$

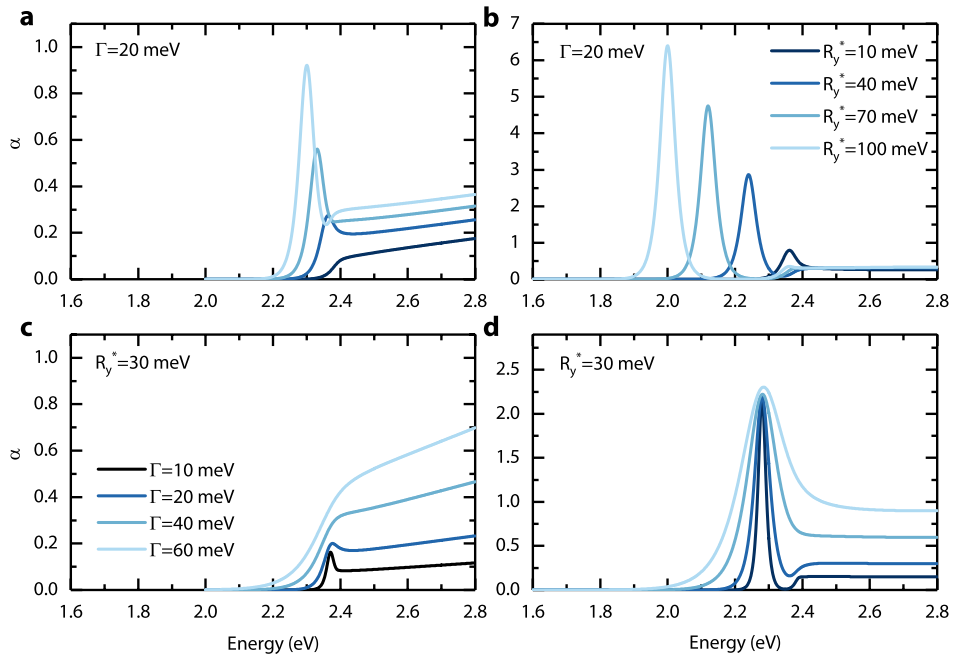

Figure 1.4
Absorption spectrum of a semiconductor after Elliott's model for a three dimensional system **(a)**,**(c)** and an ultrathin quantum well **(b)**,**(d)**. The top panels illustrate the influence of dimensionality on the exciton binding energy, the bottom panels show the effect of the broadening parameters for the two systems.

for the 2D case. The two resulting spectra are displayed in Figure 1.4. Depending on the broadening parameter, only the first bound states can be resolved, higher lying states merge smoothly into the ionization continuum. In comparison to the 3D case, the binding energy in two dimensional systems experiences a four-fold increase (Fig. 1.4 (b)).

A broad range of exciton binding energies has been reported for the compound $MAPbI_3$ starting from 2 meV to 50 meV [73–76] and slightly higher values for its bromide counterpart. The divergence can be partly assigned to the different experimental techniques used to determine the binding energy and partly to a substantial variance in the dielectric properties [54]. The latter can be attributed to differing microstructures as a result of the applied processing routine. Another source of error are indirect measurements that cannot yield a direct value of the binding energy or presume exact knowledge of the dielectric function to calculate the corresponding value. The dielectric function of a material is composed of the different frequency dependent response regimes of the material, involving lattice displacements (10^0 – 10^{10} s^{-1}), molecular rotations (10^{10} – 10^{12} s^{-1}) and electronic transitions ($\sim 10^{15}$ s^{-1}) [77]. Hybrid perovskites are ionic crystals, thus the contribution of various low and high energy phonon modes gives rise to a strong frequency dependent dielectric response of the material and its perme-

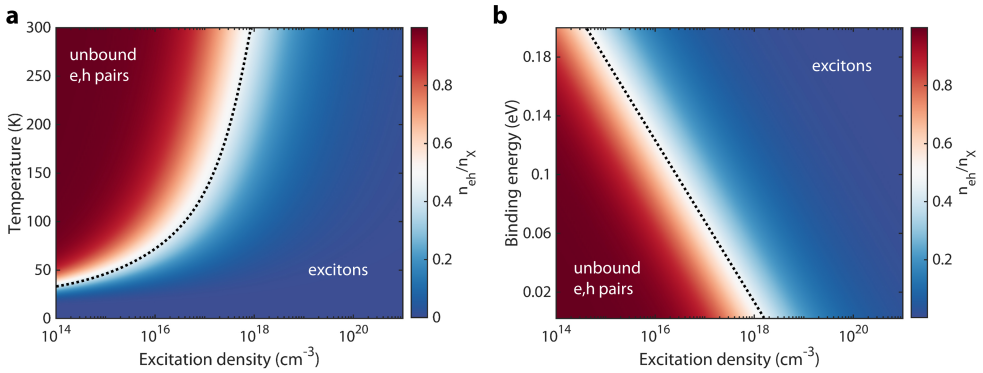

Figure 1.5
Saha-Langmuir equation: fraction of free carriers over excitons **(a)** as a function of temperature and excitation density, the binding energy was set to 20 meV and **(b)** as a function of exciton binding energy at room temperature (290 K). For the calculations $\mu_X = 0.15m_0$ was used. The transitions between the two regimes are marked by the dotted lines as guide to the eyes.

ttivity varies between ~ 6 at optical frequencies and ~ 70 approaching static conditions [73]. For calculations of the exciton binding energy it is crucial to know, which contributions have to be taken into account. If we presume a strongly delocalized large exciton with small binding energy, ionic and molecular motions can temporally coincide with the relative motion of the bound-electron hole pair, resulting in a strong screening of the Coulomb interaction. In case of a small exciton with strong binding energy, the lattice contributions will not influence the high frequency motion of the exciton and the local dielectric value at optical frequencies has to be chosen. Taking simply the static dielectric constant, as usually done for covalent solids with little dispersion can result in a strong underestimation of the actual binding energy. Excellent reviews addressing, amongst other topics, the diversity in literature about that topic can be found in [49, 77, 78].

1.3.2 Saha-Langmuir equation

The exciton binding energy is not the only parameter contributing to a stable exciton population, we also have to consider the total density of particles in the system. The previously exerted analogue between the Wannier-exciton and the hydrogen atom can be further exploited to derive an equation, that describes the thermodynamic balance between exciton dissociation and therefore creation of uncorrelated electron-hole pairs and recombination and formation of bound pairs. The dissociation of excitons into free carriers

$$X \overset{\Delta}{\leftrightarrow} p^+ + e^- \quad \Delta = Ry^* = E_b \tag{1.21}$$

leads to a coexistence of bound and unbound electron-hole pairs. The Saha equation [79, 80] can describe the population balance between excitons and unbound electron-hole pairs as a

function of temperature, binding energy and particle density in thermodynamic equilibrium [6]. To derive the corresponding equation, we start from the canonical partition functions for an ensemble consisting of N_e electrons, N_h holes and N_X excitons respectively and treat the constituents as undistinguishable. The present ensemble can be composed entirely of free e-h pairs, partially ionized or formed by bound states only and the corresponding partition function results to [81]

$$Z_{TOT} = \sum_{N_e,N_h,N_X} \frac{Z_e^{N_e}}{N_e!} \frac{Z_h^{N_h}}{N_h!} \frac{Z_X^{N_X}}{N_X!} \tag{1.22}$$

Every term in equation 1.22 normalized by Z_{tot} represents the probability to find the system in the corresponding configuration and the sum is taken over all possible configurations. Note, that the total number of particles has to be conserved ($N_e + N_h + N_X = const.$).
The energies of the single particles are given by $p^2/2m^*_{e,h}$ for electron and holes and $p^2/2m_X - E_b$ for excitons respectively. The partition functions for the single constituents can be obtained by integration over phase space and volume of the system [7]

$$Z_X = \frac{1}{(2\pi\hbar)^3} \int_V d^3r \int d^3p e^{-\frac{p^2}{2m_X k_B T}} e^{\frac{E_b}{k_B T}} = V\left(\frac{m_X k_B T}{2\pi\hbar^2}\right)^{3/2} e^{\frac{E_b}{k_B T}} \tag{1.23}$$

$$Z_{e,h} = \frac{1}{(2\pi\hbar)^3} \int_V d^3r \int d^3p e^{-\frac{p^2}{2m^*_{e,h} k_B T}} = V\left(\frac{m^*_{e,h} k_B T}{2\pi\hbar^2}\right)^{3/2} \tag{1.24}$$

To find the configuration with the largest probability we follow the considerations of R. Gilmore [82] assuming that the wanted maximum can be described by a continuous function of the configuration integers. For sufficiently large particle numbers, we can safely set two consecutive configurations as approximately equal.

$$\frac{Z_e^{N_e}}{N_e!} \frac{Z_h^{N_h}}{N_h!} \frac{Z_X^{N_X}}{N_X!} \approx \frac{Z_e^{N_e}}{(N_e+1)!} \frac{Z_h^{N_h}}{(N_h+1)!} \frac{Z_X^{N_X}}{(N_X-1)!} \tag{1.25}$$

Which can be reformulated to

$$\begin{aligned} \frac{Z_X}{N_X} &= \frac{Z_e}{N_e+1} \frac{Z_h}{N_h+1} \\ \frac{Z_e Z_h}{Z_X} &\approx \frac{N_e N_h}{N_X} \end{aligned} \tag{1.26}$$

By inserting the derived partition functions (eq. 1.23), defining the particle density as $n_c = N_c/V$ (for $c = e, h, X$) and considering the fraction of free electron-hole pairs over bound ones

[6] Originally, the Saha equation had been deployed to describe the population of ionized states in a system of free particles as a function of pressure and temperature and it had been used to characterize the ionization equilibrium in hydrogen

[7] For quantitative results, the degeneracy factors for the photo-excited species, e. g. due to the spin have to be known. They contribute as scaling factors in the final equation but can be disregarded for the general qualitative discussion here.

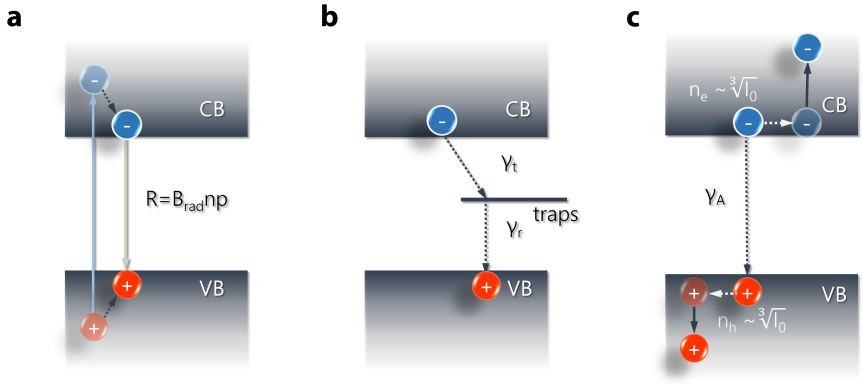

Figure 1.6
Scheme of different recombination mechanisms: **(a)** bimolecular recombination, **(b)** trap limited recombination assuming deep traps, **(c)** Auger recombination, involving 3 particles.

using the relations $n_X = (1-x)n_0$ and $n_e = n_h = xn_0$ the Saha-Langmuir equation describing the thermodynamic ionization equilibrium of excitons in semiconductors can be written as

$$\frac{x^2}{1-x} = \frac{1}{n_0}\left(\frac{\mu_X k_B T}{2\pi\hbar^2}\right)^{3/2} e^{\left(\frac{-E_b}{k_B T}\right)} \tag{1.27}$$

Figure 1.5 shows two simulations employing equation 1.27, either varying the temperature at static binding energy or vice versa. By keeping the binding energy fixed ($\sim k_B T$) and increasing the temperature, the free carrier ratio grows, due to easier ionization at elevated temperatures. Rising instead the binding energy shifts the point of predominant exciton generation towards lower excitation densities. Finally, the above example demonstrates that in thermodynamic equilibrium, considering the typical binding energies of three dimensional hybrid perovskites, excitons will play a minor role at the excitation densities for photovoltaic applications ($n_0 \sim 10^{16}$ cm^{-3}) but in some compounds they could become an important contribution at high excitation densities, necessary to achieve lasing.[8]

1.3.3 Photoluminescence

Although the exact value of the exciton binding energy is still a matter of debate, consensus had been reached that free electrons and holes form the predominant population after photo-

[8]Note, that the Saha equation does not take into account nonlinear effects due to many-body interactions. Above a certain critical carrier density, depending on the exciton Bohr radius, excitons are no longer stable and undergo a Mott transition to a correlated electron-hole plasma (EHP) [83–85] due to exciton-exciton scattering. Depending on binding energy, dielectric environment and temperature, a stable excitonic phase might never form.

excitation in 3D hybrid perovskites. Excitons, although contributing to the absorption lineshape, are not populated [74, 84, 86], which is a convenient outcome for the photovoltaic community. To reach thermodynamic equilibrium, the photo-excited carrier population decays to the ground state by virtue of several relaxation channels, which can be divided into radiative and non-radiative processes. The former encompasses a multitude of underlying physical mechanisms, depending on the nature of the emitting species (e.g. band to band recombination, exciton recombination, recombination through impurity states) and the excitation regime (e.g. luminescence of an electron-hole plasma or Bose Einstein condensate) [87]. They all have in common, that at least part of the excitation energy is converted into light. Non-radiative processes instead transform the excitation energy into other types of energy, including heat by the emission of phonons, defect generation or photochemical changes of the material. Both processes can be influenced by the defectivity of the material. Hence, the lifetime of the carrier population is given by the sum of all available decay paths. In the following, we will discuss the theoretical formalism which is widely used to explain the recombination dynamics in hybrid perovskites. In particular, we will highlight the trends of the steady-state behaviour with excitation intensity, which constitutes an indispensable tool to interpret the results of Chapter 3.
In general, population decay dynamics are often expressed through a simple rate equation [74, 86, 88, 89]:

$$\frac{dn}{dt} = -k_1 n - k_2 n^2 - k_3 n^3 \tag{1.28}$$

where, $k_{1,2,3}$ are the rate constants associated with different recombination processes. k_1 describes monomolecular processes, which can be due to excitonic, geminate recombination or carrier trapping. k_2 is connected to the intrinsic bimolecular recombination of electron and holes and consequently depending on the carrier densities n^2. k_3 represents the non-radiative Auger recombination, a many-body process, involving energy transfer to a third participant and eventually the absorption or emission of phonons to maintain momentum conservation. Consequently this process heavily depends on the excitation density. The total recombination rate results to

$$R(n) = k_1 + k_2 n + k_3 n^2 \tag{1.29}$$

and is connected to the diffusion length via

$$L_D(n) = \sqrt{\frac{\mu k_B T}{R(n) e}} \tag{1.30}$$

with μ being the carrier mobility, k_B the Boltzmann constant, T the temperature and the electronic charge e [78]. The relative importance of the three contributions will change depending on the excitation density regime.

Radiative recombination

We will first consider the simple case of purely radiative recombination of electron and hole. The rate equation describing the photoexcitation dynamics can be read as

$$\frac{dn}{dt} = G - B_{rad}n^2 \tag{1.31}$$

where G is the charge photo-generation rate, and B_{rad} the bimolecular recombination coefficient. This equation can be solved with the initial conditions $n_0 = 0$. It follows, that the PL intensity is a quadratic function of the excitation light intensity at early times ($G \propto I_{ex}$) and the time evolution of the excited state population density results to

$$n(t) = \frac{n_0}{(B_{rad}n_0t + 1)} \tag{1.32}$$

and subsequently for the PL intensity we obtain

$$I_{PL}(t) \propto B_{rad}n^2(t) = \frac{B_{rad}n_0^2}{(B_{rad}n_0t + 1)^2} \tag{1.33}$$

Under steady-state conditions, the temporal evolution can be set to zero $dn/dt = 0$ and the photoluminescence intensity results to $I_{PL} = B_{rad}n^2 = G$. The charge generation rate scales linearly with excitation density, hence, in the purely radiative regime, the integrated PL intensity shows a linear behavior as well.
If photo-excitation leads to a stable population of bound electron-hole pairs radiative recombination will be a mono-molecular process and the corresponding rate equation can be written as

$$\frac{dn_X}{dt} = G - An_X \tag{1.34}$$

where A is the monomolecular recombination coefficients and n_X the exciton density. The steady state solution leads to a population of $n_X = G/A$, and similar to pure bimolecular recombination, to a linear behaviour of the photoluminescence signal with light intensity $PL \propto n_X \propto G \propto I$.

Trap limited recombination

In real systems, radiative recombination is limited by non-radiative decay channels, either due to trapping of the photo-excited carriers within defect states, generation of defect states or non-radiative multi-particle processes like Auger recombination. Trap-limited recombination dominates the PL behaviour for excitation densities below the accessible defect density and represents the most important non-radiative loss channel for photovoltaic and light-emission (LED) applications, whereas Auger recombination constitutes the predominant loss mecha-

nism for lasing operation in the high excitation density regime. We restrict our discussion to the most widely used trap-limited recombination model for hybrid perovskites, which can be expressed within a simplified Shockley-Read Hall (SRH) [90] framework. Photo-induced trap healing and formation [86, 91–93], based on ion diffusion are also observed in this class of materials; they are collectively termed photoinstabilities (see short discussion in Chapter 3) but an in depth description is beyond the scope of this thesis.
On of the most widely used models to describe non-radiative recombination in the presence of trap states is given by a set of coupled rate equations, which describe the population dynamics of electrons, holes and occupied trap states (presuming predominantly electron traps) respectively

$$\frac{dn}{dt} = G - \gamma_t(N_t - n_t)n - B_{rad}np \tag{1.35}$$

$$\frac{dp}{dt} = G - \gamma_r p n_t - B_{rad}np \tag{1.36}$$

$$\frac{dn_t}{dt} = \gamma_t(N_t - n_t)n - \gamma_r p n_t. \tag{1.37}$$

Here, γ_t represents the trapping rate, N_t is the total trap density, n_t the density of filled traps andγ_r denotes the non-radiative recombination rate of a trapped electron with a hole. Charge neutrality leads to $n + n_t = p$. Note that this formalism assumes deep intra-gap trap states ($\gg k_B T$), rendering thermal energy deficient to detrap carriers again.
In steady-state, at low excitation densities, the photo-excitation density is smaller than the available trap density ($n \ll N_t$) and trap-mediated recombination poses the most efficient available pathway. Since electron-trapping is a monomolecular process, therefore scales linearly with excitation density, and recombination of a trapped electron with a hole on the other side constitutes a bimolecular mechanism we get $n \propto I_{ex}/(\gamma_t N_t)$ and $p \propto \sqrt{I_{ex}/\gamma_r}$. The resulting integrated PL intensity shows a superlinear intensity dependence $I_{PL} \propto B_{rad}np \propto B/(\gamma_t N_t \gamma_r^{1/2}) \cdot I_{ex}^{3/2}$. At higher carrier densities, the available trap states are mostly occupied and trapping slows down, consequently bimolecular recombination becomes dominant and the intensity dependence changes to a linear behaviour [84, 94]. For very high carrier densities, necessary for lasing applications, another term has to be added to the rate equations 1.35 to account for the non-radiative losses due to Auger recombination.

Auger recombination

At the high charge density regime, non-radiative processes due to many-body interactions become preponderant, reducing radiative recombination. Auger recombination involves at least three quasi-particles, two electrons and one hole (*eeh* processes) or two holes and one electron (*hhe* processes). Excess energy of a recombining electron will not be emitted as photon but transferred to the third particle instead, given that energy and momentum conservation is fulfilled, consequently involving phonons or if available, suitable energy bands. Subsequently, the third excited particle relaxes quickly by multiphonon emission dispensing its energy into

the lattice. The corresponding rate equations can be written as

$$\frac{dn}{dt} = G - B_{rad}np - \gamma_{An}n^2p \tag{1.38}$$

$$\frac{dp}{dt} = G - B_{rad}np - \gamma_{Ap}p^2n \tag{1.39}$$

If, for simplicity, we presume equal electron and hole densities we obtain for the Auger rate a cubic behaviour with excited carrier population.

$$R_A = \gamma_A n^3 \tag{1.40}$$

In steady-state, assuming $B_{rad}n^2 \ll \gamma_A n^3$ we obtain $n = \sqrt[3]{I/\gamma_A}$. The photoluminescence intensity constitutes a sublinear function of the excitation intensity and is given as $I_{PL} = B_{rad}n^2 = B_{rad}(I/\gamma_A)^{\frac{2}{3}}$. Generally, Auger recombination can be affected by carrier localization at impurities and by the particular vibrational and electronic structure of the semiconductor [88, 95, 96]. The radiative recombination coefficient sets an intrinsic limit to carrier diffusion lengths, therefore represents an important parameter for device optimization. For solar applications, low radiative recombination rates and low defect densities are crucial to obtain long diffusion lengths and therefore efficient carrier collection in PV devices. As a consequence a large steady-state carrier density under illumination assures a considerable open-circuit voltage [97]. This mutual dependence between recombination and diffusion length highlights the importance of precise photophysical models of the material.

1.4 Electron-phonon coupling

Coupling between fermions and bosons, has been a widely studied topic in many-particle physics. The interactions between electrons and phonons are omnipresent in solid state systems and give rise to a broad variety of intrinsic material properties, e. g. the temperature dependence of the electrical resistivity in metals and electronic bands in solids, the carrier mobility in semiconductors, superconductivity, they determine the thermalization of hot carriers and consequently become manifest in the optical properties of materials.
Owing to the ionic, "soft" crystal structure of hybrid metal-halide perovskites, one can expect that lattice vibrations and electronic properties are strongly correlated. In particular, two observations have puzzled the scientific community, invoking a debate about the influence of electron-phonon coupling in this class of materials. On the one hand, their carrier recombination rates are remarkably low [98] and comparable to the ones found for highly crystalline semiconductors [99], on the other hand they exhibit only modest charge carrier mobilities ($\mu \sim 1 - 100\text{cm}^2\text{V}^{-1}\text{s}^{-1}$) [88, 100] in comparison to conventional semiconductors like GaAs. Zhu and coworkers [99, 101] have postulated large polaron formation, referring to a quasiparticle, either an electron or hole with mass m_p that polarizes, hence locally deforms the lattice when moving through the ionic crystal. The interaction with the ionic crystal lattice slows

down its motion and becomes manifest in a higher effective mass in comparison to the free particle. This picture could explain the relatively low carrier mobilities in hybrid perovskite despite low effective masses of the free particle [75, 102] and would be consistent with the observation of temperature dependent homogeneous emission linewidths in these materials [103].
In the following, we will give a brief recap of the pertinent fundamental principles behind electron-phonon coupling and qualitatively describe its influence on the optical properties of materials.

1.4.1 Mechanisms of electron-phonon coupling

We briefly address the underlying physical mechanisms enabling electron-phonon and exciton-phonon coupling respectively. In semiconductors we can distinguish three main microscopic processes, the deformation potential due to acoustic phonons, in which distortions of the lattice modify the electronic band structure, the piezoelectric mechanism, that influences the carriers due to macroscopic fields in the material induced by mechanical deformation and the Fröhlich mechanism [67, 87]. The latter is the most relevant interaction mechanisms in ionic (polar) semiconductors like hybrid perovskites [9] and is expected to dominate electron-phonon coupling processes, therefore carrier cooling and optical transitions. Its principle is based on the Coulomb interaction between bound or unbound e-h pairs and a local electric field induced by oscillations of oppositely charged ions. To illustrate the concept, we take a cubic metal halide perovskite structure in which the metal cations (M^{2+}) and halide anions (X^{-}) are situated on alternating planes along the [111] crystal direction (see Fig. 1.7 (a)). The excitation of longitudinal optical (LO) phonons perpendicular to the planes results in a temperature dependent oscillating separation of the different ion planes, which act as capacitor plates and induce a local electric field that interacts with the charge carrier or excitons [87] [10].
The mechanism can be quantified, by introducing a dimensionless coupling constant [87]

$$\alpha = \frac{e^2}{8\pi\varepsilon_0 r_p}\left(\frac{1}{\varepsilon_\infty} - \frac{1}{\varepsilon_s}\right)\frac{1}{\hbar\omega_{LO}} \tag{1.41}$$

where ε_s and ε_∞ represent the screening at low frequencies and the electronic screening respectively. Recalling the previous discussion about the frequency dependence of the dielectric function in perovskites, the coupling increases with the degree of ionicity in the system. $r_p = \hbar/\sqrt{2m_p\hbar\omega_{LO}}$ is called polaron radius, the size of the deformed lattice region due to polarization of the charge carrier.
Electron-phonon interactions influence the dynamical processes in a material, e.g. optical dephasing and exciton dissociation due to phonon scattering, which affects the spectral width of the observed electronic transitions. The various contributions to linewidth broadening can

[9] In contrast, the Fröhlich mechanism does not play a role in elemental (covalent) semiconductors like Ge or Si
[10] transversal optical modes do not induce a comparable crystal polarization

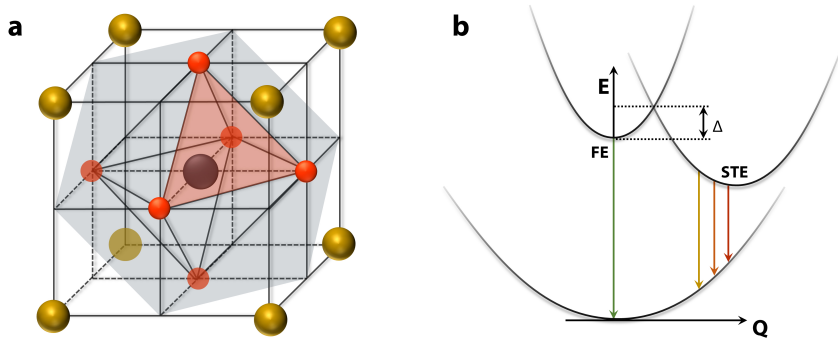

Figure 1.7
(a) Illustration of Fröhlich mechanism in an ionic cubic perovskite structure, indicating planes of negative X^- and positive M^{2+} ions, acting as capacitor plates (after [87]).**(b)** Potential energy curves of self trapped (STE) and free excitons (FE) in the configuration space. The luminescence processes are indicated and Δ denotes the potential barrier.

be expressed by different functional dependencies on the spectral width as a function of temperature [103–106], including inhomogeneous and homogeneous broadening mechanisms.

$$\Gamma(T) = \Gamma_0 + \gamma_{AC} N_{AC}(T) + \gamma_{LO} N_{LO}(T) \tag{1.42}$$

Here, T_0 is a temperature-independent inhomogeneous broadening parameter due to impurities and imperfections. The second term describes interactions with acoustic phonons and the last term takes into account LO phonon scattering, γ_{AC} and γ_{LO} are the coupling parameters respectively. The coupling is proportional to the occupation numbers and given by the Bose-Einstein distribution $N_{AC/LO}(T) = 1/\left(e^{E_{AC/LO}/k_B T} - 1\right)$. Since acoustic phonons exhibit energies much smaller than $k_B T$ their contribution can be approximated by a linear temperature dependence at finite temperatures and their coupling strength is mainly caused by the deformation potential mechanism. Eventually, a fourth term $\gamma_{imp} e^{-E_{bi}/k_B T}$ [103, 105] can be added, describing scattering from ionized impurities with an average binding energy E_{bi}.

In addition to the large polaron picture above, electron-phonon coupling can result in the formation of small polarons, strongly localized over a few lattice sites, which is energetically favored in the presence of shallow defect states. Recent theoretical [107, 108] and experimental [109, 110] work suggests, that small polarons appear in HOIPs which implies to consider a molecular-like picture to explain the optical properties in this class of materials.

In general, the Hamiltonian describing an atomic system of N electrons and M nuclei takes the

explicit form

$$\hat{\mathcal{H}} = -\frac{\hbar^2}{2m}\sum_{i=1}^{N}\nabla_i^2 - \frac{\hbar^2}{2}\sum_{k=1}^{M}\frac{\nabla_k^2}{M_k} - \sum_{i,k=1}^{M,N}\frac{Z_k e^2}{|\vec{r}_i - \vec{R}_k|} + \sum_{\substack{i=1\\ j<i}}^{N,N}\frac{e^2}{|\vec{r}_i - \vec{r}_j|} + \sum_{\substack{k=1\\ l<k}}^{M,M}\frac{Z_k Z_l e^2}{|\vec{R}_k - \vec{R}_l|} \tag{1.43}$$

where the first two terms represent the kinetic energy of electrons and nuclei respectively, the other terms describe the interaction potentials of the constituents, in particular, electrons and nuclei, between electrons and between nuclei respectively. Here $\vec{R}$ stands for the nuclear and $\vec{r}$ for the electronic coordinates. The corresponding Schrödinger equation can be solved exactly only for the most simple system, the hydrogen molecule. In all other cases, especially in the case of highly complex systems like semiconductors suitable approximations are indispensable to keep the problem tractable.

1.4.2 Born-Oppenheimer approximation

Starting from the above Hamiltonian, the solution of the Schrödinger equation depends on two coordinates, the spatial coordinates of the electrons and nuclei. The Born-Oppenheimer approximation simplifies the complex interplay between the constituents by assuming that the motion of the nuclei with respect to the electronic motion is sufficiently slow, to consider them effectively static when describing electronic movements. This presumption is based on the fact, that the mass ratio between electrons and nuclei is in the order of 0.1%. It allows to decouple the dynamics of nuclei and electrons and to factorize the wave-function ansatz $\Psi(\vec{r},\vec{R}) = \varphi_{\mathrm{e}}(\vec{r},\vec{R})\psi_{\mathrm{n}}(\vec{R})$. As a consequence, the solutions change when the nuclei move but electrons arrange quasi instantaneously without influencing the positions of the nuclei [11]. In the Born Oppenheimer approximation, the electronic part is repeatedly solved slowly varying the nuclear coordinates to return the electronic potential surfaces. Due to the complexity of involving the interaction potentials, different analytical and numerical methods are usually applied which make further simplifications (e. g. density functional theory (DFT), Hatree-Fock, etc.). After defining the nuclear potentials (common choices encompass the harmonic or Morse potential) the nuclear part can be solved and the final result contains a manifold of nuclear sub-levels within each electronic level. The solutions are usually displayed in configurational coordinates Q_i for the normal modes of the lattice, hence distinct electronic states have different equilibrium positions.

1.4.3 Frank-Condon principle

The Frank-Condon approximation states, that all optical transitions are vertical with respect to the configurational coordinate, thus there is no nuclear dependence for the transition dipole operator. Subsequently, the matrix element for the transition between ground and excited

[11] The formalism is also referred to as adiabatic approximation.

states Ψ_g, Ψ_e results to

$$M_{1,2} \propto \int \varphi_e(\vec{r})^* \mu \varphi_g(\vec{r}) dr^3 \times \int \psi_m^* \psi_n dQ \tag{1.44}$$

The first factor describes the dipole moment for the electronic transition $\mu_{eg} = \int \varphi_e(\vec{r})^* \mu \varphi_g(\vec{r}) dr^3$ and is evaluated at the equilibrium position of the initial state. The second factor represents the overlap integral between the initial and final vibrational wave functions. According to Fermi's golden rule [68], the transition rate is proportional to the square of the matrix element, hence, the absorption cross section results to

$$\begin{aligned} \sigma_{abs}(\omega) &= |\mu_{eg}|^2 \times \sum_{n=0}^{\infty} | \int \psi_n^* \psi_0 dQ|^2 \delta(\omega - \omega_{eg} - n\omega_0) \\ \sigma_{abs}(\omega) &= |\mu_{eg}|^2 \times \sum_{n=0}^{\infty} F_{0,n} \delta(\omega - \omega_{eg} - n\omega_0) \end{aligned} \tag{1.45}$$

The absorption spectrum consists of a progression of regularly spaced transitions, rising from ω_{eg}, separated by ω_0 with a distribution of intensities given by the Franck-Condon coefficients $F_{0,n}$, which can be expressed as

$$F_{0,n} = \frac{e^{-S} S^n}{n!}. \tag{1.46}$$

and describe a Poissonian intensity distribution around an average S. S represents the strength of the electron-phonon coupling and is called Huang-Rhys factor. It is related to the spatial displacement q of the conformational coordinate via

$$S = \frac{q^2 m \omega_0}{2\hbar} \tag{1.47}$$

The expression 1.45 can be extended to j phonons (j=1,2,...N) with n_j modes and results to

$$\sigma_{abs}(\omega) = |\mu_{eg}|^2 \times \sum_{n_j} \delta \left[\omega - \left(\omega_{eg} + \sum_j n_j \omega_j \right) \right] \prod_j F_{0,n_j}^j \tag{1.48}$$

Let us discuss the consequences on the optical properties (see Figure 1.8). If we do not have electron-phonon coupling ($S = 0$) both electronic states can be described by one single configuration coordinate and only transitions between the same vibrational levels in ground and excited state are optically allowed, leading to a single observable transition for absorption and emission (Fig. 1.8 (b)). In the case of electron-phonon coupling ($S > 0$) the Frank Condon factors become non-zero for transitions between ground and excited vibrational states of different indices and redistribute the oscillator strength of the purely electronic transition according to

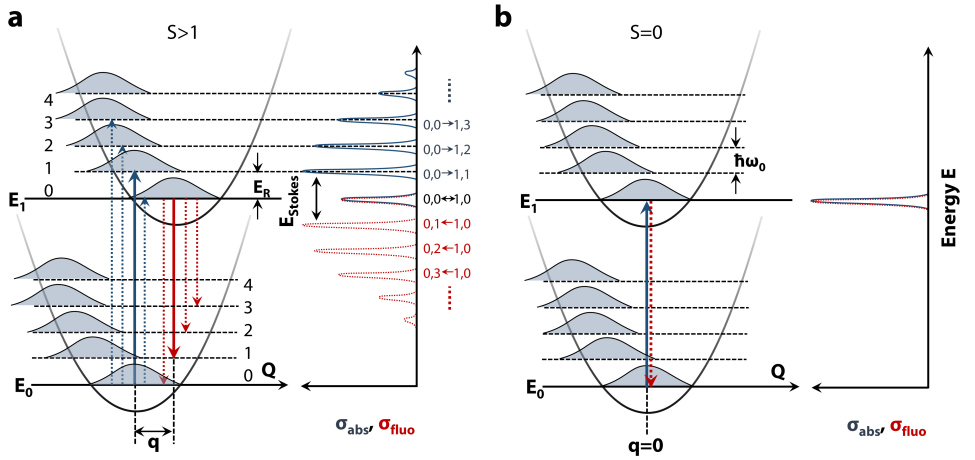

Figure 1.8
A configuration coordinate sketch of two electronic states (in harmonic approximation) with **(a)** large displacement and therefore strong electron-phonon coupling. Vibronic progressions give rise to structured absorption and emission bands at cryogenic temperatures. At room temperature, these bands are usually heavily broadened. **(b)** shows no displacement (zero electron-phonon coupling) and single transitions for absorption and emission.

the overlap between initial and final vibrational wavefunctions [12].
Higher vibrational sublevels, directly populated by absorption of a phonon relax quickly through phonon emission to the lowest vibronic state. Since this process is in general much faster than spontaneous emission, photoluminescence usually occurs from the lowest occupied vibrational level of the excited state [13]. The allowed transitions to the ground state are dictated by the same selection rules valid for the absorption and lead to a comparable vibronic progression appearing in the emission spectra. The maximum in emission are red shifted by the so called Stokes shift, which is directly related to the reorganization energy (compare E_R in Fig. 1.8) due to vibrational relaxation. If ground and excited state are described with the same Frank Condon factors, emission and absorption bands will be mirror images of each other with the zero-phonon line (transition between the vibrational ground states) as symmetry plane [111]. Note, that so far we have presumed that all transitions take place from the vibrational ground state $m = 0$ to various vibrational final states n, which is only true in case of negligible thermal occupation $\hbar\omega_i \gg k_B T$. Keil *et al.* [112] have derived the overlap integral for the case that initial and excited electronic states have equal vibrational energy. The corresponding Frank Condon factors result to

$$F_{n,m} = \left| \int \psi_m^* \psi_n dQ \right|^2 = e^{-S} S^{n-m} \left(\frac{m!}{n!} \right) \left(L_m^{n-m}(S) \right)^2 \tag{1.49}$$

[12] Other selection rules, e. g. given by the spin, that have not been taken into account in this simplistic picture can have stronger impact on the final spectral shape
[13] This principle is also known as Kasha's rule

with L_m^{n-m} being the associated Laguerre polynomials. At finite temperatures, certain vibrational states $m > 0$ can be occupied and the corresponding populations follow a Boltzmann distribution $p(m) \propto e^{m/k_B T}$. The spectrum contains transitions from every occupied state m to every accessible final state n. If the broadening is sufficiently low to resolve the single vibronic replicas, thermal occupation results in the appearance of Anti-Stokes lines in the spectra. Thermal broadening leads to wider bands and slightly shifted absorption and emission maxima in comparison to the case when thermal occupation is neglected.
Although the Frank Condon principle can be used in its strict form solely to describe electronic transitions involving vibrational levels in molecules, it is routinely extended to describe the interaction of phonons with impurity centers and localized states in solids [87].

1.4.4 Exciton self-trapping

Impurities in a semiconductor form efficient potential wells which can trap excitons [87]. These bound excitons exhibit very narrow band luminescence features (FWHM ~ 0.1 meV) that do not broaden with temperature due to the loss in kinetic energy. Furthermore, their luminescence is characterized by a so-called 'giant oscillator strength' [113] and a concomitant decrease in lifetime. The luminescence intensity scales linear with excitation density and saturates at higher densities. Since the exciton loses kinetic energy in the trapping process, these features are spectrally situated at lower energies than the free exciton emission.
In polar semiconductors with strong electron-phonon coupling, exciton trapping can occur even in defect free and unperturbed crystals. This phenomenon is referred to as self-trapping or auto-localization [87]. Whereas the luminescence from excitons bound to an impurity center represents the typical case of an extrinsic luminescence process, emission from self-trapped excitons (STE) constitutes an intrinsic process. The strong exciton-phonon coupling results in broad luminescence features.

For self-trapping localization must occur. The translational movement of an exciton is determined by its heavier constituent, usually the hole. If the polaron coupling constant α is high, the propagation of the exciton through the crystal will be slow and therefore the carriers strongly polarize the surrounding lattice. This further leads to an increase of mass and decrease of speed till total localization at one lattice site can take place. The lighter electron will therefore orbit in close vicinity (small polaron formation). According to Song [114] self-trapping is not only mediated by long range polarizations with large ion displacements (a considerable fraction of the lattice constant) but also by short-range forces (mainly covalent molecular bonding) causing the redistribution of the lattice in close vicinity of the exciton with a relaxation energy $E_R^s = S\hbar\omega$, where S is the already discussed Huang-Rhys factor. The trapped exciton can be assigned an effective mass $m_{STE} = m^* e^S$, with the free exciton mass m^*. As a consequence, for strong electron-phonon coupling ($S \gg 1$) the mass goes towards infinity.
Short range electron-phonon coupling is fundamentally different from Fröhlich interactions, it involves coupling to acoustic phonons and depends on the deformation potential of the material [114]. In the absence of short-range interactions, self-trapping cannot take place, the

exciton will remain free albeit accompanied by a phonon cloud which increases its effective mass. The energy of the vibrational local modes of the lattice site at which the exciton gets localized has to be higher than the highest LO phonon mode, not to spread the localized energy over the whole lattice [87]. Self-trapping depends on the dimensionality of the system, which can be understood by considering the simple analogue of the three dimensional quantum mechanical potential well that exhibits bound states only for a certain potential depth whereas in the one-dimensional case at least one bound state is always possible. Therefore, in three dimensional systems a minimum distortion has to be given to promote self-trapping and shallow defects usually contribute to localization effects, referred to as extrinsic self-trapping. Free excitons and self trapped excitons can coexist as stable or metastable state. In a configurational coordinate model, their potential surfaces in this case are separated by a potential barrier and their interplay in the photoluminescence properties exhibits a characteristic temperature dependence [114] (see Fig. 1.7 (b)).

References

[1] H. Topsøe, A. Arzruni, and G. v. Bath. "XVI. Auszüge". In: *Zeitschrift für Kristallographie-Crystalline Materials* 8.1-6 (1884), pp. 246–320.

[2] R. Wyckoff. "The crystal structures of monomethyl ammonium chlorostannate and chloroplatinate". In: *American Journal of Science* 94 (1928), pp. 349–359.

[3] D. Weber. "$CH_3NH_3PbX_3$, ein Pb (II)-system mit kubischer Perowskitstruktur/ $CH_3NH_3PbX_3$, a Pb (II)-system with cubic perovskite structure". In: *Zeitschrift für Naturforschung B* 33.12 (1978), pp. 1443–1445.

[4] A. Raaen, I. Svare, and M. Fibich. "Proton Resonance and Critical Relaxation in NH_4MnF_3 and NH_4ZnF_3". In: *Physica Scripta* 25.6B (1982), p. 957.

[5] H. Fuess et al. "A new ferroelectric compound: Methylammonium trichloromercurate ($CH_3NH_3HgCl_3$)". In: *Solid state communications* 56.1 (1985), pp. 137–139.

[6] T. Ishihara, J. Takahashi, and T. Goto. "Optical properties due to electronic transitions in two-dimensional semiconductors $(C_nH_{2n+1}NH_3)_2PbI_4$". In: *Physical review B* 42.17 (1990), p. 11099.

[7] J. Calabrese et al. "Preparation and characterization of layered lead halide compounds". In: *Journal of the American Chemical Society* 113.6 (1991), pp. 2328–2330.

[8] G. C. Papavassiliou et al. "Spectroscopic studies of $(C_{10}H_{21}NH_3)_2PbI_4$, $(CH_3NH_3)(C_{10}H_{21}NH_3)_2Pb_2I_7$, $(CH_3NH_3)PbI_3$, and similar compounds". In: *Synthetic metals* 57.1 (1993), pp. 3889–3894.

[9] T. Ishihara. "Optical properties of PbI-based perovskite structures". In: *Journal of luminescence* 60 (1994), pp. 269–274.

[10] D. Mitzi et al. "Conducting layered organic-inorganic halides containing (110)-oriented perovskite sheets". In: *Science* (1995), pp. 1473–1473.

[11] G. C. Papavassiliou, G. A. Mousdis, and I. Koutselas. "Some new organic–inorganic hybrid semiconductors based on metal halide units: structural, optical and related properties". In: *Advanced Functional Materials* 9.6 (1999), pp. 265–271.

[12] T. Hattori et al. "Highly efficient electroluminescence from a heterostructure device combined with emissive layered-perovskite and an electron-transporting organic compound". In: *Chemical physics letters* 254.1-2 (1996), pp. 103–108.

[13] T. Gebauer and G. Schmid. "Inorganic-organic Hybrid Structured LED's". In: *Zeitschrift für anorganische und allgemeine Chemie* 625.7 (1999), pp. 1124–1128.

[14] C. Kagan, D. Mitzi, and C. Dimitrakopoulos. "Organic-inorganic hybrid materials as semiconducting channels in thin-film field-effect transistors". In: *Science* 286.5441 (1999), pp. 945–947.

[15] D. B. Mitzi, C. D. Dimitrakopoulos, and L. L. Kosbar. "Structurally tailored organic-inorganic perovskites: optical properties and solution-processed channel materials for thin-film transistors". In: *Chemistry of materials* 13.10 (2001), pp. 3728–3740.

[16] A. Kojima et al. "Novel photoelectrochemical cell with mesoscopic electrodes sensitized by lead-halide compounds (2)". In: *Meeting Abstracts*. 7. The Electrochemical Society. 2006, pp. 397–397.

[17] A. Kojima et al. "Organometal halide perovskites as visible-light sensitizers for photovoltaic cells". In: *Journal of the American Chemical Society* 131.17 (2009), pp. 6050–6051.

[18] J.-H. Im et al. "6.5% efficient perovskite quantum-dot-sensitized solar cell". In: *Nanoscale* 3.10 (2011), pp. 4088–4093.

[19] I. Chung et al. "All-solid-state dye-sensitized solar cells with high efficiency". In: *Nature* 485.7399 (2012), p. 486.

[20] L. Etgar et al. "Mesoscopic $CH_3NH_3PbI_3/TiO_2$ heterojunction solar cells". In: *Journal of the American Chemical Society* 134.42 (2012), pp. 17396–17399.

[21] M. M. Lee et al. "Efficient hybrid solar cells based on meso-superstructured organometal halide perovskites". In: *Science* 338.6107 (2012), pp. 643–647.

[22] N. C. for Photovoltaics (NCPV). *NREL efficiency chart*. 2018. URL: `https://www.nrel.gov/pv/assets/images/efficiency-chart.png` (visited on 01/13/2018).

[23] J. Burschka et al. "Sequential deposition as a route to high-performance perovskite-sensitized solar cells". In: *Nature* 499.7458 (2013), pp. 316–319.

[24] A. A. Bakulin et al. "Real-time observation of organic cation reorientation in methylammonium lead iodide perovskites". In: *J. Phys. Chem. Lett* 6.18 (2015), pp. 3663–3669.

[25] G. Rose. "Beschreibung einiger neuen Mineralien des Urals". In: *Annalen der Physik* 126.8 (1840), pp. 652–656.

[26] A. Navrotsky and D. J. Weidner. "Perovskite: a structure of great interest to geophysics and materials science". In: *Washington DC American Geophysical Union Geophysical Monograph Series* 45 (1989).

[27] D. Damjanovic. "Piezoelectric properties of perovskite ferroelectrics: unsolved problems and future research". In: *Annales de Chimie Science des Materiaux*. Vol. 26. 1. Elsevier. 2001, pp. 99–106.

[28] Y. Moritomo et al. "Giant magnetoresistance of manganese oxides with a layered perovskite structure". In: *Nature* 380.6570 (1996), pp. 141–144.

[29] U. Eibenstein and W. Jung. "Li_2Pd_3B and Li_2Pt_3B: Ternary lithium borides of palladium and platinum with boron in octahedral coordination". In: *Journal of Solid State Chemistry* 133.1 (1997), pp. 21–24.

[30] M. Pena and J. Fierro. "Chemical structures and performance of perovskite oxides". In: *Chemical reviews* 101.7 (2001), pp. 1981–2018.

[31] A. Glazer. "The classification of tilted octahedra in perovskites". In: *Acta Crystallographica Section B: Structural Crystallography and Crystal Chemistry* 28.11 (1972), pp. 3384–3392.

[32] V. Goldschmidt. "Krystallbau und chemische Zusammensetzung". In: *European Journal of Inorganic Chemistry* 60.5 (1927), pp. 1263–1296.

[33] C. Li et al. "Formability of ABX_3 (X= F, Cl, Br, I) Halide Perovskites". In: *Acta Crystallographica Section B: Structural Science* 64.6 (2008), pp. 702–707.

[34] D. B. Mitzi, K. Chondroudis, and C. R. Kagan. "Organic-inorganic electronics". In: *IBM journal of research and development* 45.1 (2001), pp. 29–45.

[35] B. Saparov and D. B. Mitzi. "Organic–inorganic perovskites: structural versatility for functional materials design". In: *Chem. Rev.* 116.7 (2016), pp. 4558–4596.

[36] D. B. Mitzi. "Templating and structural engineering in organic–inorganic perovskites". In: *Journal of the Chemical Society, Dalton Transactions* 1 (2001), pp. 1–12.

[37] D. B. Mitzi. "Synthesis, structure, and properties of organic-inorganic perovskites and related materials". In: *Progress in Inorganic Chemistry, Volume 48* (2007), pp. 1–121.

[38] J. Even et al. "Solid-state physics perspective on hybrid perovskite semiconductors". In: *The Journal of Physical Chemistry C* 119.19 (2015), pp. 10161–10177.

[39] J. Even et al. "Electronic model for self-assembled hybrid organic/perovskite semiconductors: Reverse band edge electronic states ordering and spin-orbit coupling". In: *Physical Review B* 86.20 (2012), p. 205301.

[40] J. Even, L. Pedesseau, and C. Katan. "Analysis of multivalley and multibandgap absorption and enhancement of free carriers related to exciton screening in hybrid perovskites". In: *The Journal of Physical Chemistry C* 118.22 (2014), pp. 11566–11572.

[41] E. Mosconi et al. "First-principles modeling of mixed halide organometal perovskites for photovoltaic applications". In: *The Journal of Physical Chemistry C* 117.27 (2013), pp. 13902–13913.

[42] K. Tanaka et al. "Comparative study on the excitons in lead-halide-based perovskite-type crystals $CH_3NH_3PbBr_3$ $CH_3NH_3PbI_3$". In: *Solid state communications* 127.9 (2003), pp. 619–623.

[43] E. T. Hoke et al. "Reversible photo-induced trap formation in mixed-halide hybrid perovskites for photovoltaics". In: *Chemical Science* 6.1 (2015), pp. 613–617.

[44] A. J. Barker et al. "Defect-Assisted Photoinduced Halide Segregation in Mixed-Halide Perovskite Thin Films". In: *ACS Energy Letters* 2.6 (2017), pp. 1416–1424.

[45] D. P. McMeekin et al. "A mixed-cation lead mixed-halide perovskite absorber for tandem solar cells". In: *Science* 351.6269 (2016), pp. 151–155.

[46] Z. Xiao et al. "Mixed-halide perovskites with stabilized bandgaps". In: *Nano Letters* 17.11 (2017), pp. 6863–6869.

[47] Y. P. Varshni. "Temperature dependence of the energy gap in semiconductors". In: *physica* 34.1 (1967), pp. 149–154.

[48] A. Olkhovets et al. "Size-dependent temperature variation of the energy gap in lead-salt quantum dots". In: *Physical review letters* 81.16 (1998), p. 3539.

[49] A. R. Srimath Kandada and A. Petrozza. "Photophysics of hybrid lead halide perovskites: the role of microstructure". In: *Accounts of chemical research* 49.3 (2016), pp. 536–544.

[50] C. C. Stoumpos and M. G. Kanatzidis. "The renaissance of halide perovskites and their evolution as emerging semiconductors". In: *Accounts of chemical research* 48.10 (2015), pp. 2791–2802.

[51] C. Quarti et al. "The Raman spectrum of the $CH_3NH_3PbI_3$ hybrid perovskite: interplay of theory and experiment". In: *The journal of physical chemistry letters* 5.2 (2013), pp. 279–284.

[52] A. Amat et al. "Cation-induced band-gap tuning in organohalide perovskites: interplay of spin–orbit coupling and octahedra tilting". In: *Nano letters* 14.6 (2014), pp. 3608–3616.

[53] V. D'Innocenzo et al. "Tuning the light emission properties by band gap engineering in hybrid lead halide perovskite". In: *Journal of the American Chemical Society* 136.51 (2014), pp. 17730–17733.

[54] G. Grancini et al. "Role of microstructure in the electron–hole interaction of hybrid lead halide perovskites". In: *Nature photonics* 9.10 (2015), pp. 695–701.

[55] J. Even, L. Pedesseau, and C. Katan. "Understanding quantum confinement of charge carriers in layered 2D hybrid perovskites". In: *ChemPhysChem* 15.17 (2014), pp. 3733–3741.

[56] X. Hong, T. Ishihara, and A. Nurmikko. "Dielectric confinement effect on excitons in PbI_4-based layered semiconductors". In: *Physical Review B* 45.12 (1992), p. 6961.

[57] E. Muljarov et al. "Excitons in self-organized semiconductor/insulator superlattices: PbI-based perovskite compounds". In: *Physical Review B* 51.20 (1995), p. 14370.

[58] Y. Kato et al. "Extremely large binding energy of biexcitons in an organic–inorganic quantum-well material $(C_4H_9NH_3)_2PbBr_4$". In: *Solid state communications* 128.1 (2003), pp. 15–18.

[59] A. Einstein. "Zur quantentheorie der strahlung". In: *Phys. Z.* 18 (1917), pp. 121–128.

[60] H. Haug and S. W. Koch. *Quantum theory of the optical and electronic properties of semiconductors*. World Scientific, 1990.

[61] J. Shah. *Ultrafast spectroscopy of semiconductors and semiconductor nanostructures*. Vol. 115. Springer Science & Business Media, 2013.

[62] Y. Yang et al. "Observation of a hot-phonon bottleneck in lead-iodide perovskites". In: *Nature Photonics* 10.1 (2016), pp. 53–59.

[63] J. Fu et al. "Hot carrier cooling mechanisms in halide perovskites". In: *Nature communications* 8.1 (2017), p. 1300.

[64] H. Haug and S. Schmitt-Rink. "Electron theory of the optical properties of laser-excited semiconductors". In: *Progress in Quantum Electronics* 9.1 (1984), pp. 3–100.

[65] S. Permogorov. "Hot excitons in semiconductors". In: *physica status solidi (b)* 68.1 (1975), pp. 9–42.

[66] S. Lyon. "Spectroscopy of hot carriers in semiconductors". In: *Journal of luminescence* 35.3 (1986), pp. 121–154.

[67] P. Y. Yu and M. Cardona. *Fundamentals of semiconductors: physics and materials properties*. Springer, 2010.

[68] N. W. Ashcroft and D. N. Mermin. *Solid State Physics*. Brooks Cole, 1976.

[69] C. Cohen-Tannoudji, B. Diu, and F. Laloë. *Quantum Mechanics*. Wiley NY, 1977.
[70] R. Eisberg and R. Resnick. *Quantum physics*. John Wiley New York, 1974.
[71] R. Elliott. "Intensity of optical absorption by excitons". In: *Physical Review* 108.6 (1957), p. 1384.
[72] M. Sturge. "Optical absorption of gallium arsenide between 0.6 and 2.75 eV". In: *Physical Review* 127.3 (1962), p. 768.
[73] Q. Lin et al. "Electro-optics of perovskite solar cells". In: *Nature Photonics* 9.2 (2015), pp. 106–112.
[74] V. D'Innocenzo et al. "Excitons versus free charges in organo-lead tri-halide perovskites". In: *Nature communications* 5 (2014), p. 3586.
[75] A. Miyata et al. "Direct measurement of the exciton binding energy and effective masses for charge carriers in organic-inorganic tri-halide perovskites". In: *Nature Physics* 11.7 (2015), pp. 582–587.
[76] D. A. Valverde-Chávez et al. "Intrinsic femtosecond charge generation dynamics in single crystal $CH_3NH_3PbI_3$". In: *Energy & Environmental Science* 8.12 (2015), pp. 3700–3707.
[77] A. R. S. Kandada et al. "Photophysics of Hybrid Perovskites". In: *Unconventional Thin Film Photovoltaics*. Royal Society of Chemistry, 2016, pp. 107–140.
[78] L. M. Herz. "Charge-carrier dynamics in organic-inorganic metal halide perovskites". In: *Annual review of physical chemistry* 67 (2016), pp. 65–89.
[79] M. N. Saha. "On a physical theory of stellar spectra". In: *Proceedings of the Royal Society of London. Series A, Containing Papers of a Mathematical and Physical Character* 99.697 (1921), pp. 135–153.
[80] W. Kraeft, K. Kilimann, and D. Kremp. "Quantum statistics of an electron–hole plasma". In: *physica status solidi (b)* 72.2 (1975), pp. 461–474.
[81] P. van Dongen. "Grundlagen der Statistischen Physik". In: *Statistische Physik*. Springer, 2017, pp. 97–126.
[82] R. Gilmore. "Saha's Equation and the Partition Function". In: *URL http://www. physics. drexel. edu/~ bob/PHYS317_08/saha. pdf* ().
[83] J. S. Manser and P. V. Kamat. "Band filling with free charge carriers in organometal halide perovskites". In: *Nature Photonics* 8.9 (2014), pp. 737–743.
[84] M. Saba et al. "Correlated electron–hole plasma in organometal perovskites". In: *Nature communications* 5 (2014), p. 5049.
[85] N. Mott. "On metal-insulator transitions". In: *Journal of Solid State Chemistry* 88.1 (1990), pp. 5–7.
[86] Y. Yamada et al. "Spontaneous defect annihilation in $CH_3NH_3PbI_3$ thin films at room temperature revealed by time-resolved photoluminescence spectroscopy". In: *The journal of physical chemistry letters* 6.3 (2015), pp. 482–486.
[87] I. Pelant and J. Valenta. *Luminescence spectroscopy of semiconductors*. Oxford University Press, 2012.
[88] R. L. Milot et al. "Temperature-Dependent Charge-Carrier Dynamics in $CH_3NH_3PbI_3$ Perovskite Thin Films". In: *Advanced Functional Materials* 25.39 (2015), pp. 6218–6227.

[89] C. Wehrenfennig et al. "High charge carrier mobilities and lifetimes in organolead trihalide perovskites". In: *Advanced materials* 26.10 (2014), pp. 1584–1589.
[90] W. Shockley and W. Read Jr. "Statistics of the recombinations of holes and electrons". In: *Physical review* 87.5 (1952), p. 835.
[91] Y. Tian et al. "Mechanistic insights into perovskite photoluminescence enhancement: light curing with oxygen can boost yield thousandfold". In: *Physical Chemistry Chemical Physics* 17.38 (2015), pp. 24978–24987.
[92] W. Zhang et al. "Photo-induced halide redistribution in organic–inorganic perovskite films". In: *Nature communications* 7 (2016), p. 11683.
[93] S. G. Motti et al. "Photoinduced emissive trap states in lead halide perovskite semiconductors". In: *ACS Energy Letters* 1.4 (2016), pp. 726–730.
[94] S. D. Stranks et al. "Recombination kinetics in organic-inorganic perovskites: excitons, free charge, and subgap states". In: *Physical Review Applied* 2.3 (2014), p. 034007.
[95] P. T. Landsberg. "The band-band Auger effect in semiconductors". In: *Solid-State Electronics* 30.11 (1987), pp. 1107–1115.
[96] M. Takeshima. "Unified theory of the impurity and phonon scattering effects on Auger recombination in semiconductors". In: *Physical Review B* 25.8 (1982), p. 5390.
[97] J. Nelson. *The physics of solar cells*. World Scientific Publishing Co Inc, 2003.
[98] A. R. Srimath Kandada and A. Petrozza. "Research Update: Luminescence in lead halide perovskites". In: *APL Materials* 4.9 (2016), p. 091506.
[99] X.-Y. Zhu and V. Podzorov. *Charge carriers in hybrid organic–inorganic lead halide perovskites might be protected as large polarons*. 2015.
[100] G.-J. A. Wetzelaer et al. "Trap-assisted non-radiative recombination in organic–inorganic perovskite solar cells". In: *Advanced Materials* 27.11 (2015), pp. 1837–1841.
[101] H. T. Yi et al. "Intrinsic Charge Transport across Phase Transitions in Hybrid Organo-Inorganic Perovskites". In: *Advanced Materials* 28.30 (2016), pp. 6509–6514.
[102] K. Galkowski et al. "Determination of the exciton binding energy and effective masses for methylammonium and formamidinium lead tri-halide perovskite semiconductors". In: *Energy & Environmental Science* 9.3 (2016), pp. 962–970.
[103] A. D. Wright et al. "Electron–phonon coupling in hybrid lead halide perovskites". In: *Nature communications* 7 (2016).
[104] S. Rudin, T. Reinecke, and B. Segall. "Temperature-dependent exciton linewidths in semiconductors". In: *Physical Review B* 42.17 (1990), p. 11218.
[105] J. Lee, E. S. Koteles, and M. Vassell. "Luminescence linewidths of excitons in GaAs quantum wells below 150 K". In: *Physical Review B* 33.8 (1986), p. 5512.
[106] X. Zhang et al. "Influence of electron-phonon interaction on the optical properties of III nitride semiconductors". In: *Journal of Physics: Condensed Matter* 13.32 (2001), p. 7053.
[107] M. H. Du. "Efficient carrier transport in halide perovskites: theoretical perspectives". In: *Journal of Materials Chemistry A* 2.24 (2014), pp. 9091–9098.
[108] A. J. Neukirch et al. "Polaron stabilization by cooperative lattice distortion and cation rotations in hybrid perovskite materials". In: *Nano letters* 16.6 (2016), pp. 3809–3816.

[109] T. Hu et al. "Mechanism for broadband white-light emission from two-dimensional (110) hybrid perovskites". In: *The journal of physical chemistry letters* 7.12 (2016), pp. 2258–2263.

[110] D. Cortecchia et al. "Polaron self-localization in white-light emitting hybrid perovskites". In: *Journal of Materials Chemistry C* 5.11 (2017), pp. 2771–2780.

[111] M. de Jong et al. "Resolving the ambiguity in the relation between Stokes shift and Huang–Rhys parameter". In: *Physical Chemistry Chemical Physics* 17.26 (2015), pp. 16959–16969.

[112] T. H. Keil. "Shapes of impurity absorption bands in solids". In: *Physical Review* 140.2A (1965), A601.

[113] E. Rashba. "Giant oscillator-strengths associated with exciton complexes". In: *SOVIET PHYSICS SEMICONDUCTORS-USSR* 8.7 (1975), pp. 807–816.

[114] K. Song and R. T. Williams. *Self-trapped excitons*. Vol. 105. Springer Science & Business Media, 2013.

Chapter 2

Methods

The chapter provides a brief introduction into the field of spectroscopy explaining the common optical characterization techniques of the PhD research with focus on the custom-built setups for nonlinear spectroscopy and an overview of the employed sample fabrication procedures.

2.1 Optical spectroscopy

The term optical spectroscopy relates all techniques using light to investigate matter, in particular, the influence of matter on the broad spectrum of electro-magnetic radiation. Hence each method offers a different perspective on the system of interest. The material property that couples to an incoming radiation field is the optical polarization of the material, the ensemble average over the driven individual oscillating molecular dipoles. Mathematically, it can be described perturbatively as power series of the field of the incident electromagnetic radiation.

$$P(t) = P^{(1)}(t) + P^{(2)}(t) + P^{(3)}(t) + \ldots = \sum_{j=1}^{\infty} \chi^{(j)} E^j(t) \tag{2.1}$$

where $P^{(1)}$, $P^{(2)}, \ldots$ depend linearly, quadratically, etc. on the electric field respectively, and $\chi^{(j)}$ are the susceptibilities. The induced macroscopic polarization serves as source term in the electro-magnetic wave equation and defines the response of the material system [1].

$$\vec{\nabla}^2 \vec{E}(\vec{r}, t) - \frac{1}{c^2} \frac{\partial \vec{E}(\vec{r}, t)}{\partial t^2} = \frac{4\pi}{c^2} \frac{\partial \vec{P}(\vec{r}, t)}{\partial t^2} \tag{2.2}$$

In linear spectroscopy we take advantage of light-matter interactions with a sufficiently weak incident radiation field, which allows to treat the interaction as a linear response between light and matter, e. g. to retain solely the linear term in equation 2.1. In contrast, non-linear spectroscopy comprises the case when the incident radiation field is too strong to neglect higher

order terms in equation 2.1 to describe the coupling of light an matter and the case of multiple electro-magnetic fields interacting with the material. Additionally, depending on the type of signal we are monitoring we distinguish between coherent and spontaneous spectroscopy. In coherent spectroscopy, we detect the constructively interfering signal of the coherently driven macroscopic polarization along a well-defined direction which encompasses experiments like pump-probe, transient grating and higher dimensional spectroscopic techniques. Spontaneous spectroscopy deals with the signal radiated from independently oscillating dipoles in the sample and refers to fluorescence and phosphorescence spectroscopy, light scattering experiments as well as nonlinear techniques like stimulated emission pumping or excitation correlation photoluminescence spectroscopy.

2.2 Linear optical spectroscopy

If the response of a material is linearly dependent on the electric field it can be expressed in terms of a linear susceptibility $\chi^{(1)}$.

$$P(t) = \chi^{(1)} E(t) \tag{2.3}$$

Considering the classical picture, in which electrons are bound by harmonic forces to the positively charged atomic nuclei [2], we can describe the motion of an electron e in an electric field $E(t)$ as a damped driven harmonic oscillator. Hence, the linear susceptibility results to

$$\chi^{(1)}(\omega) = \frac{n_0 e^2}{m_0} \cdot \frac{1}{\omega_0^2 - i\gamma\omega - \omega^2} \tag{2.4}$$

where n_0 is the electron density, γ the damping constant and m_0 and ω_0 are the oscillator mass and resonance frequency respectively. The imaginary part indicates, that the response of the material has a certain phase relation with the incoming driving field. When excited resonantly, the induced polarization radiates a second field which is out of phase with the incoming radiation. In this classical picture, absorption can be understood due to destructive interference between the two electro-magnetic waves. In the following, a short overview of the linear spectroscopic techniques will be given.

2.2.1 UV-vis spectroscopy

The majority of absorbance spectra in this thesis were recorded with a commercial UV-VIS-NIR spectrophotometer (PerkinElmer Lambda 1050) using a spectral resolution of about 1 nm. All spectra are corrected for the absorbance of the substrate when using thin films and solvent absorbance for solutions. In order to give an initial estimate of the excitation densities in the material, the penetration depth of the measured films and therefore the absorption coefficient has to be determined accurately. For this purpose, the total I_0, transmitted I_T and

reflected I_R intensities are measured with an integrating sphere module and the penetration depth calculated δ_p following Lambert Beer's law:

$$I_T = (I_0 - I_R)e^{-\alpha d} \tag{2.5}$$

$$\delta_p(\lambda) = \alpha(\lambda)^{-1} = -\frac{d}{\ln(I_T(\lambda)/(I_0(\lambda) - IR(\lambda)))} \tag{2.6}$$

d is the film thickness, normally determined via SEM cross-section or profilometer measurements. Assuming that all incident photons are absorbed within a volume given by the spot size A_{pump} of the incident radiation and the penetration depth, the excitation density results to

$$n_0 = \frac{P_{CW} \cdot \lambda_{\text{pump}}}{RR \cdot hc \cdot A_{\text{pump}} \cdot \delta_p(\lambda_{\text{pump}})} \tag{2.7}$$

with the repetition rate of the laser RR and the incident power P_{CW}.

2.2.2 Photoluminescence spectroscopy

The excitation light source for power dependent photoluminescence measurements consists of the fs laser system described in the transient absorption section. The pump pulses are either generated by frequency doubling the fundamental in a BBO crystal, or using the signal output of an optical parametric amplifier (OPA), depending on the desired wavelength for the material of interest. The photoluminescence from the sample is collected and focused by a lens doublet into a fiber coupled spectrometer (Ocean Optics Maya Pro 2000). Long-pass filter in front of the spectrometer prevent saturation by the scattered pump light. The pump fluences are adjusted using a gradual neutral density filter wheel. The relative photoluminescence quantum yield (PLQY) is derived by spectrally integrating the photoluminescence signal and dividing it by the respective pump power.

2.2.3 Raman spectroscopy

Raman spectroscopy can probe various low-frequency, rotational and vibrational modes in a material by detecting the scattered light from the monochromatically illuminated sample. The small part of the scattered light which is shifted in energy from the excitation energy due to interaction between vibrational modes of the material with the electro-magnetic excitation field can give useful structural information about the material of interest. The room temperature Raman spectra in this thesis were recorded under ambient conditions in backscattering configuration using a micro Raman confocal microscope (inVia Raman Microscope Renishaw, equipped with 5x, 20x,50x and 100x short and long working distance objectives, using 785 nm excitation wavelength). System calibration was performed using the 520 cm^{-1} mode of a bare

silicon wafer. Temperature dependent measurements were taken under vacuum at 718 nm excitation wavelength in a near backscattering configuration with a continuous-wave Ti:Sapphire laser (Spectra Physics, Matisse TS). In this configuration, 100 mW excitation power is distributed over a spotsize of about 1cm x 50µm with a cylindrical focussing lens. The spectrum is detected by a liquid nitrogen cooled Princeton Instruments CCD in conjunction with a Jobin-Yvon U1000 double spectrometer featuring a grating with 1800 lines per mm. The system was calibrated with the help of the spectral lines of a mercury gas lamp.

2.3 Nonlinear optical spectroscopy

Traditional linear spectroscopy can deliver microscopic information about a system in form of observables like resonance frequencies, lineshapes and oscillator strengths and we can refine our study by varying the properties of the impinging light field (frequency, amplitude, phase, polarization, etc.) and careful adjustment of sample parameters.

Nevertheless, due to its indirect nature, the interpretation of linear spectroscopic data suffers from ambiguities, especially in complex systems like disordered condensed matter with many interacting degrees of freedom which leads to convoluted or featureless spectra. As an example, we lack information about whether observed resonances belong to independent or correlated states or if the lineshape is homogeneously broadened and therefore given solely by relaxation or inhomogeneously broadened due to a distribution of different frequencies. Relying on linear spectroscopy alone, we can only measure a convolution of both lineshapes.

Time-resolved higher order nonlinear spectroscopic techniques offer the possibility to tackle these problems. Multiple light-matter interactions allow to correlate and disentangle spectral features to obtain knowledge about molecular structure and interaction. Furthermore, the introduction of controlled time delays reveals information about the temporal evolution of the system from the non-equilibrium to the equilibrium state.

2.3.1 Transient absorption spectroscopy

Transient absorption (TA), also called pump-probe spectroscopy is probably the most widely used third order nonlinear technique. In the process, the material is first excited by a short laser pulse and brought into a non-equilibrium condition. A temporally delayed optical probe pulse is used to detect the progression of the pump induced changes. The observables are linear responses of the probe like transmission, reflection, Raman scattering or the polarization state and the resulting signal is defined as the normalized change as a function of delay [3]. The temporal resolution in a pump-probe experiment determines which regime, coherent or incoherent can be studied and is limited by the convolution between the temporal profiles of pump and probe pulses. Most experiments in this thesis address solely the population dynamics of the material system with a temporal resolution of ~120 fs. The utilized transient

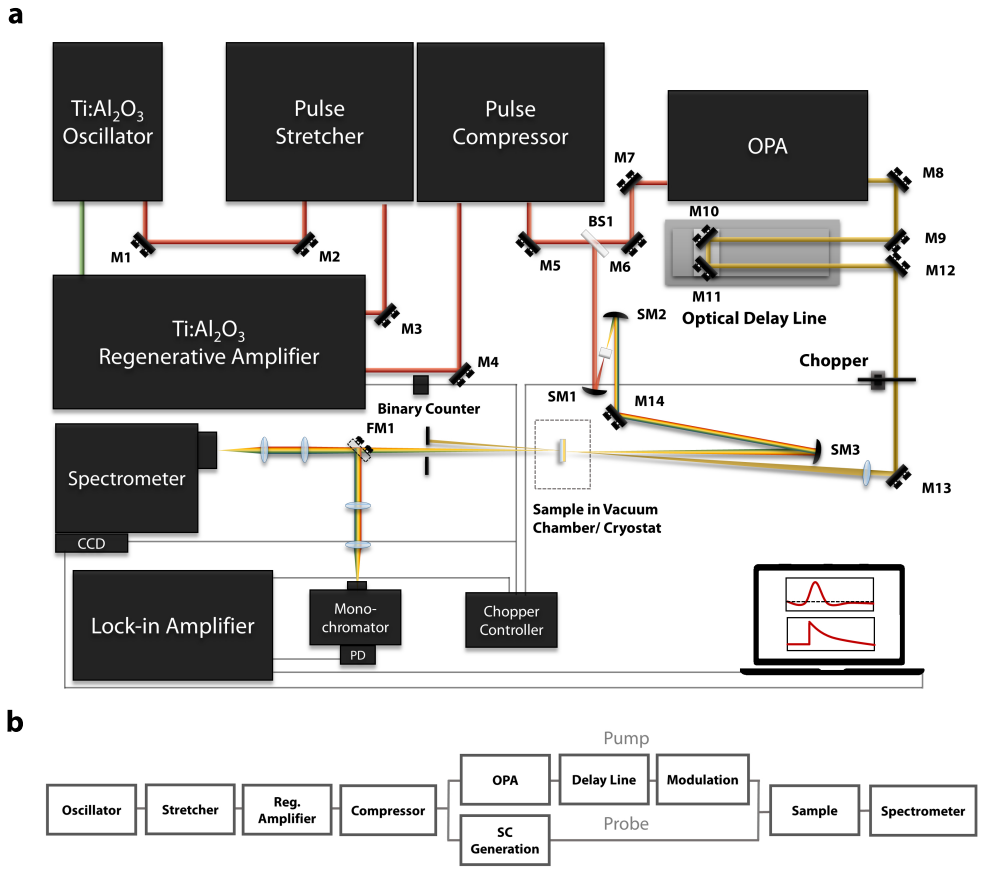

Figure 2.1
(a) Simplified optical layout of the TA-setup. **(b)** Flowchart of light generation and measurement principle (adopted from [5]).

absorption system and control software was developed mainly by Srimath Kandada [4] and others and merely adjusted to particular experiments. Therefore, only a brief description of the main components and the general measurement principle is given below.

Setup configuration

A sketch of the transient absorption setup is depicted in Figure 2.1. The fs light source powering the different nonlinear processes used to generate pump and probe light can be divided into four parts, source, stretcher, amplifier and compressor. The fundamental source consists of a passive Kerr-lens mode-locked intra-cavity $Ti:Al_2O_3$ oscillator (Coherent Micra), which provides ~20 fs pulses at 80 MHz repetition rate and 800 nm central wavelength. Before amplification, the pulses are temporally stretched in a grating based pulse stretching/compressing

unit (Coherent 9040) to lower the peak power for damage prevention and subsequently delivered to a Q-switched Ti:Al_2O_3 based regenerative amplifier (Coherent RegA 9000) running at 250 kHz. After amplification, the pulses are compressed again (Coherent 9040) resulting in a temporal width of ~35 fs and energies of roughly 6 µJ. Afterwards, the pulse train is divided by a 90:10 beam splitter to produce pump and probe light. The pump light is generated by difference-frequency processes in a collinear optical parametric amplifier (Coherent 9450) offering wavelength tuning between 480 and 750 nm with a spectral bandwidth of ~ 10-20 nm and involving a temporal broadening of around 100 fs. The probe light encompasses a spectral range from 480 to almost 1100 nm and is obtained via supercontinuum generation by focusing the lower power part of the 800 nm fundamental into a 1-2 mm thick sapphire plate [1]. The spectral region close to the fundamental is filtered out, to keep the overall power of the probe light low ensuring a small, negligible perturbation of the sample by the probe.

For pump-probe measurements, both pulses are focused and spatially as well as temporally overlapped onto the sample, whereupon the temporal delay is introduced by a computer controlled optical delay stage in the pump line of the setup. The angle between pump and probe pulse has to be as small as feasible to maximize the spatial overlap. To guarantee homogeneous sample illumination by the pump beam, the beam diameter of the probe beam on the sample is kept substantially smaller than the pump spot size. Finally, only reflective optics are used in the probe path before the sample, to minimize the spectral chirp.

The signal to be measured in our pump-probe experiment is the change in normalized transmission (or reflection) of the probe beam upon excitation of the material by the pump. Since the expected change is usually small with respect to the background given by the total intensity of the transmitted probe spectrum, a heterodyne detection scheme is commonly applied. In the typical measurement configurations the transmitted spectrum is measured either wavelength by wavelength using a lock-in amplifier (Stanford Research Systems, SR830) in conjunction with a monochromator and slow photodiode or in a single shot with a customized Stresing silicon based CCD array, equipped with an electronic shutter to adjust to the high repetition rate of the laser system in conjunction with an Acton SP2300i spectrometer. During the measurements, the pump beam is mechanically chopped and the utilized detecting unit is phase-locked to the chopping frequency, corresponding to 937 Hz when using the lock-in amplifier. In single shot measurement, the electronic shutter of the CCD has to be synchronized with the radio frequency timing Q-switch and cavity dumper of the amplifier, which is achieved using a binary counter to externally set the chopping frequency to $250/(64 \cdot 2) = 1.95$ kHz, allowing to average over approximately 50 spectra in pump on and pump off conditions. The difference between the two conditions delivers the transient absorption signal.

$$\frac{\Delta T}{T} = \frac{T_{\text{pump on}} - T_{\text{pump off}}}{T_{\text{pump off}}} \tag{2.8}$$

Data acquisition and control over the various system components is achieved by using a homemade LabVIEW based software.

[1] The spectral range can be expanded into the UV up to 320 nm by using Ca_2F crystals instead of sapphire

Understanding TA signals

TA spectroscopy is based on three interacting excitation fields[2] and creates a third order nonlinear polarization in the material, resulting in additional field components in the direction of the probe field [3].

$$\frac{\Delta T}{T}(\omega) \approx \frac{\omega L}{\varepsilon_0 nc} \mathrm{Im} \frac{P^3(\omega)}{E' P(\omega)} \tag{2.9}$$

The dominating dynamics, if coherent or incoherent, heavily depend on the time-scales of investigation. If the time-resolution of the experiment is comparable or shorter than the dephasing times of a material system, the full semiconductor Bloch equations (compare [6]) and/or a response theoretical framework have to be used to account for all nonlinear processes contributing to the signal, encompassing amongst others self phase modulation, coherent coupling, free induction decay, stimulated Raman scattering and two photon absorption [3, 7]. Given the time-resolution of the described TA setup, most of these effects only take place within the pulse overlap time, therefore, only the population terms are sufficient to describe the time evolution of the system. The resulting transient absorption signal in such a case can be simplified to [3]:

$$\frac{\Delta T}{T}(\omega, t) = -L \left[\sum (\sigma_{i,j} \Delta N_j) * f_p \right](t) \tag{2.10}$$

$\sigma_{i,j}$ is the cross section of the transition from state i to state j, ΔN_j describes the change in population and the last part represents the convolution with the pump pulse profile. The photo-induced change in transmission upon population redistribution can be either positive or negative and can be depicted considering a simplistic three level system, composed of ground S0, first excited S1 and a higher lying excited state S2 (see Fig. 2.2 (a)). Upon photoexcitation, population depletion of the ground state leads to reduced probe absorption and therefore a positive $\Delta T/T$ spectrally matching with the linear absorption band, designated as ground state bleach (GSB). Two more transitions are available from the first excited state S1, corresponding to stimulated emission (SE) back to the ground state, appearing at the spectral position of the photoluminescence, and photoinduced absorption (PIA) into the higher lying excited state S2, manifesting in a negative $\Delta T/T$ signal, since this transition is not available in the unexcited system. The above picture describes solely population effects, caused by the photo-induced non-equilibrium occupation of certain states and TA spectroscopy would simply monitor the temporal evolution of the different non-equilibrium populations.

TA signatures of lead halide perovskites

To understand the TA-response of semiconducting systems we also have to take into account many-body-interactions. They can manifest in a change in the energetic band structure (band-

[2] We count two interactions with the pump and a third one with the probe field

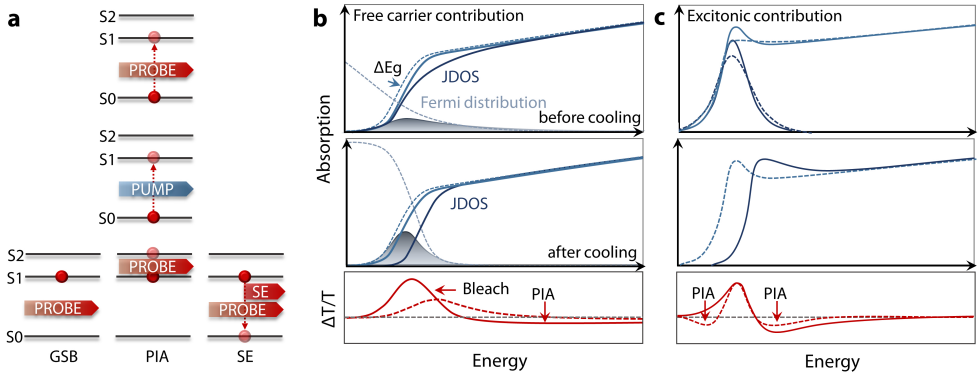

Figure 2.2
(a) Interpretation of transient absorption signals in a simplistic three level picture (see description in the main text). **(b)** Free carrier contribution to the TA signal in semiconductors: indicated are a shift in band edge ΔE_g due to bandgap renormalization and the carrier distributions before (top panel) and after cooling (bottom panel) with the respective changes in the joint density of states (JDOS). The resulting TA spectra are shown below as dotted (before cooling) and solid (after cooling) lines. (adapted from [8]). **(c)** Excitonic contribution to the TA signal. Top panel: line broadening and decrease in excitonic transition strength due to scattering and screening by the presence of free carriers, leading to a second derivative shape in the TA spectrum (dotted line). Band filling and corresponding shift in JDOS result in a characteristic PIA feature in the TA spectrum (solid line) [9, 10].

gap renormalization and change in the exciton binding energy) or broadening of energetic levels and are usually coupled to occupation effects by virtue of the distribution functions of the photo-excited carriers (Fermi-Dirac distribution). Furthermore, many-body effects strongly depend on the excitation density and on the nature of the primary photo-excitation, in particular if the prevalent species consists of excitons or free carriers. In the case of excitons, the dominant many-body contributions encompass energetic shifts, broadening and bleaching induced by Coulomb screening and phase-space filling, whereas for free carriers, effects like band-gap renormalization become important at high excitation densities. Band-gap renormalization originates from exchange interactions and can be understood in the following intuitive way. Attractive and repulsive Coulomb forces between charges would exactly cancel each other, if charge carriers would be randomly distributed. In reality, due to their fermionic nature, the Pauli principle forbids two carriers with equal spin to occupy the same unit cell. Thus, the exchange energy leads to a reduction of the repulsive Coulomb term and results in a lowering of the total energy, yielding a red-shift of the band gap. State-filling close to the band-edge reduces the absorption probability and leads to a modified joint density of optical states (JDOS) (see Fig. 2.2 (b)), thus gives rise to a transparency.[3] The latter becomes manifest

[3]Above certain excitation densities, the quasi Fermi levels of electrons and holes will move into the bands, the carrier population becomes degenerate, which constitutes the onset of population inversion and leads to a blue shift of the absorption edge, also referred to as "dynamic Burstein-Moss shift" [11] (a similar, but static effect can be observed in highly doped degenerate semiconductors). This process usually competes with band gap renormalization and surpasses the latter at high excitation densities. Population inversion can give rise to stimulated emission in direct bandgap semiconductors.

in a positive $\Delta T/T$ signal, usually referred to as photobleach (PB), which is first broad with an extended tail at higher energies due to the hot carrier distribution and subsequently sharpens and grows within picoseconds upon carrier cooling. In the absence of excitons, the TA spectrum will mainly consist of this PB feature and a broad PIA band on the blue side resulting from continuum band shifting caused by band-gap renormalization [8]. Although excitons in three dimensional lead halide perovskites have small binding energies at room temperature ($\sim 10-20$ meV), therefore most electron-hole pairs are ionized and free carriers determine the device relevant photophysics, excitonic effects still have to be taken into account to describe the linear and excited state electro-optical properties [8] especially in the high excitation density regime (compare Saha equation in the introduction and the respective discussion). Bound electron-hole pairs become the dominant contribution in lower dimensional systems .
Excitons are influenced by the presence of free carriers and depending on the carrier density, the corresponding spectral signatures can be quenched or completely suppressed, when their binding vanishes at the Mott density. Their contribution to the typical spectral shape in transient absorption measurements can be divided into three effects. A reduction in oscillator strength caused by phase-space filling, due to the Pauli exclusion principle and by Coulomb screening in the presence of free carriers. Screening decreases the exciton binding energy and therefore the overlap between electron and hole wavefunctions, leading to a decrease in transition strength. In addition, a reduction of the exciton binding energy leads to a blue shift of the exciton resonance. This blueshift is usually compensated by bandgap renormalization in three dimensional semiconductors, rendering the spectral position during photoexcitation unchanged but gains importance in lower dimensional systems [12]. The third effect is given by the exciton broadening, which increases due to a rise of the scattering rate, reducing the lifetime. Broadening and reduction of oscillator strength lead to a typical second derivative feature at early times. The blueshift of the absorption onset due to state-filling leads to a pronounced PIA feature at the higher energy side of the main bleach, which adds to the free carrier contribution (see Fig. 2.2 (c)) [9, 10, 13]. A multitude of different processes can contribute to the transient absorption signal resulting in heavily convoluted spectral features. Thus, their interpretation can be challenging and additional information gained from other spectroscopic techniques which offer higher spectral and/or time resolution is desirable.

2.3.2 Two dimensional coherent spectroscopy

Optical two-dimensional spectroscopy can spread congested spectra along a second dimension and measures the correlations between optical states [14], which allows to extract detailed spectroscopic information even in the presence of strong inhomogeneous broadening and was originally developed as optical analogue to multidimensional nuclear magnetic resonance (NMR). Experimentally, the spectral phase and amplitude of the transient four-wave-mixing signal generated by three successive incident pulses is measured by delaying the excitation pulses and using heterodyne detection. A so called box coherent anti-Stokes Raman scattering (BoxCARS) beam geometry for the excitation is usually applied to guide the nonlin-

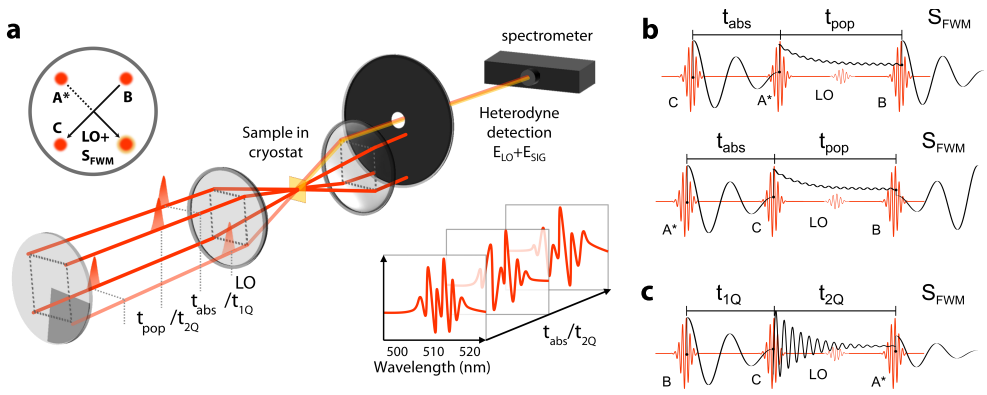

Figure 2.3
(a) Schematic representation of a transient four-wave mixing experiment. The geometric beam configuration and excitation scheme used to generate and detect the four-wave mixing signal (S_{FWM}) by interfering the signal with a local oscillator (LO) is shown. The beams co-propagate in a so-called BoxCARS beam geometry along the corners of a square and are focused onto the sample using a common lens, which defines the incident wavevectors $\vec{k}_A$, $\vec{k}_B$ and $\vec{k}_C$. The local oscillator, impinging from the fourth apex of the excitation geometry, co-propagates with the FWM signal and their spectral interferogram is recorded at every time step. Depending on the pulse order, different responses can be measured: **(b)** one-quantum measurements with non-rephasing ($\vec{k}_A$-$\vec{k}_B$+$\vec{k}_C$) and rephasing pulse sequence ($\vec{k}_B$-$\vec{k}_A$+$\vec{k}_C$). **(c)** Two-quantum pulse sequence. The pulses are shown in red, the induced polarization in black.

ear response of the sample in a dedicated direction as represented in Figure 2.3 (a). The three excitation beams of wavevectors $\vec{k}_A$, $\vec{k}_B$ and $\vec{k}_C$ crossing in the sample are incident from three corners of a box and result in a signal, radiating in the direction $\vec{k}_S = -\vec{k}_A + \vec{k}_B + \vec{k}_C$ of the fourth corner after the sample due to momentum conservation (phase-matching). The wavevector of beam A contributes negatively to the final vector sum and is referred to as conjugate beam, whereas the other two beams are non-conjugate. During the process, the first pulse creates a coherent superposition between ground and excited states and induces a polarization in the material. The second pulse arrives after a the evolution (absorption) time τ, interferes with the first pulse, completes the photon absorption process and generates a population grating at the interference maxima. The dynamic grating causes the third pulse arriving after a certain population time T to scatter into the phase-matched direction as four-wave-mixing signal. Microscopically the third pulse induces another coherence between ground and excited states, which emits in the corresponding direction [4]. The FWM signal (coherent emission signal) is overlapped collinearly with a well characterized reference pulse, the local oscillator (LO) to generate a spectral interferogram which is recorded for each time step by scanning the delays between the pulses. In addition to simultaneous determination of phase and amplitude, this heterodyne detection scheme also allows for phase cycling, to reduce undesired signal contribution due to scattering from the sample or setup components [15]. Fourier transform of the

[4]Pump probe spectroscopy can be considered as a special case of FWM. Here the first two pulses forming the pump arrive at the same time, corresponding to zero evolution time.

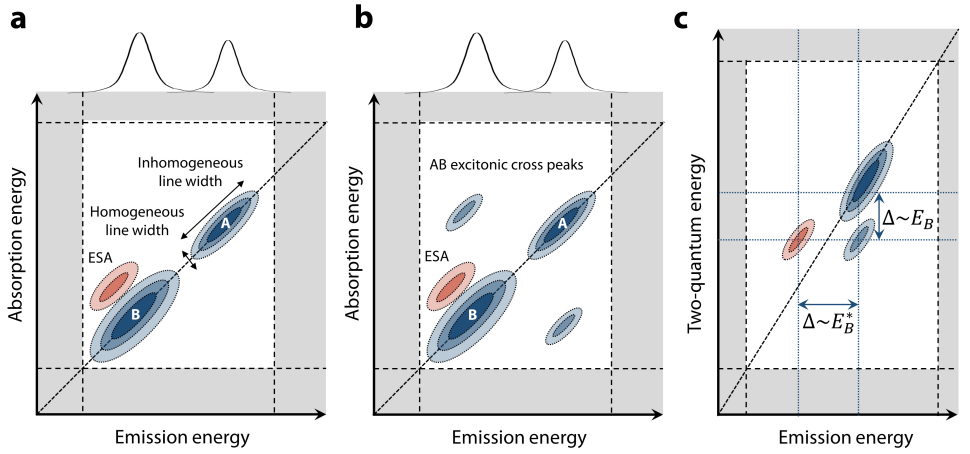

Figure 2.4
Illustration of one quantum total correlation maps in case of uncorrelated **(a)** and correlated **(b)** excited states.The spectra on top represent the linear absorption and are identical. Diagonal negative peaks correspond to the energies of the two states, the cross peaks appear if the states are coupled. Photoinduced absorption manifests as positive features, often spectrally overlapping with the negative cross-peaks. **(c)** Illustration of a two-quantum measurement of a biexciton, the corresponding peak is slightly below the diagonal, due to the bi-exciton binding energy, indicated by E_B.

time axis finally delivers the second frequency axis (absorption axis) to form a two dimensional frequency map which resembles an excitation spectrum.

By changing the time ordering of the excitation pulses, we can perform two different kind of experiments, one-quantum (1Q) and two-quantum (2Q) measurements (Fig. 2.3 (a), (b)). So called one-quantum total correlation experiments refer to pulse sequences ending with a non-conjugate beam. The designation originates from the particular kind of transitions probed during the measurement, encompassing the first and second ladder of excited states, namely transitions from the ground state, accessible through a single light-matter interaction and the corresponding excited-state absorption. Total correlation measurements are obtained by summing the real parts of rephasing (photon-echo) and non-rephasing spectra obtained by pulse sequences, starting with a conjugated or non-conjugated pulse respectively (Fig. 2.3 (b)). On the diagonal, one expects the spectral structure observed in linear absorption measurements, the autocorrelations of the optical transitions. Additionally, the spectra immediately reveal quantum correlations between different transitions due to coherences and population transfer, which become manifest in the presence of off-diagonal cross peaks as depicted in Figure 2.4 (b). Furthermore, contributions due to excited-state absorption (ESA) can be easily identified as spectral features of opposite sign [16]. Two-quantum non-rephasing experiments (Fig. 2.3 (c)) directly address the second excited-state manifold and constitute a sensitive tool to measure multi-exciton correlations. The changed pulse sequence in two-quantum measurements induces oscillations between the ground and two-quantum states and the frequency domain

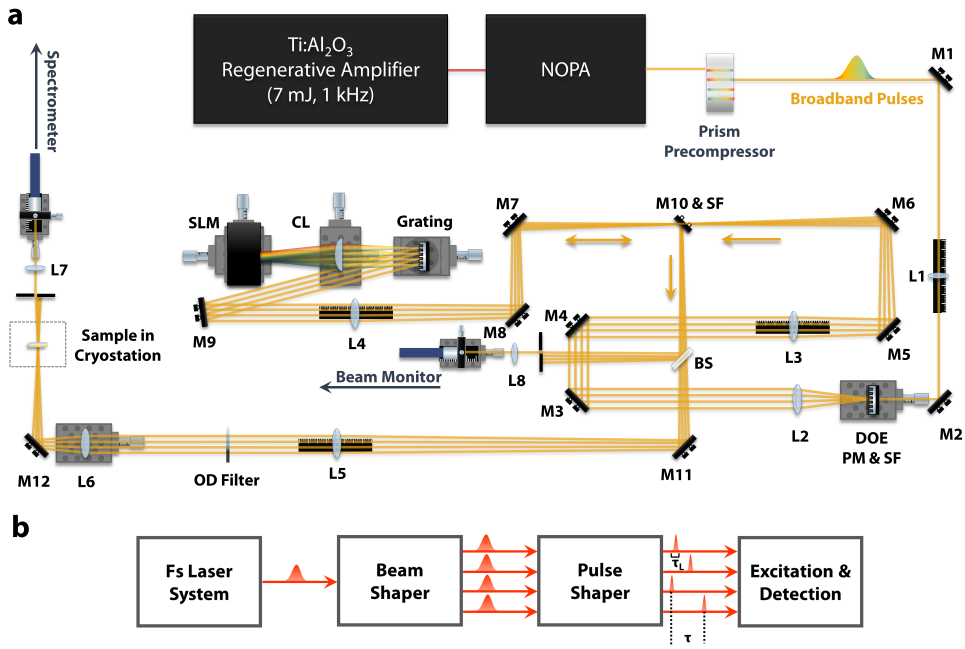

Figure 2.5
(**a**) Simplified optical layout of the multidimensional spectrometer. (**b**) The fundamental components of the setup: light source, beam shaper producing the geometrical BoxCARS arrangement of four co-propagating beams, spatiotemporal pulse shaper independently delaying and compressing the pulses and the detection unit, consisting of a fibercoupled spectrometer with attached CCD array.

two-quantum axis is obtained via Fourier transform along t_{2Q} (Fig. 2.3). Features in two quantum spectra selectively emerge from four-body states, including unbound but correlated two-exciton states along the diagonal and bound biexcitonic states below or above the diagonal by virtue of their binding energy (Fig. 2.4 (c)) [17].

Setup configuration

The setup used for multidimensional spectroscopy in this thesis is based on the coherent optical laser beam recombination technique (COLBERT), a spectrometer with superior phase stability, originally developed by Turner and Nelson [18]. Phase stability is achieved passively, since the spectrometer does not contain any moving parts (stages or wedges) and all beams pass through a common set of optics. The technique was implemented and extended by Félix Thouin at the University of Montréal, where the measurements were taken by the author in collaboration with the group of Professor Carlos Silva. In the following, the technical components and measurement principle will be briefly outlined, more details can be found in the references [18, 19]. A simplified sketch and summary of the crucial components is given by

Figure 2.5.

A 1 kHz Ti:sapphire regenerative amplifier system (Coherent Astrella) in conjunction with a home-built broadband two-pass nonlinear optical parametric amplifier (NOPA) generates broadband pulses with a spectral bandwidth of ~ 50 – 150 nm (depending on the central wavelength) [20]. The chirped pulses are pre-compressed, passing four times in a folded single-prism pulse compressor [21] and subsequently spatially filtered with a pinhole to obtain a clean Gaussian profile. A phase mask (PM) builds the diffractive optical element (DOE) and is designed in such way, that the four first order diffracted beams can be selected with a spatial filter (SF) to co-propagate in a rotated BoxCARS geometry. The fundamental component of the setup consists of a spatiotemporal pulse shaper, including a spatial light modulator (SLM), cylindrical lens (CL) and grating. It works in diffraction mode (to eliminate replica pulses [18]) and allows full control over the fields of each beam, including the temporal delays and phase. The four beams are dispersed by the grating, and collimated by a cylindrical lens to arrive as horizontal stripes on four vertical sections on the SLM (Fourier plane of CL). Each vertical array of pixels is programmed to form a sawtooth grating, which diffracts the frequency components impinging on the corresponding section. Temporal delay is introduced by linearly sweeping the phase across the frequency components of the diffracted light. The grating then recombines the diffracted modified frequency components to form temporally shaped pulses. The first diffractive order of the SLM is imaged on a pick-off mirror (M10, the other orders are blocked by a spatial filter) and redirected onto the sample. An additional spectrometer (beam monitor) is used to monitor the pump spectra during the acquisition to ensure spectral stability over the measurement time. The four beams are focused with a single 20 cm achromatic lens on the sample. The fourth beam, used as local oscillator for heterodyne detection is attenuated with a neutral density filter by three orders of magnitude, not to actively interact with the sample. The final signal is selected via optical iris and detected with a CCD camera attached to a fiber coupled Acton spectrometer. Prior to measurements, the system needs several calibration steps, including a greyscale to phase calibration of the SLM, a wavelength to pixel calibration and proper geometrical alignment of the cylindrical lens in the pulse shaper to prevent beam distortions. A detailed description is beyond the scope of this thesis and can be found in [18].

Short pulses are crucial to avoid artifacts due to non time-ordered interactions. Therefore, in addition to the prism based pre-compression, a 30 µm BBO crystal placed at the sample position serves for further temporal optimization and beam profile characterization. The second harmonic signal delivers the observable. All beams are one by one compressed, subsequently applying two iterations of chirp scan [22] and sufficient repetitions of the MIIPS algorithm [23] until any detectable group delay dispersion (GDD) disappears. The resulting temporal profile of one of the beams (generally the local oscillator) is subsequently characterized using collinear frequency gating (CFROG). The requisite pulse replica is generated by cosine modulation of the phase pattern from the previous compression step and any artifacts removed by two-dimensional Fourier transform [24, 25]. Finally, all other beams were cross-correlated with the local oscillator to ensure that their temporal pulse profiles are comparable or shorter

than the previously characterized pulse width. Typical obtained pulse widths for the experiments in this thesis are ~ 20 fs. Each excitation pulse carries around 15 nJ amounting to a total fluence of ~ 20μJ/cm². During the measurements, the sample is kept in a cold-finger closed cycle cryostat (Montana Instruments Cryostation) with the active layer in contact with the cold finger.

2.3.3 Excitation correlation photoluminescence (ECPL) spectroscopy

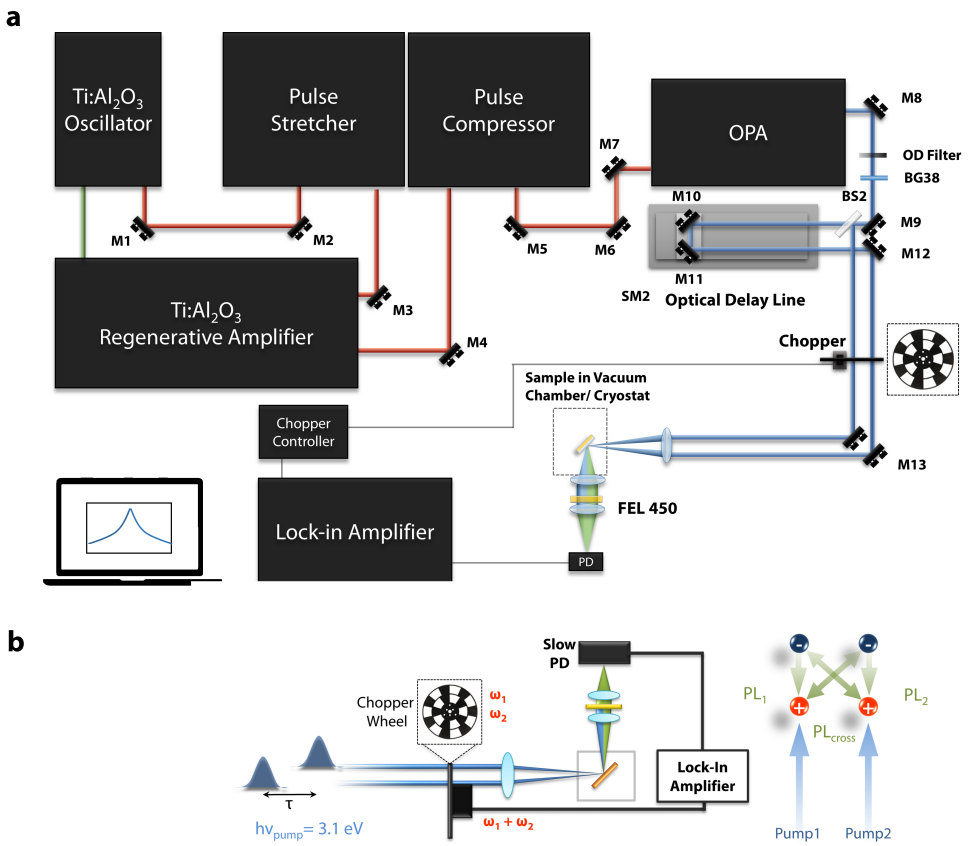

Figure 2.6
(a) Simplified optical layout of the ECPL-setup. **(b)** Illustration of measurement principle with the corresponding beam interactions (adapted from [26]).

ECPL spectroscopy was originally proposed in 1981 by von der Linde *et al.* [27] to track the nonlinear part of the photoluminescence from semiconductors. It corresponds to a variation of degenerate pump-probe with the important difference, that instead of monitoring the change

in transmission of a weaker probe pulse the time-integrated photoluminescence is measured as a function of time delay between two excitation pulses of equal power, size and energy. Given that the luminescence of the material is a nonlinear function of the excitation density due to population mixing, the resulting signal cannot be simply described as the sum of the two signals, generated when considering both excitation pulses separately. In practice heterodyne detection is used to isolate this nonlinear part of the signal by modulating the excitation beams at different frequencies and detecting at the sum-frequency.

Setup configuration

The laser system delivering the fundamental 800 nm pulses is identical to the light source described in the TA section. After the compressor the pulses are subsequently frequency doubled within the BBO crystal of the OPA, resulting in 400 nm pulses of ~ 100 fs length and and split using a thin 50:50 beam splitter to generate two optical pump lines, whereupon one contains a computer controlled optical delay stage to vary the delay between the two excitation pulses. By means of a mechanical chopper the two beams are modulated at different frequencies (381 and 272 Hz) and both focused onto the sample by the same 150 mm lens. A simplified layout of the setup is show in Figure 2.6.

The spectrally integrated photoluminescence of the sample is collected by a lens doublet and focused onto a slow silicon photodetector after filtering out the residual scattered pump light by using a long-pass optical filter (FEL 450 nm). The signal from the photodiode is sent simultaneously to a lock-in amplifier (Stanford Research Systems SR830) and an oscilloscope (Tektroniks TDS 2022C) to monitor ΔPL and PL at the same time. Referencing the used lock-in at the sum frequency (653 Hz) allows to extract the nonlinear fraction of the photoluminescence (see Fig. 2.6 b).

Principle of ECPL spectroscopy

Mathematically, the intensity of the collected photoluminescence when exciting the material with two pulses as a function of temporal delay τ can be expressed as [26, 28]:

$$\begin{aligned} PL(2I_{\text{pump}}, \tau) = & \int_0^\infty PL_1(I_{\text{pump}}, t)dt + \int_\tau^\infty PL_2(I_{\text{pump}}, t)dt + \\ & + \int_\tau^\infty PL_{\text{cross}}(2I_{\text{pump}}, t, t-\tau)dt \end{aligned} \tag{2.11}$$

The first two terms on the right side of Eq. 2.11 describe the photoluminescence as a result of excitation by each of the pump pulses separately, the third term emerges due to the nonlinear part of the photoluminescence by virtue of population mixing. We define the final ECPL signal

as the fraction of the nonlinear part over the total photoluminescence, given by:

$$ECPL(\tau = 0, I_{\text{pump}}) = \frac{PL(2I_{\text{pump}}) - 2PL_1(I_{\text{pump}})}{PL(2I_{\text{pump}})}. \tag{2.12}$$

The photoexcitation dynamics can be obtained by scanning the delay between the pulses with a time resolution of about ~ 150 fs. The advantage of the technique is its simplicity in terms of obligatory equipment, streak camera or photo counting system are not needed, additionally it provides high signal to noise ratio and time resolution, only limited by the pulse width. On the other side, measured time windows are limited by the used delay stage (in our case to ~ 2 ns) and interpretation of the obtained signals can be complex, therefore requiring a comprehensive photophysical model.

2.4 Sample preparation

The samples under investigation in this thesis were prepared by various partners, belonging to the same working group of the author and by collaborators at the IIT Genova and Nanyang Technological University of Singapore. The main contributions have to be acknowledged to Marina Gandini (3D perovskites), Quinten Akkerman (nanocrystals) and Daniele Cortecchia (2D perovskites). For the sake of completeness, the employed synthesis steps for the different systems will be described briefly [26, 29–32].

2.4.1 Three dimensional lead halide perovskites

$MAPbI_3$ (MA=methylammonium)

Synthesis of methylammonium iodide salt

The synthesis of the precursor solution follows a well-established procedure that was reported elsewhere [33]. Hydroiodic acid (57 wt% in water, obtained from Sigma-Aldrich) reacts with methylamine solution (33 wt% in ethanol, obtained from Sigma-Aldrich), leading to excess methylamine by adding ethanol. Subsequent drying with a rotary evaporator yields the white methylammonium iodide salt. Finally, the salt is washed in diethyl ether to purify it.

Thin film preparation

Samples are usually prepared in a controlled nitrogen atmosphere on glass microscope slides. Prior to deposition, the substrates are cleaned (two cycles of sonication in water, acetone and isopropanol (IPA) for 10 minutes respectively), followed by 10 minutes of oxygen plasma treatment. To obtain $CH_3NH_3PbI_3$ films, a two-step deposition method is employed. As first step, a hot (70°C) solution of PbI_2 in N,N-dimethylformamide (DMF) (462 mg/ml) is spin coated for 60 s at 2000 r.p.m, yielding a final layer thickness of ~ 300 nm, followed by an annealing step at

70°C for 30 min to form a thin PbI_2 film. In a second step, the cooled down PbI_2 coated substrates are dipped in CH_3NH_3I solution. By varying solution concentration and temperature different crystal sizes can be realized. To obtain $CH_3NH_3PbI_3$ films with crystal sizes around 1 µm, the substrates are left for 2 minutes in a solution with a concentration of 0.045M CH_3NH_3I in IPA at 70°C. For small crystallites (< 200 nm) the salt concentration is raised to 0.063M and the solution kept at room temperature. At the end, all samples are rinsed in anhydrous IPA to remove any excess unreacted CH_3NH_3I.

$MAPbBr_3$

Synthesis of methylammonium bromide salt

The salt is prepared according to a method from literature [34]. Hydrobromic acid (48 wt% in water, obtained from Sigma-Aldrich) and methylamine solution (33 wt% in ethanol, obtained from Sigma-Aldrich) are added to 100 ml ethanol and stirred at room temperature. Afterwards, the solvent is removed via rotary evaporation. The resulting crystals are washed in diethyl ether and subsequently recrystallized in ethanol.

Thin film preparation

$CH_3NH_3PbBr_3$ samples are deposited in a one-step process. Therefore, the CH_3NH_3Br salt and $PbBr_2$ are both dissolved in DMF (20 wt% concentration) and the solution spin-coated for 60 s at 3000 r.p.m on a cleaned glass substrate (see above). The final film is obtained after annealing the sample at 100 °C for approximately 15 minutes.

2.4.2 Two dimensional lead halide perovskites

$(EDBE)PbI_4$ (EDBE=2,2-(ethylenedioxy)bis(ethylammonium))

Synthesis of 2,2'-(ethylenedioxy)bis(ethylammonium) salt

Usually, 1 ml of 2,2'-2,2'-(ethylenedioxy)bis(ethylamine) is dissolved in ethanol (10 ml) and reacted with hydriodic acid HI (57% wt in water, distilled and stabilized, Sigma Aldrich) solution, which is added in drops to the stirred and cooled amine solution. After a reaction time of 4h, the solvent can be removed using a rotary evaporator, and several steps of washing in hot ethanol and precipitating in diethyl ether yield the white precursor salt. Finally, the salt is dried for 12 h at 60°C in a vacuum oven and stored in inert (N_2) atmosphere.

Thin film preparation

The precursor concentration determines the final film thickness. E.g., for a 0.5 M solution, 100 mg of $(EDBE)I_2$ (either synthesized or from Sigma Aldrich, 98%) and 115.2 mg of PbI_2 (99.995%, Alfa Aesar) are dissolved in 500 µL of dimethyl-sulfoxide DMSO (anhydrous, Sigma Aldrich). The solution is subsequently spincoated for 30s at 4000 r.p.m. and the resulting films

annealed for 30 min at 100°C on a hotplate.

Single crystals

(EDBE)PbI_4 single crystals are synthesized via vapor diffusion. Here, 33.5 mg of (EDBE)I_2 (obtained following the above procedure) and 26.5 mg of PbI_2 are dissolved in 3 ml of concentrated HI water solution. Leaving the solution for one week under diffusion of diethyl ether vapors results in the formation of mm sized yellow (EDBE)PbI_4 crystals.

$(NBT)_2PbI_4$ (NBT=n-butylammonium)

Thin film preparation

To obtain 0.25 M solution, 50.3 mg of (NBT)I (Dyesol) and 57.6 mg of PbI_2 are dissolved in 500 µL of N,N-Dimethylformamide, DMF (anhydrous, Sigma Aldrich). Analogous to (EDBE)PbI_4, the films are formed by spincoating the solution at 4000 r.p.m. for 30 s and subsequent annealing at 100°C for 30 min.

Single crystals

$(NBT)_2PbI_4$ crystals are obtained via slow cooling. Therefore, 100.52 mg of (NBT)I and 115.12 mg of PbI_2 are dissolved in hot concentrated HI water solution (1.2 ml at 100°C). After slowly cooling the solution in steps of 2°C per hour at room temperature, it is left for one week in a refrigerator at 2°C, promoting the growth of orange perovskite crystals on the bottom of the vial.

$(PEA)_2PbI_4$ (PEA=phenylethylammonium)

Thin film preparation

For a stoichiometric precursor solution (0.25 M) of $(PEA)_2PbI_4$, 62.3 mg (PEA)I (Dyesol) is mixed with 57.6 mg PbI_2 (99.99%, TCI) in 500 µL DMF (anhydrous, Sigma Aldrich). The solution is heated for 1 h at 100°C and spin-coated for 30s at 4000 r.p.m. on glass substrates, followed by an annealing step of 15 min at 100°C to form orange films.

Single crystals

For single crystals, 223.2 mg of PbO (Sigma Aldrich) is dissolved in 2 ml of aqueous HI solution with the addition of 170 µL of 50% aqueous H_3PO_2 (Sigma Aldrich). Separately, 92.4 µL of phenethylamine (Sigma Aldrich) are neutralized in 1 ml of HI (57% wt), yielding a white precipitate which re-dissolves upon heating. The latter solution is added to the PbO solution, and the mixture stirred for 10 min at 150°C on a hotplate. Subsequently, the solution is left to cool down at room temperature. 24 h later, the grown orange crystals are collected via filtration and dried under vacuum at 100°C.

References

[1] R. W. Boyd. *Nonlinear optics*. Academic press, 2003.

[2] H. A. Lorentz. *The Theory of Electrons and Its Applications to the Phenomena of Light and Radiant Heat: A Course of Lectures Delivered in Columbia University, New York, in March and April, 1906*. Vol. 29. Columbia University Press, 1909.

[3] G. Lanzani. *The photophysics behind photovoltaics and photonics*. John Wiley & Sons, 2012.

[4] A. R. Srimath Kandada. "Ultrafast Dynamics in Molecular Aggregates and Interfaces". PhD thesis. Politecnico di Milano, 2013.

[5] M. J. P. Alcocer. "Exploring Light Harvesting Systems via Broadband Transient Photoluminescence Spectroscopy". PhD thesis. Politecnico di Milano, 2014.

[6] H. Haug and S. W. Koch. *Quantum theory of the optical and electronic properties of semiconductors*. World Scientific, 1990.

[7] J. Shah. *Ultrafast spectroscopy of semiconductors and semiconductor nanostructures*. Vol. 115. Springer Science & Business Media, 2013.

[8] Y. Yang et al. "Observation of a hot-phonon bottleneck in lead-iodide perovskites". In: *Nature Photonics* 10.1 (2016), pp. 53–59.

[9] G. Grancini et al. "Role of microstructure in the electron–hole interaction of hybrid lead halide perovskites". In: *Nature photonics* 9.10 (2015), pp. 695–701.

[10] A. R. Srimath Kandada and A. Petrozza. "Photophysics of hybrid lead halide perovskites: the role of microstructure". In: *Accounts of chemical research* 49.3 (2016), pp. 536–544.

[11] J. Shah, R. Leheny, and C. Lin. "Dynamic Burstein shift in GaAs". In: *Solid State Communications* 18.8 (1976), pp. 1035–1037.

[12] X. Wu, M. T. Trinh, and X.-Y. Zhu. "Excitonic many-body interactions in two-dimensional lead iodide perovskite quantum wells". In: *The Journal of Physical Chemistry C* 119.26 (2015), pp. 14714–14721.

[13] A. R. S. Kandada et al. "Photophysics of Hybrid Perovskites". In: *Unconventional Thin Film Photovoltaics*. Royal Society of Chemistry, 2016, pp. 107–140.

[14] F. D. Fuller and J. P. Ogilvie. "Experimental implementations of two-dimensional Fourier transform electronic spectroscopy". In: *Annual review of physical chemistry* 66 (2015), pp. 667–690.

[15] J. C. Vaughan et al. "Coherently controlled ultrafast four-wave mixing spectroscopy". In: *The Journal of Physical Chemistry A* 111.23 (2007), pp. 4873–4883.

[16] P. Hamm and M. Zanni. *Concepts and methods of 2D infrared spectroscopy*. Cambridge University Press, 2011.

[17] D. B. Turner and K. A. Nelson. "Coherent measurements of high-order electronic correlations in quantum wells". In: *Nature* 466.7310 (2010), pp. 1089–1092.

[18] D. B. Turner et al. "Invited Article: The coherent optical laser beam recombination technique (COLBERT) spectrometer: Coherent multidimensional spectroscopy made easier". In: *Review of Scientific Instruments* 82.8 (2011), p. 081301.

[19] D. B. Turner. "Investigating Exciton Correlations Using Coherent Multidimensional Optical Spectroscopy". PhD thesis. Massachusetts Institute of Technology (MIT), 2010.

[20] G. Cerullo and S. De Silvestri. "Ultrafast optical parametric amplifiers". In: *Review of scientific instruments* 74.1 (2003), pp. 1–18.

[21] S. Akturk et al. "Extremely simple single-prism ultrashort-pulse compressor". In: *Optics Express* 14.21 (2006), pp. 10101–10108.

[22] V. Loriot, G. Gitzinger, and N. Forget. "Self-referenced characterization of femtosecond laser pulses by chirp scan". In: *Optics express* 21.21 (2013), pp. 24879–24893.

[23] B. Xu et al. "Quantitative investigation of the multiphoton intrapulse interference phase scan method for simultaneous phase measurement and compensation of femtosecond laser pulses". In: *JOSA B* 23.4 (2006), pp. 750–759.

[24] B. von Vacano, T. Buckup, and M. Motzkus. "Shaper-assisted collinear SPIDER: fast and simple broadband pulse compression in nonlinear microscopy". In: *JOSA B* 24.5 (2007), pp. 1091–1100.

[25] I. Amat-Roldán et al. "Ultrashort pulse characterisation with SHG collinear-FROG". In: *Optics express* 12.6 (2004), pp. 1169–1178.

[26] A. R. Srimath Kandada et al. "Nonlinear Carrier Interactions in Lead Halide Perovskites and the Role of Defects". In: *Journal of the American Chemical Society* 138.41 (2016), pp. 13604–13611.

[27] D. Von der Linde, J. Kuhl, and E. Rosengart. "Picosecond Correlation Effects in the hot luminescence of GaAs". In: *Journal of Luminescence* 24 (1981), pp. 675–678.

[28] M. Borgwardt et al. "Excitation correlation photoluminescence in the presence of Shockley-Read-Hall recombination". In: *Journal of Applied Physics* 117.21 (2015), p. 215702.

[29] S. Neutzner et al. "A dual-phase architecture for efficient amplified spontaneous emission in lead iodide perovskites". In: *Journal of Materials Chemistry C* 4.21 (2016), pp. 4630–4633.

[30] D. Cortecchia et al. "Broadband Emission in Two-Dimensional Hybrid Perovskites: The Role of Structural Deformation". In: *J. Am. Chem. Soc* 139.1 (2017), pp. 39–42.

[31] F. Thouin et al. "Stable biexcitons in two-dimensional metal-halide perovskites with strong dynamic lattice disorder". In: *arXiv preprint arXiv:1712.04733* (2017).

[32] Q. A. Akkerman et al. "Tuning the optical properties of cesium lead halide perovskite nanocrystals by anion exchange reactions". In: *Journal of the American Chemical Society* 137.32 (2015), pp. 10276–10281.

[33] H. Zhou et al. "Interface engineering of highly efficient perovskite solar cells". In: *Science* 345.6196 (2014), pp. 542–546.

[34] Z.-K. Tan et al. "Bright light-emitting diodes based on organometal halide perovskite". In: *Nature nanotechnology* 9.9 (2014), pp. 687–692.

Chapter 3

Nonlinearities in the Light Emission Characteristics of Lead Halide Perovskites

One of the most compelling aspects of lead halide perovskites, simple and easy processing from solution at room temperature, exposes them to a non-negligible amount of unintentional chemical and structural defects, consequently, obtaining a reliable and stable material proves to be a difficult task. Hence understanding the nature of defects and how they affect device operation remains a major challenge for incorporation of the semiconductor in market-scale optoelectronic products. In this chapter we study the recombination dynamics of photocarriers in three prototypical lead bromide perovskite systems by means of excitation correlation photoluminescence (ECPL) spectroscopy and quantitatively characterize their carrier trapping dynamics within a generalized Shockley-Read-Hall framework. This particular spectroscopic technique features superior sensitivity towards many-body interactions within the emission properties of a material and moreover allows to asses the energetics of defects. We demonstrate, that the predominant occurrence of shallow or deep defect states is correlated to the employed synthesis conditions, which provides guidelines for material engineering. We show that shallow defects, energetically located about 20 meV below the conduction band, can act as dopants in the semiconductor and enhance the photoluminescence quantum yield (PLQY), despite simultaneous trapping of carriers. Furthermore, high excitation densities reveal the formation of a new correlated carrier regime, suppressing nonradiative Auger effects. Finally, we demonstrate that colloidal $CsPbBr_3$-nanocrystals can be perceived as almost defect free system, suffering only from nonradiative Auger recombination at high excitation densities.[1]

[1]The content of this chapter is adapted with permission from Kandada and Neutzner *et al.*, "Nonlinear Carrier Interactions in Lead Halide Perovskites and the Role of Defects", *J. Am. Chem. Soc.*, 2016, 138, 13604–13611. Copyright (2016) American Chemical Society. [1]

3.1 Introduction

Hybrid lead halide perovskites have demonstrated exceptional properties for optoelectronic applications, comprising strong absorption associated with an excitonic transition close to the band edge, long carrier lifetimes [2–4] and tunability of the bandgap [5, 6] leading to remarkable photovoltaic (PV) performances with efficiencies, exceeding 22% [7].
Owing to efficient screening and therefore small exciton binding energies in the range of tens of meVs, the predominant population after photo-excitation in $MAPbX_3$ systems for excitation densities relevant for photovoltaic and light emitting applications (below 10^{17} cm^{-3}) is formed by ionized states [8, 9]. The principle of detailed balance [10] requires radiative recombination between electron and hole as necessary process equilibrating carrier generation, however, this recombination channel can be limited by non-radiative processes. When a defect state is energetically located within the semiconductor bandgap it can trap an electron or hole. Depending on the activation energy, which constitutes the energetic depth of the defect within the bandgap, the trapped carrier can be detrapped or recombine non-radiatively with its counterpart, leading to an excitation density dependent branching of the recombination pathways. Non-radiative recombination due to defects limits carrier lifetimes, photoluminescence quantum yields (PLQY) and subsequently device performances. Whereas well passivated $CsPbBr_3$ nanocrystals have been demonstrated to exhibit a PLQY as high as 90% [11, 12], polycrystalline films barely surpass 30% at low excitation densities (below 10^{17} cm^{-3}) [13]. At high densities, multi-particle Auger recombination constitutes another non-radiative loss channel for the carrier population [4, 14]. Understanding and quantifying the different limiting mechanisms is of paramount importance to optimize the material for device implementation.
Based on time-resolved photoluminescence spectroscopy (Tr-PL) the recombination dynamics of methylammonium lead halide perovskites have been characterized using a generalized Shockley-Read-Hall formalism, assuming energetically deep trap states rendering detrapping highly unlikely (compare equations 1.35). However, there had been theoretical [15–20] and experimental [21, 22] evidence that a substantial fraction of the possible defect configurations (encompassing various point, surface and linear defects) can exhibit low formation energies therefore forming shallow trap levels. Furthermore, it had been proposed that their selective appearance in the material is influenced by the specific precursor chemistry during fabrication [15, 23, 24] along with post fabrication conditions [25–27]. Shallow defects can dope the material and do not necessarily constitute nonradiative quenchers of the carrier population [28]. Thus the simplified recombination model widely used so far might not be sufficient to describe the actual photophysical scenario.
Electrical measurements to characterize defects in hybrid perovskites, are difficult to perform and decipher due to hysteresis effects and the low conductivity of polycrystalline films. Conventional PL techniques are not able to unambiguously identify the nature of traps without precast photophysical model. Transient PL spectroscopy gives information about diverse recombination rates, including the trapping rate but it cannot differentiate between particular kind of defects, excitonic effects and possible carrier doping, leading to variable assignment options within the numerical analysis[21]. Careful analysis of the intensity-dependent steady-

state PL behaviour can give pivotal information to select a suitable photophysical model, nevertheless, it is not commonly carried out in conjunction with time resolved techniques. Due to the complexity of possible interaction dynamics between carriers and various defect states, a method able to intrinsically differentiate between numerous nonradiative decay mechanisms is advantageous.

In this chapter, we use excitation correlation photoluminescence spectroscopy [29–33], a technique inherently sensitive to nonlinear carrier interactions which can provide special insight into the nonradiative loss channels. We investigate the dynamics of three exemplary lead bromide perovskite systems and study the influence of their fabrication conditions. Polycrystalline thin films of $MAPbBr_3$ on glass exhibit deep and shallow defects, the latter inducing unintentional doping in the material and we demonstrate their particular influence on the excitation density dependent recombination dynamics. Their respective predominance in the material is correlated with their synthesis route, in particular, a halogen rich environment promotes shallow defect formation over detrimental deep defects. In fact, $CsPbBr_3$ nanocrystals, growing as colloids with an excess of halogen exhibit predominantly radiative electron-hole recombination without signatures of intrinsic constraints of the material properties. Nevertheless, they are limited by nonradiative Auger recombination at higher excitation densities, when the average number of excitations per nanocrystal surpasses ~0.15.

3.2 Results and discussion

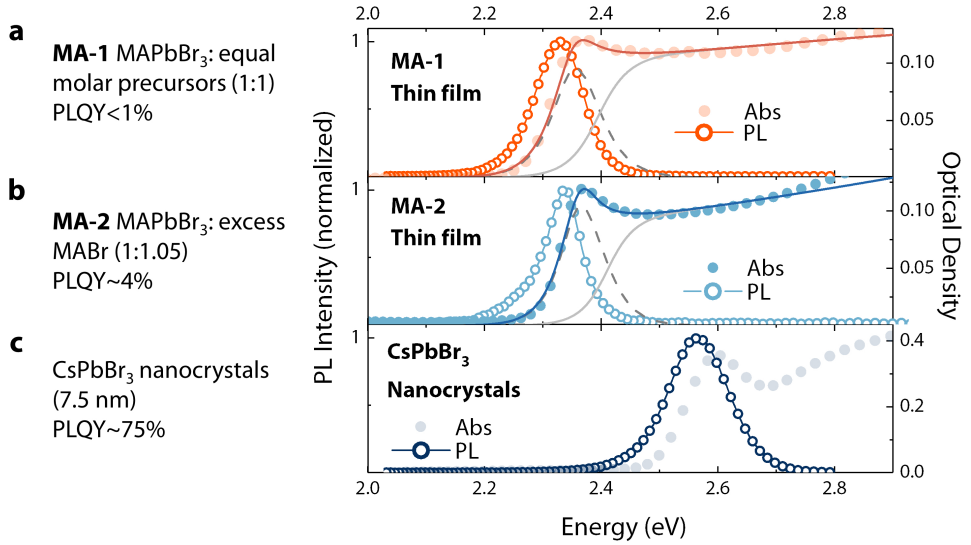

Figure 3.1
UV-vis absorption and photoluminescence spectra of (**a**) MA-1 and (**b**) MA-2 thin films on glass, made with different ratios of precursors and of (**c**) a colloidal suspension of $CsPbBr_3$ nanocrystals of ~7.5 nm size. Fits of the free carrier and excitonic absorption using Elliott's formula (compare equation 1.19) are plotted as continuous and dashed gray lines respectively (adapted from [1]).

3.2.1 Steady-state characterization

Figure 3.1 represents the UV-vis absorption and steady state PL spectra of the three investigated sample systems. The first two are $MAPbBr_3$ thin films prepared following two different fabrication protocols. MA-1 bases on an equimolar precursor ratio between PbBr and MABr (1:1) during synthesis and is deposited in a single step, whereas MA-2 is fabricated in the presence of excess MABr (1:1.05). As reported in Figure 3.1 (a) and (b), both thin films show similar optical characteristics, exhibiting an absorption onset at approximately 2.35 eV combined with an excitonic resonance at 2.37 eV. Modeling of the absorption lineshape in the framework of Elliott's theory (see introduction, eq. 1.19) yields similar exciton binding energies of 42 and 47 meV for MA-1 and MA-2, respectively. The third system in this study (Fig. 3.1 (c)) consists of a colloidal suspension of $CsPbBr_3$ cubic shaped nanocrystals of approximately 7 nm in size. The band-edge is blue-shifted in comparison to the two thin films by virtue of non-negligible quantum confinement. The MA-1 film shows a very low PLQY of about 1% at excitation densities around 10^{16} cm^{-3}, whereas MA-2 exhibits around 4% at comparable excitation densities (both measured under ambient conditions), in agreement with previous reports, demonstrat-

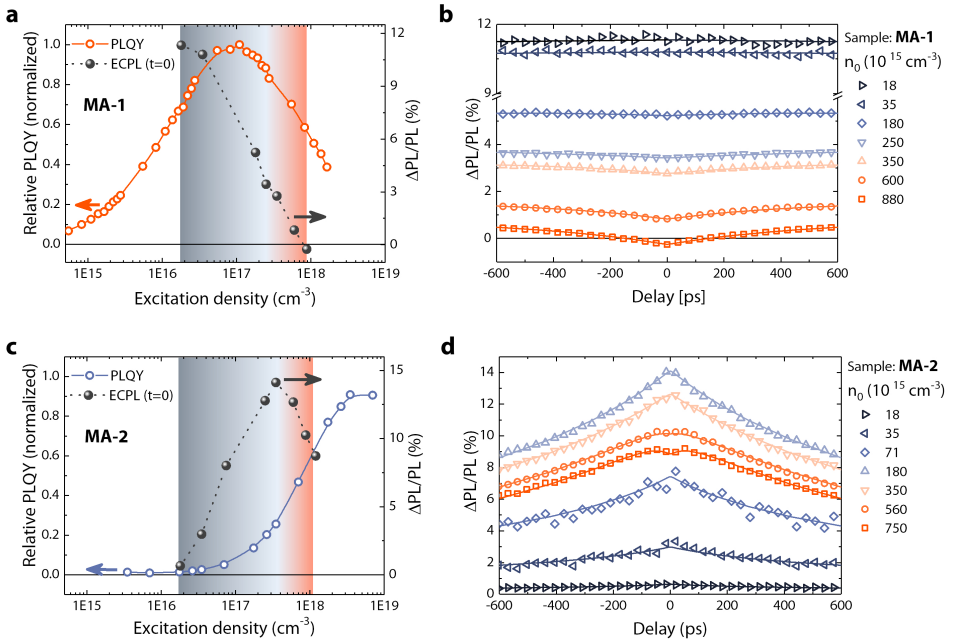

Figure 3.2
Relative PLQY and zero-delay ECPL signals plotted as function of excitation density for **(a)** MA-1 and **(c)** MA-2. Panel **(b)** MA-1 and **(d)** MA-2 show the full ECPL dynamics at different excitation densities. Symbols represent the experimental data, the solid lines are numerical fits according to the models explained in the main text (adapted from [1]).

ing that the presence of excess Br leads to films with higher PLQY although without further categorical rationalization [34]. $CsPbBr_3$ nanocrystals on the other hand reveal a PLQY of about 75%, thus constituting an efficient light emitting system. First, we perform ECPL experiments on the two $MAPbBr_3$ thin films, the corresponding measurement principle can be found in the methods chapter. If we consider an ideal scenario of pure radiative recombination, either geminate (eq. 1.34) or bimolecular (eq. 1.31), the steady-state photoluminescence will grow linearly with excitation density. According to equation 2.12, a linear dependence will give rise to zero ECPL signal. The case of density-dependent competing nonradiative processes leads to sublinear or superlinear behaviour of the steady-state PL as a function of light intensity and yields a non-vanishing ECPL signal. The commonly applied SRH formalism with deep traps (compare introduction section 1.3.3) results in a superlinear increase of PL intensity ($\propto I^{1.5}$). Such a scenario would yield a maximum positive ECPL signal of 30% at zero delay. In contrast, Auger-like processes lead to a sublinear steady state dependence of the PL ($\propto I^{0.6}$) thus the corresponding ECPL signature is negative. The above demonstration shows, that the technique allows to specifically select the contributions of the nonradiative loss channels from the overall relaxation dynamics and therefore gives higher precision than conventional measurement techniques.

3.2.2 MA-1 and MA-2: relative PLQY and ECPL

Figure 3.2 (a) and (c) present the relative PLQY (see methods chapter) as a function of excitation density for the two $MAPbBr_3$ systems respectively. As comparison, the specific tendency of the ECPL signal at time zero is shown for both thin films. Figure 3.2 (b) and (d) exhibit the corresponding dynamics for the different excitation densities. Their symmetry arises from the reciprocity of the two pulses. The MA-1 film shows a monotonic increase in relative PLQY, due to an excitation density dependent quenching of the nonradiative path resulting from trapping of the excited carrier population. If the excitation density rises above the available trap density, the free carrier population accessible for radiative recombination starts to increase, enhancing the PLQY. At large excitation densities (close to 10^{18} cm^{-3}) Auger recombination reduces the yield. The ECPL signal is positive and is measured to be around 11 % at excitation densities of 10^{16} cm^{-3} , not showing any ostensible decay within the experimental time window of 600 ps, due to recombination lifetimes in the order of nanoseconds. The positive sign indicates trap limited behaviour as discussed earlier. By increasing the excitation density, the bimolecular component increases as a consequence of trap filling, thus lowering the ECPL signal. When the excitation densities start to exceed $3x10^{17}$ cm^{-3}, another kinetic appears in the ECPL dynamics, and the zero-delay signal starts to become negative at the highest excitation density. This behaviour can be assigned to nonradiative Auger recombination and the respective dynamics directly deliver the Auger rate.
In the case of MA-2, the relative PLQY (Fig. 3.2 (c)) shows a similar trend to MA-1, suggesting trap limited recombination, even though the onset where the signal starts to increase is shifted by approximately two decades to higher excitation densities (the absolute PLQY is considerably higher in MA-2 than in MA-1). In contrast, the density evolution of the zero delay ECPL signal suggests a different and even contradicting scenario. The ECPL response presented in Figure 3.2 (c) and (d) remains close to zero at low excitation densities and based on our previous discussion could be interpreted as efficient radiative recombination in the bimolecular regime. Upon increasing the excitation density up to 10^{17} cm^{-3}, the ECPL signal rises to a maximum value of about 15% and exhibits in all traces a distinct dynamic with a decay time of about 500 ps. At higher excitation densities the signal decreases again and starts to develop a negative dip around time zero. To quantitatively analyze the density evolution of the ECPL traces we consider the following set of rate equation, including the possibility of carrier detrapping and schematically depicted in Figure 3.3 (b):

$$\frac{dn}{dt} = G - R - \gamma_t(N_t - n_t)n + \gamma_d n_t - \gamma_A n^2 p \tag{3.1}$$

$$\frac{dp}{dt} = G - R - \gamma_r n_t p - \gamma_A n^2 p \tag{3.2}$$

$$\frac{dn_t}{dt} = \gamma_t(N_t - n_t)n - \gamma_r n_t p - \gamma_d n_t. \tag{3.3}$$

Here, G is the generation rate due to light absorption, $R = B_{rad}np$ stands for the bimolecular recombination, γ_t represents the trapping rate under the presumption of predominant electron

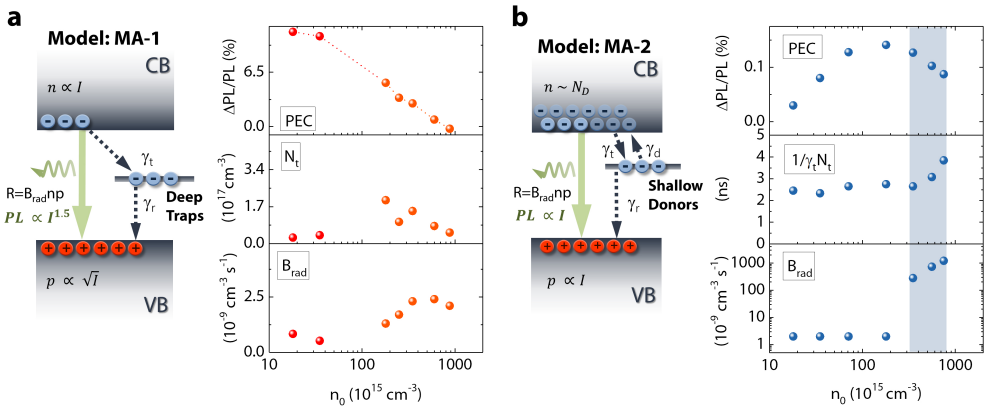

Figure 3.3
(a) Photophysical scenario for MA-1 assuming deep traps as primary recombination channel and corresponding fit parameters. **(b)** Employed model for MA-2, based on shallow donor levels, acting as recombination centers but doping the material and the fit parameters obtained from the model (adapted from [1]).

trapping, N_t is the total available trap density and γ_r and γ_d represent the recombination rate of a trapped electron with a hole and detrapping rate respectively. If electron or hole are trapped within energetically deep defects, the detrapping rate is negligible whereas in the case of shallow defects levels, this term must be taken into account. γ_A stands for the nonradiative Auger rate. To keep our model simple, we presume predominant electron traps, albeit the formalism can be easily extended to also include hole traps. In contrast to the common formalism in literature, which takes into account only the dynamical evolution of the excited carrier population employing a monomolecular trapping rate (compare eq. 1.28) we consider here coupled equations, including the electron, hole and trap densities without any anticipated presumption on the trapping mechanism.

By fitting the ECPL data of MA-1 assuming a SRH framework (see Fig. 3.3 (a)), we obtain a trap density of around 1×10^{17} cm^{-3}, $B_{rad} = 2 \times 10^{-9}$ cm^{3}s^{-1}, $\gamma_A = 1 \times 10^{-27}$ cm^{6}s^{-1}, $\gamma_t = 0.84 \times 10^{-9}$ cm^{3}s^{-1} and $\gamma_r = 0.19 \times 10^{-9}$ cm^{3}s^{-1} (the complete list of parameters can be found in the experimental section, table 3.1). In general, our experiments on MA-1 can be quantitatively described within a trap limited SRH based recombination model, as suggested in previous reports [21, 35].
If we use the same photophysical model to fit the ECPL data of MA-2, the resulting $B_{rad} = 2.2 \times 10^{-6}$ cm^{3}s^{-1} at low densities ($\sim 18 \times 10^{15}$) cm^{-3} is about 3 orders of magnitude higher than the parameter retrieved from MA-1, which would result in a PLQY of almost unity, obviously not being the case. Moreover, fitting the evolution of the ECPL signal as a function of excitation density would require an inversely proportional dependence of this coefficient (compare table 3.2). Physically, B_{rad} constitutes an intrinsic material property, which depends on bandgap and transition moments determined by the electronic band structure. Consequently, materials with identical optical signatures and similar chemical composition like MA-1 and MA-2

have to exhibit a comparable B_{rad} which does not depend on the excitation density and therefore a meaningful interpretation of the data demands for an adjustment of the photophysical model.
Zero ECPL signal suggests a practically linear behavior of the PL ($\propto B_{rad}np$) with excitation density, instead of the superlinear behaviour emerging from a SRH formalism. Such linear dependence despite carrier traps can result from shallow defect states, that apart from constituting nonradiative recombination centers, act as donors (or acceptors) doping the material when thermally ionized.
Doping modifies the charge neutrality condition according to $n + n_t = N_d + p$ (where n, p, n_t and N_d are the electron, hole, filled defect and doping densities respectively) and leads to a large background carrier density $n \simeq N_d$ without illumination. If we presume that shallow defects are n-doping the perovskite, p is proportional to the light intensity I and $n \simeq N_d$ for low excitation densities. This can be understood by recalling the above rate equations with the new charge neutrality condition (for the sake of simplicity we neglect the Auger term in the following discussion).

$$\frac{dn}{dt} = G - \gamma_t(N_d - n_t)n + \gamma_d(N_d + p - n) - Bnp \tag{3.4}$$

$$\frac{dp}{dt} = G - \gamma_r n_t p - Bnp \tag{3.5}$$

$$\frac{dn_t}{dt} = \gamma_t(n - p)n - \gamma_d(N_d + p - n) - \gamma_r n_t p \tag{3.6}$$

We presume $G \propto I$ since spontaneous carrier generation for radiative and non-radiative processes can be neglected already at low light intensity. Also, we consider the non-degenerate case, $n < n_{th}$ with $n_{th} = 2(m_e k_B T/(2\pi\hbar^2))^{3/2}$ representing the thermal density of electrons which results to $\sim 3 \times 10^{18}$ cm^{-3} at room temperature. Detrapping, expressed by $\gamma_d n_t$ constitutes a thermally mediated process. Therefore, the principle of detailed balance demands $\gamma_d = \gamma_t n_{th} e^{-\Delta E_d/(k_B T)}$ at thermal equilibrium, where ΔE_d represents the energy of the defect with respect to the electronic bands or equivalently, the defect ionization energy and T the temperature. For shallow defects, $\Delta E_d/(k_B T)$ is small and without illumination we have $p \ll n$. When the absolute number of trap states is much lower than the thermal electron density ($N_d \ll n_{th}$), all defects become fully ionized and without illumination we have $n \sim N_d$ and $n_t \sim n(N_d/n_{th})e^{\Delta E_d/(k_B T)} \ll n$. Further, we presume that the recombination processes at low excitation densities are dominated by hole-trap recombination, relevant for a low quantum yield. Finally, under illumination we obtain $n_t \sim \alpha n - I/\gamma_d$ with $\alpha = (N_d/n_{th}e^{\Delta E_d/(k_B T)}) \ll 1$ and $n \sim N_d + I/(\gamma_r \alpha N_d)$ as well as $p \sim I/(\gamma_r \alpha N_d)$. Thus, the PL is linear with light intensity and the ECPL response becomes negligibly small. With increasing excitation density, the density of photogenerated electrons reaches the magnitude of background doping density and starts to take part in the radiative process but also competes with carrier trapping. Therefore, $n, p \sim I/(\gamma_r N_d)$ and the ECPL response shows an almost linear trend with light intensity until an excitation density of $\sim 10^{17}$ cm^{-3}. Slope and onset are determined by the doping concentration. It is important to mention, that doping due to shallow traps can alleviate nonradiative

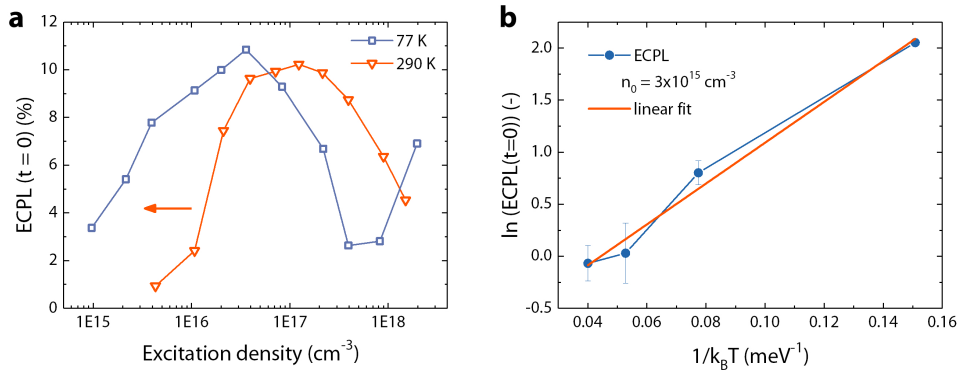

Figure 3.4
(a) Intensity dependence of zero-delay ECPL signal of MA-2 at room temperature and 77 K. **(b)** Logarithmic plot of zero-delay ECPL signal against $1/k_BT$ where k_B is the Boltzmann constant and T the temperature. The excitation density was fixed at 3×10^{15} cm^{-3} (adapted from [1]).

losses and explain the elevated PLQY observed in MA-2 in comparison to MA-1.

With the set of equations 3.3, considering the modified charge neutrality condition due to doping and significant detrapping we can quantitatively analyze the ECPL dynamics of MA-2. The observed dynamics here can be assigned to trapping by the shallow defect states on subnanosecond timescales. We extract a donor density of about 2×10^{18} cm^{-3} and a trapping rate $\gamma_t = 3 \times 10^{-8}$cm^{3}s^{-1}. Both are significantly higher than in MA-1, leading to the observed shift of the relative PLQY in MA-2 to higher excitation densities. Note, that the resulting value of B_{rad} corresponds to the previously obtained B_{rad} of MA-1, as expected for an intrinsic material property. The complete list of fitting parameters can be found in the experimental section in Table 3.3 and partly in Figure 3.3 (b).

3.2.3 MA-2: temperature dependence and defect energies

As we discussed before, the ionization of donor or acceptor states, leading to doping of a material, is a thermally activated process and the doping density is proportional to $e^{\Delta E_d/k_BT}$. Consequently, by reducing the temperature one would expect a reduction of the doped carrier concentration and, since the ECPL signal depends on the ratio between excitation density and background doping, a concomitant rise of the ECPL response. Figure 3.4 (a) shows the time zero ECPL signal as a function of excitation density for 290 K and 77 K. If we compare the signal at fixed excitation density (3×10^{15} cm^{-3}) we see the expected increase from 0.8% at 290 K to 8% at low temperatures and a shift of the whole ECPL trend to lower excitation densities at 77 K, in good agreement with our above presumption. The inverse proportionality between doping concentration and ECPL response can be used to quantify the ionization energy. Figure 3.4 (b) shows the linear relationship between $1/k_BT$ and $\ln(ECPL)$ at a fixed excitation

density of 3×10^{15} cm^{-3}. The slope here is given by the ionization energy ΔE_d which results equal to 19 ± 1.7 meV as derived from the data fit, underlining our presumption of shallow donor states in the material. Interestingly, Cho *et al.* [34] demonstrated that excess MABr during the synthesis of $MAPbBr_3$ can reduce the semiconductor work function.
Current theoretical studies show that most of the native point defects in lead halide perovskites, namely vacancies, interstitials and anti-site occupations have low formation energies and thus form shallow defect levels [17, 36–38]. They presume that due to the large formation energies of deep trap levels, their role in carrier recombination processes should be negligible, which is in agreement with our experiments on MA-2, where shallow defects form the main carrier traps. However, the formation of deep defects in "halogen-poor" conditions due to halide vacancies had also been suggested [16, 39] and shown for $MAPbBr_3$ [15], fully in agreement with our observations on MA-1, which is more susceptible to halide vacancies than MA-2. Despite still needing independent experiments to identify the chemical nature of defect states, ECPL allows to measure their energetics and to identify if shallow or deep levels form the predominant carrier traps. Furthermore, ECPL delivers a quantitative description of carrier dynamics in lead halide perovskites.

3.2.4 MA-2: high excitation density regime

So far, we did not discuss the behaviour of the ECPL signal of MA-2 above excitation densities of 10^{17} cm^{-3}. From the retrieved bimolecular recombination coefficient in Figure 3.3 (b) we see that our rate equation model breaks down when trying to account for the decrease in ECPL signal at higher excitation densities. A constant B_{rad} would result in a growing ECPL signal above the observed maximum of 15%. Including Auger recombination to counteract this trend would be accompanied by an abrupt decrease in PLQY, which is not observed.
The high excitation density regime in MA-2 could be interpreted in terms of an increase in carrier correlations, due to renormalization of the carrier interaction screening. The possible consequence could be the formation of a strongly correlated electron-hole plasma or the built-up of an exciton population. According to the Saha equation, the probability of the latter increases at high excitation densities (compare introduction). The excess energy for coalescence of carriers into an exciton needs to be released to the lattice. Considering the binding energies in this material, which are 3-5 times higher than the available LO phonon energies, the process would require the less probable emission of multiple phonons. Nevertheless, e-h plasma screening leads to a reduction in exciton binding energy with carrier density. A simple guess of the corresponding bandgap normalization [40] delivers ~ 60 meV at 3×10^{17} cm^{-3}, and ~ 100 meV at 10^{18} cm^{-3}, following a square root scaling with charge carrier density. Hence, in the density regime of the anomalous ECPL response, exciton formation would solely require emission of one single LO phonon and is therefore more probable than other multiphonon phenomena. This interpretation is supported by the fact, that at slightly higher excitation densities Mott transition takes place, leading to a complete dissociation of excitons but still preserving geminate recombination. Note that our explanation is only qualitative,

since the carrier population quickly decreases in time which results in a superposition of different regimes and interacting processes like Mott transition and exciton formation. Albeit we are not able to distinguish these complex dynamics with our simple model (eq. 3.3), we can apprehend the bottom line of carrier interactions in different regimes.[2]

3.2.5 $CsPbBr_3$: relative PLQY and ECPL

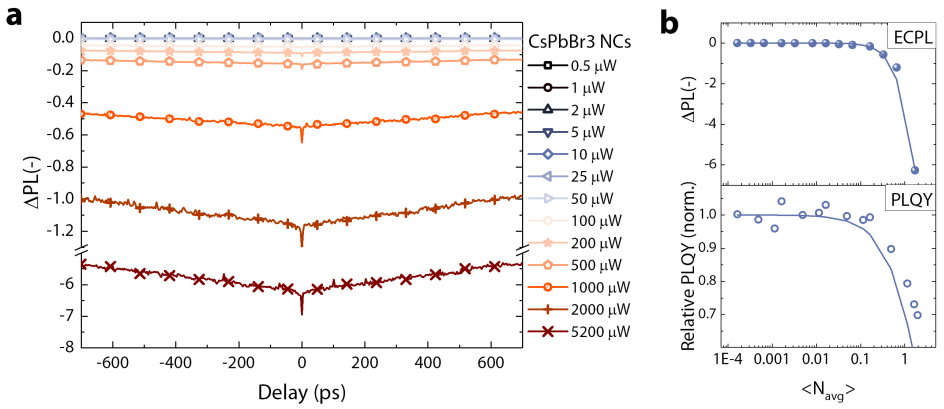

Figure 3.5
(a) ECPL dynamics of colloidal $CsPbBr_3$ nanocrystals as function of excitation density. **(b)** Top panel: ECPL, bottom panel: PLQY. Plotted over the average number of excitations per nanocrystal. Fits according to the theoretical estimates (see main text) are indicated by lines (adapted from [1]).

Finally we will discuss our third example system, the colloidal suspension of $CsPbBr_3$ nanocrystals (NCs). A PLQY of 75% already at low excitation densities [11, 41] and monoexponential recombination dynamics with a lifetime around 4 ns suggest excitonic emission [41] and indicate a negligible role of defects in the emission dynamics. We will use this perovskite system as control sample to validate our methodology in assessing different carrier trapping scenarios.[3] The measured crystals have an average size of 6.7 ± 1 nm. Figure 3.5 shows the ECPL dynamics for different excitation densities. At low densities, the ECPL signal is practically zero, corroborating the excitonic origin of the PL. With increasing pump intensities, the signal becomes negative but without changing the kinetics. For nanocrystals and quantum dots it is more intuitive to give the average number of excitations per crystal instead of the excitation density. We can make an estimate assuming that the bulk absorptivity α (in cm^{-1}) at 3.1 eV is comparable to the absorptivity of NCs, which is evaluated from thin $CsPbBr_3$ films to be $\sim 10^4$ cm^{-1}. Hence, the average number of carriers per crystal can be calculated according to $\langle N \rangle = \sigma \varphi_{photon}$, with

[2] The reason for not seeing the geminate regime in MA-1, might be related to an intrinsically lower deep trap density and reduced Auger scattering, leading to a higher carrier population available for radiative recombination.
[3] Thin films of $CsPbBr_3$ exhibit similar characteristics to the MA-2 sample, hence, we do not add additional variability.

$\sigma = \alpha V$ (V is the NC volume) being the absorption cross section and φ_{photon} denoting the photon flux. The calculated absorption cross section of 3×10^{-15} cm^2 agrees well with the estimates of Makarov *et al.* [42]. As depicted in Figure 3.5 (b), the zero time ECPL response starts to drop significantly when $\langle N \rangle > 0.15$, with a concomitant decrease in PLQY, suggesting Auger recombination of the excited state population, which relaxes the population per crystal as soon as the photoexcitations per particle start to surpass one. Exceeding a certain excitation intensity, the PL will start to saturate after the first pulse and only one photon will be emitted, regardless of the injected density. Thus, the PL decay exhibits the intrinsic exciton dynamics, and leads to monoexponential ECPL traces, independent of the pump intensity. We can analytically reproduce the behaviour presented in Figure 3.5 (b) by calculating the probability (p_m) of finding m excitons in a nanocrystal which can be expressed by a Poisson distribution $p_m = \frac{\langle N \rangle^m}{m!} e^{-\langle N \rangle}$. After Auger recombination, each excited nanocrystal is left with one exciton only for radiative recombination. In this case, the PL is proportional to $(p_1 + p_2 + \ldots + p_N) = 1 - p_0 = 1 - e^{\langle N \rangle}$ [43]. Consequently, we can estimate PLQY and ECLPL as $\propto \frac{1-e^{-\langle N \rangle}}{\langle N \rangle}$ and $\propto (1 - e^{-2\langle N \rangle}) - 2(1 - e^{-\langle N \rangle})$ respectively. The corresponding plots are indicated in Figure 3.5 (b) and nicely reproduce the experimental trends. Here we point out, that Auger recombination occurs before the gain onset, and subsequently forms the main limiting mechanism for lasing applications, as has been currently demonstrated by Makarov *et al.* [42]. At the same time, $CsPbBr_3$ nanocrystals form a clean material system with little restricting trapping processes.[4]

[4]The PLQY is about 75% which indicates, that there are non-radiative loss channels, probably due to insufficient passivation or bulk traps of some crystals which render the affected crystal dark. In the calculation above, we rescaled $\langle N \rangle$ correspondingly.

3.3 Experimental

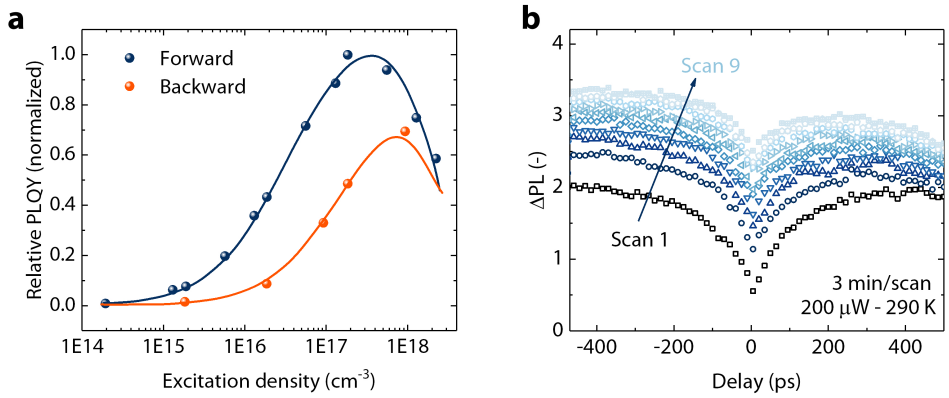

Figure 3.6
Instabilities of MA-1. **(a)** Relative PLQY with forward (lowest to highest intensity) and backward scans. **(b)** Successive ECPL scans show a growth with each scan till the sample starts to stabilize around 10 scans. Each scan took about 3 min. To minimize the instabilities during the main measurements, the sample was kept under constant illumination before starting the experiment (adapted from [1]).

Sample preparation and treatment: $MAPbBr_3$ thin films with equal precursor ratio (MA-1) were prepared according to the procedure described in the methods chapter.
$MAPbBr_3$ thin films with inorganic $PbBr_2$ to organic CH_3NH_3Br molar precursor ratio of 1:1.05 (MA-2) were prepared from solution in dimethyl sulfoxide (40 wt. %), following the recipe for nanocrystal pinning by Cho *et al.* [34]. The substrate was spun for 7s at 500 r.p.m. and 90 s at 3000 r.p.m. and the perovskite solution dropped after the first acceleration onto the substrate. Nanocrystal pinning was initiated with chlorobenzene after 60 s and the sample subsequently annealed for 10 min at 90°C. Prior to exposure to ambient conditions the sample were covered by poly(methyl methacrylate) (PMMA). The $MAPbBr_3$ thin films for this work were synthesized and prepared by Marina Gandini.
$CsPbBr_3$ nanocrystals were prepared as reported by Akkerman *et al.* [11].

ECPL measurements and relative PLQY: all measurements were carried out using the setup configurations described in the methods chapter.

All samples except the nanocrystal solutions were measured in running vacuum to prevent sample degradation due to the presence of oxygen and water during the measurements. Before taking the actual data, all samples were kept under constant illumination at higher light intensity to reduce PL instabilities, apparent in the hysteretic behaviour of the PLQY (Fig. 3.6 (a)) and a slow increase of the ECPL in time (Fig. 3.6 (b)). The available trap density increases on very slow timescales, possibly by photo induced formation of deep-trap states as proposed by Agiorgousis *et al.* [16]. As a matter of fact, a good theoretical fit of the PLQY as function of excitation density can be obtained by a consistent variation of trap density.

The following tables contain all relevant fit parameters for the employed models described in the main text. We have to highlight, that a global fit of the data over all excitation densities is not possible to perform. Partly, this can be attributed to errors when estimating the excitation density and other minor experimental errors but mainly to the effect of the above mentioned photo-instabilities. The measurements on MA-1 have been performed by starting from medium densities, subsequently moving to lower ones and taking the high density measurements at the end. Therefore, we have to expect an increase in trap density, since the sample was exposed to continuous illumination during the intensity sweep, which is reflected by the trends summarized in Table 3.1. Note that a reciprocal correlation seems to exist between B_{rad} and the trap density, which might suggest that filled traps act as carrier scattering centers, reducing the effective mean free path and eventually carrier-carrier interactions. Table 3.2 summarizes

MA-1: ECPL fit parameters: deep traps

n_0 (10^{15}cm^{-3})	B_{rad} (10^{-9}cm^{3}s^{-1})	γ_A (10^{-27}cm^{6}s^{-1})	N_t (10^{17}cm^{-3})	χ^2 red.
18	0.83 ± 0.03	7.2 ± 0.1	0.28 ± 0.01	
35	0.52 ± 0.01	3.3	0.39 ± 0.01	0.6
180	1.3 ± 0.1	1.3	2.0 ± 0.01	0.3
250	1.7 ± 0.01	0.43	1.0 ± 0.01	0.6
350	2.3 ± 0.01	0.36	1.5 ± 0.01	1.5
600	2.4 ± 0.01	0.13	0.81 ± 0.01	4.8
880	2.1 ± 0.01	0.064	0.51 ± 0.01	2.2

Table 3.1
Obtained fit parameters for the model employed for MA-1, assuming deep neutral traps as main loss channel at low excitation densities. Note, that trapping rate and recombination coefficient for the trapped electron with the hole are fixed at $\gamma_t = 0.84 \times 10^{-9}$cm^{-3}s^{-1} and $\gamma_r = 0.19 \times 10^{-9}$cm^{-3}s^{-1} respectively. All parameters vary slightly due to the sensitivity of the fits to any small offset.

the parameters from fitting the experimental data of MA-2 within a SRH framework.

MA-2: ECPL fit parameters: deep traps

n_0 (10^{15}cm^{-3})	B_{rad} (10^{-9}cm^{3}s^{-1})	γ_A (10^{-27}cm^{6}s^{-1})	N_t (10^{17}cm^{-3})	χ^2 red.
7	2200	0.1	0.62	< 1
18	480	0.1	2.2	< 1
35	170	0.1	5.5	< 1
71	57	0.1	7.8	< 1
180	22	< 0.1	8.4	< 1
350	14	0.65	8.6	< 1
560	12	1.4	11	< 1
750	12	1.2	12	< 1

Table 3.2
Obtained fit parameters employing the deep trap model for MA-2.

Table 3.3 lists all parameters obtained by fitting MA-2 with the modified model, considering shallow donor levels.

MA-2: ECPL fit parameters: shallow traps				
$n_0\,(10^{15}\mathrm{cm}^{-3})$	$B_{rad}\,(10^{-9}\mathrm{cm}^3\mathrm{s}^{-1})$	$\gamma_t\,(10^{-9}\mathrm{cm}^3\mathrm{s}^{-1})$	$\gamma_A\,(10^{-27}\mathrm{cm}^6\mathrm{s}^{-1})$	$N_t\,(10^{17}\mathrm{cm}^{-3})$.
7	2	0.17	8	24
18	2	0.24	8	17
35	2	0.39	8	11
71	2	0.29	8	13
180	2	0.13	8	28
350	280	0.13	130	29
560	730	0.13	210	25
750	1200	0.13	300	20

Table 3.3
Obtained fit parameters of MA-2 employing the modified model accounting for shallow donors. We presume $\gamma_d = 0.9\gamma_t N_t$. χ^2 red. remained < 3 for all fits.

3.4 Conclusions

In this chapter we use ECPL spectroscopy, to extract the nonlinear part of carrier recombination processes and we address the influence of defects and unintentional doping on the charge carrier dynamics of three exemplary lead bromide perovskite systems. Polycrystalline thin films of $MAPbBr_3$ prepared using equimolar precursor ratios exhibit predominantly deep trap mediated SRH-like recombination characteristics, whereas films prepared with excess MABr show clear signatures of shallow defects. We could retrieve the energetics of these defect states, which are located around 20 meV below the conduction band. At finite temperatures, they can be easily ionized leading to doping of the material and partly mitigating the effect of non-radiative recombination of the excited carrier population. Our results give evidence for the correlations between the energetics of defect states (in particular, deep versus shallow) and the synthesis conditions during the preparation of the thin film. Further and more detailed studies are needed to unambiguously identify the chemical nature of defect states, but our study provides refined photophysical models of the material, which allows to retrieve crucial photophysical parameters for material engineering. In addition, we demonstrate the existence of a correlated carrier regime at high excitation densities where geminate recombination dominates the carrier dynamics as long as detrimental non-radiative losses are alleviated. This regime can form due to screening at high excitation densities, causing renormalization of the band gap and competing and somehow limiting Auger recombination.[5] In the end, we demonstrate that well passivated colloidal $CsPbBr_3$ nanocrystals can constitute a practically defect-free semiconducting system, even though they still suffer from Auger recombination at high excitation densities.

[5]The existence of a second exciton regime had been recently confirmed by Sarritzu *et al.* [44].

References

[1] A. R. Srimath Kandada et al. "Nonlinear Carrier Interactions in Lead Halide Perovskites and the Role of Defects". In: *Journal of the American Chemical Society* 138.41 (2016), pp. 13604–13611.

[2] C. Wehrenfennig et al. "High charge carrier mobilities and lifetimes in organolead trihalide perovskites". In: *Advanced materials* 26.10 (2014), pp. 1584–1589.

[3] S. D. Stranks et al. "Electron-hole diffusion lengths exceeding 1 micrometer in an organo-metal trihalide perovskite absorber". In: *Science* 342.6156 (2013), pp. 341–344.

[4] V. D'Innocenzo et al. "Tuning the light emission properties by band gap engineering in hybrid lead halide perovskite". In: *Journal of the American Chemical Society* 136.51 (2014), pp. 17730–17733.

[5] E. T. Hoke et al. "Reversible photo-induced trap formation in mixed-halide hybrid perovskites for photovoltaics". In: *Chemical Science* 6.1 (2015), pp. 613–617.

[6] S. Pathak et al. "Perovskite crystals for tunable white light emission". In: *Chemistry of Materials* 27.23 (2015), pp. 8066–8075.

[7] N. C. for Photovoltaics (NCPV). *NREL efficiency chart*. 2018. URL: `https://www.nrel.gov/pv/assets/images/efficiency-chart.png` (visited on 01/13/2018).

[8] M. Saba et al. "Excited state properties of hybrid perovskites". In: *Accounts of chemical research* 49.1 (2015), pp. 166–173.

[9] V. D'Innocenzo et al. "Excitons versus free charges in organo-lead tri-halide perovskites". In: *Nature communications* 5 (2014), p. 3586.

[10] W. Shockley and H. J. Queisser. "Detailed balance limit of efficiency of p-n junction solar cells". In: *Journal of applied physics* 32.3 (1961), pp. 510–519.

[11] Q. A. Akkerman et al. "Tuning the optical properties of cesium lead halide perovskite nanocrystals by anion exchange reactions". In: *Journal of the American Chemical Society* 137.32 (2015), pp. 10276–10281.

[12] S. Yakunin et al. "Low-threshold amplified spontaneous emission and lasing from colloidal nanocrystals of caesium lead halide perovskites". In: *Nature communications* 6 (2015), p. 8056.

[13] F. Deschler et al. "High photoluminescence efficiency and optically pumped lasing in solution-processed mixed halide perovskite semiconductors". In: *The journal of physical chemistry letters* 5.8 (2014), pp. 1421–1426.

[14] R. L. Milot et al. "Temperature-Dependent Charge-Carrier Dynamics in $CH_3NH_3PbI_3$ Perovskite Thin Films". In: *Advanced Functional Materials* 25.39 (2015), pp. 6218–6227.

[15] A. Buin et al. "Halide-dependent electronic structure of organolead perovskite materials". In: *Chemistry of Materials* 27.12 (2015), pp. 4405–4412.

[16] M. L. Agiorgousis et al. "Strong covalency-induced recombination centers in perovskite solar cell material $CH_3NH_3PbI_3$". In: *Journal of the American Chemical Society* 136.41 (2014), pp. 14570–14575.

[17] H.-S. Duan et al. "The identification and characterization of defect states in hybrid organic–inorganic perovskite photovoltaics". In: *Physical chemistry chemical physics* 17.1 (2015), pp. 112–116.

[18] M.-C. Jung et al. "The presence of CH_3NH_2 neutral species in organometal halide perovskite films". In: *Applied Physics Letters* 108.7 (2016), p. 073901.

[19] J. Kim et al. "The role of intrinsic defects in methylammonium lead iodide perovskite". In: *The journal of physical chemistry letters* 5.8 (2014), pp. 1312–1317.

[20] G.-J. A. Wetzelaer et al. "Trap-assisted non-radiative recombination in organic–inorganic perovskite solar cells". In: *Advanced Materials* 27.11 (2015), pp. 1837–1841.

[21] S. D. Stranks et al. "Recombination kinetics in organic-inorganic perovskites: excitons, free charge, and subgap states". In: *Physical Review Applied* 2.3 (2014), p. 034007.

[22] A. Baumann et al. "Identification of trap states in perovskite solar cells". In: *The journal of physical chemistry letters* 6.12 (2015), pp. 2350–2354.

[23] X. Wen et al. "Defect trapping states and charge carrier recombination in organic-inorganic halide perovskites". In: *Journal of Materials Chemistry C* 4.4 (2016), pp. 793–800.

[24] X. Fang et al. "Effect of excess $PbBr_2$ on photoluminescence spectra of $CH_3NH_3PbBr_3$ perovskite particles at room temperature". In: *Applied Physics Letters* 108.7 (2016), p. 071109.

[25] T. Leijtens et al. "Modulating the electron–hole interaction in a hybrid lead halide perovskite with an electric field". In: *Journal of the American Chemical Society* 137.49 (2015), pp. 15451–15459.

[26] H.-H. Fang et al. "Photoluminescence enhancement in formamidinium lead iodide thin films". In: *Advanced Functional Materials* 26.26 (2016), pp. 4653–4659.

[27] N. Aristidou et al. "The role of oxygen in the degradation of methylammonium lead trihalide perovskite photoactive layers". In: *Angewandte Chemie International Edition* 54.28 (2015), pp. 8208–8212.

[28] H. J. Queisser and E. E. Haller. "Defects in semiconductors: some fatal, some vital". In: *Science* 281.5379 (1998), pp. 945–950.

[29] J. Chilla, O. Buccafusca, and J. Rocca. "Origin of photoluminescence signals obtained by picosecond-excitation correlation measurements". In: *Physical Review B* 48.19 (1993), p. 14347.

[30] D. Liu, X. Xu, and Y. Chen. "Photoluminescence-excitation-correlation spectroscopic study of a high-density two-dimensional electron gas in $GaAs/Al_{0.3}Ga_{0.7}$ As modulation-doped quantum wells". In: *Physical Review B* 49.7 (1994), p. 4640.

[31] R. Kumar and A. Vengurlekar. "Nonlinear picosecond excitation-correlation luminescence due to free electron-hole pairs in GaAs". In: *Physical Review B* 54.15 (1996), p. 10292.

[32] R. Mondal et al. "Pauli blocking dynamics in optically excited quantum dots: A picosecond excitation-correlation spectroscopic study". In: *Physical Review B* 87.11 (2013), p. 115317.

[33] M. Borgwardt et al. "Excitation correlation photoluminescence in the presence of Shockley-Read-Hall recombination". In: *Journal of Applied Physics* 117.21 (2015), p. 215702.

[34] H. Cho et al. "Overcoming the electroluminescence efficiency limitations of perovskite light-emitting diodes". In: *Science* 350.6265 (2015), pp. 1222–1225.

[35] M. Saba et al. "Correlated electron–hole plasma in organometal perovskites". In: *Nature communications* 5 (2014), p. 5049.

[36] W.-J. Yin, T. Shi, and Y. Yan. "Unusual defect physics in $CH_3NH_3PbI_3$ perovskite solar cell absorber". In: *Applied Physics Letters* 104.6 (2014), p. 063903.

[37] M. H. Du. "Efficient carrier transport in halide perovskites: theoretical perspectives". In: *Journal of Materials Chemistry A* 2.24 (2014), pp. 9091–9098.

[38] H. Shi and M.-H. Du. "Shallow halogen vacancies in halide optoelectronic materials". In: *Physical Review B* 90.17 (2014), p. 174103.

[39] M.-H. Du. "Density functional calculations of native defects in $CH_3NH_3PbI_3$: effects of spin–orbit coupling and self-interaction error". In: *The journal of physical chemistry letters* 6.8 (2015), pp. 1461–1466.

[40] G. Tränkle et al. "Dimensionality dependence of the band-gap renormalization in two- and three-dimensional electron-hole plasmas in GaAs". In: *Physical review letters* 58.4 (1987), p. 419.

[41] Q. A. Akkerman et al. "Solution synthesis approach to colloidal cesium lead halide perovskite nanoplatelets with monolayer-level thickness control". In: *Journal of the American Chemical Society* 138.3 (2016), pp. 1010–1016.

[42] N. S. Makarov et al. "Spectral and dynamical properties of single excitons, biexcitons, and trions in cesium–lead-halide perovskite quantum dots". In: *Nano letters* 16.4 (2016), pp. 2349–2362.

[43] V. I. Klimov. "Optical nonlinearities and ultrafast carrier dynamics in semiconductor nanocrystals". In: *Journal of Physical Chemistry B* 104.26 (2000), pp. 6112–6123.

[44] V. Sarritzu et al. "Perovskite Excitonics: Primary Exciton Creation and Crossover from Free Carriers to a Secondary Exciton Phase". In: *Advanced Optical Materials* (2017).

Chapter 4

Ultrafast Dynamics at the Structural Phase Transition of Hybrid Lead Iodide Perovskites

In the previous chapter we saw that one major loss channel for light emission in hybrid perovskites at high excitation densities is due to non-radiative Auger recombination, a substantial obstacle for lasing applications. In this chapter we present low temperature transient absorption studies on the compound methyl-ammonium lead iodide ($MAPbI_3$). Exploiting the population transfer between coexisting structural phases of the material, we demonstrate a possibility to overcome the problem of Auger recombination and show that the threshold for amplified spontaneous emission (ASE) can be lowered for properly engineered intermixing. In addition, we will present a short perspective for suitable candidates for our suggested dual-phase architectures and summarize current developments in the field.[1]

4.1 Introduction

The high photoluminescence quantum yields of hybrid perovskites suggest the incorporation as active materials for lasing applications [2]. Amplified spontaneous emission (ASE) and lasing have been shown in a vast variety of different morphologies, comprising single crystals [3], nanowires [4, 5], films of colloidal nanocrystals [6] and polycrystalline thin films [7]. To the date of this study, all reports about gain thresholds in hybrid perovskites were based on experiments, using ultra-short pulses of fs/ns length to access the carrier densities for stimulated emission. Cadelano *et al.* [8] demonstrated, that the main drawbacks for achieving technologically relevant continuous wave (cw) lasing are lacking heat dissipation, mainly due to the poor thermal conductivity of hybrid perovskites [9]. They concluded, that the heat load could be drastically decreased by lowering the ASE threshold. Population inversion in semiconductors

[1]The content of this chapter is adapted with permission from Neutzner *et al.*, "A dual-phase architecture for efficient amplified spontaneous emission in lead iodide perovskites",*J. Mater. Chem. C*, 2016,4, 4630-4633. Copyright (2016) The Royal Society of Chemistry [1]

requires high carrier densities, which are prone to multi-particle Auger processes causing two detrimental consequences: shift of the gain threshold towards higher excitation densities due to a decrease of the available carrier population and dissipation of the excess energy into the lattice, locally heating the material [10]. In quantum well lasers, this problem has been tackled by embedding spatially separated domains for population inversion and pumping. The concept allows to allocate and, in situ, lower the excited carrier population in order to decrease the probability of Auger recombination and subsequently diminish the threshold for population inversion [11–13]. In the following we demonstrate, as a proof of principle, that a similar concept can be realized by exploiting coexisting orthorhombic and tetragonal crystal domains at temperatures below 160 K [14, 15]. Using transient absorption (TA) spectroscopy, we show, that these domains conceptually represent spatially separated pumping and emission regions with efficient carrier transfer to the emission sites, a scenario leading to a reduced threshold for ASE. From our results, we deduce simple design parameters to engineer phase-architectures in this class of self-assembled materials.

4.1.1 Structural phase transition in $MAPbI_3$

Structural phase transitions are a common phenomenon in perovskite crystal structures and need to be taken into account when investigating light-matter interactions, since they usually alter the electronic band structure and thus the electro-optical properties of a material. The $MAPbI_3$ studied here exhibits four structural phases ($\alpha, \beta, \gamma, \delta$), of which three describe perovskite structures ($\alpha - \gamma$) [15]. The high temperature α phase forms at temperatures above $\sim$ 330 K and adopts a cubic structure (strictly speaking, the size and dipole moment of the organic cation correlated to structural disorder in the material, prevents full transition into the cubic structure and results in the P4mm spacegroup [15]). At room temperature, rotations of the PbI_6 octahedra around the c-axis of the material result in a tetrogonal unit cell ($\beta-$ phase, space group I4cm) with doubled volume and decreased crystal symmetry [16, 17]. A further structural transition can be observed below $\sim$ 160 K. The PbI_6-octahedra tilt out of the ab-plane and arrange in an orthorhombic crystal structure (space group Pnma) [14]. The unit cell in the orthorhombic phase experiences an eight fold volume increase with respect to the tetragonal unit cell [15]. Consequently, the absorption onset of the material exhibits abrupt shifts to higher energies with every temperature induced reduction of symmetry [18]. [2]

[2] The absorption shift at the cubic to tetragonal transition point in $MAPbI_3$ is almost not observable. Reason for this are fluctuations of the crystal structure induced by the organic cation [19].

4.2 Experimental

Sample preparation and treatment: for the work in this chapter, two different sample morphologies were investigated, polycrystalline $MAPbI_3$ films on glass with < 200 nm and ~ 1 µm crystal sizes, prepared according to the procedures described in the methods chapter. All measurements were carried out in nitrogen environment using an exchange gas continuous flow cryostat (Oxford Instruments Optistat CF). The temperature was varied between 77 K and room temperature, using liquid nitrogen as coolant and all measurements were taken in the heating up cycle after cooling down to 77 K to prevent ambiguous data due to hysteresis effects, discussed in the following section. The samples for this work were prepared by Marina Gandini who also performed the SEM measurements, using a commercial high vacuum, tungsten filament Jeol 6010-LV SEM, with a working bias of 20 kV.

Steady-state absorbance and photoluminescence: optical absorbance measurements were performed in a photo-induced absorption setup, based on a 30 W tungsten halogen lamp as illumination source and employing parabolic mirror optics. The transmitted light was modulated with a mechanical chopper, thereupon dispersed by a SP DK240 1/4 Meter monochromator and detected with a silicon photodiode in conjunction with a Stanford Instruments SR830 lock-in amplifier, referenced to the chopper frequency. All spectra were corrected by the transmission through the bare substrate. Steady-state photoluminescence measurements were taken from the same sample spot, using the above detection system and a green diode laser with 0.5 W/cm^2 at 560 nm central wavelength as excitation source.

Transient absorption measurements: For all TA measurements the fs pump probe system described in detail in the methods chapter was employed. The pump energy was kept at 250 nJ/cm^2, resulting in excitation densities of $6.5x10^{16}/cm^3$, $5.7x10^{16}/cm^3$ and $4.9x10^{16}/cm^3$ for 530, 760 and 400 nm respectively.

Power dependent photoluminescence measurements: the samples were excited with 120 fs pulses at 400 nm, focused by a 150 mm lens and resulting in a spot radius of 65 µm on the sample. The corresponding excitation densities for the different pump powers were calculated according to Equation 2.7.

4.3 Results

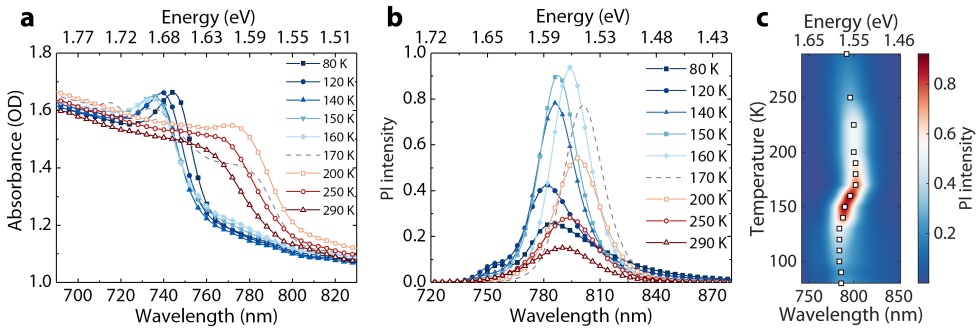

Figure 4.1
(a) Temperature dependence of the absorbance. **(b)** Spectral evolution of the photoluminescence as function of temperature. **(c)** Evolution of the low energy feature, the white squares are a guide to the eye to mark the PL maxima (adapted from [1]).

Figure 4.1 displays the absorption and photoluminescence spectra of a poly-crystalline $MAPbI_3$ film on glass, taken at different temperatures. The band gap in the orthorhombic phase is larger, as reported earlier [20–22] and the absorption edges are situated at 740 nm and 760 nm at 150 K and 290 K respectively. Above and below the phase transition, a blue-shift of the absorption edge with increasing temperature can be observed due to a continuous expansion/shrinkage of the lattice, which can be described by an empirical Varshni law [23].
Despite being reported in various studies, the exact temperature at which the transition occurs remains somewhat ambiguous. A study on single crystals demonstrated an abrupt transition at ~ 160 K [14] whereas other show that polycrystalline films exhibit a prolonged transition over several tens of degrees of Kelvin considering the optical signatures of both phases which follows a hysteretic behaviour upon heating and cooling [20, 24–26]. A recent micro-photoluminescence study [27] concludes that defects affect the transition temperature, acting as nucleation centers for the transition [28], which induces strain in the adjacent crystal environment as has been observed for other perovskite compounds [29]. The phase transition temperature therefore depends on the distribution of defects and the history of the sample, thus explaining the observed hysteresis.
Figure 4.1 (a) shows the existence of the tetragonal spectral fingerprint in absorption down to 140 K. A distinct trend can also be observed in the photoluminescence spectra, presented in Figure 4.1 (b) and (c). A lower energy emission signature accompanied by the emission from the orthorhombic phase below 160 K dominates over the whole temperature range, indicating carrier transfer from the higher energy feature. After following the red-shift of the tetragonal absorption edge above the phase transition temperature, the emission peak blue-shifts between 170 and 130 K, passes through a maximum in luminescence intensity and starts red-shifting again below 130 K. The nature of this lower energy emission feature below the phase transition temperature has been discussed in previous studies and assigned either to the signature

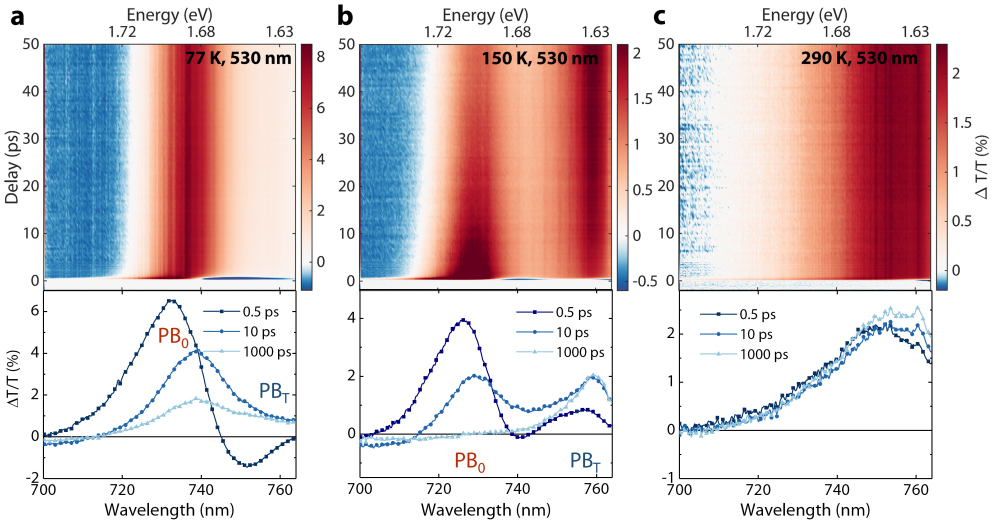

Figure 4.2
Spectral evolution of the pump probe signal within 50 ps at 77 K **(a)**, 150 K **(b)** and room temperature **(c)**. The bottom panels show the representative spectra for three time steps. The signal stemming from tetragonal domains is visible as a red shoulder till 77 K (adapted from [1]).

of a bound-exciton next to the free-exciton emission of the orthorhombic phase [7, 30], thus corresponding to the same structural phase, or to the concurrence of both structural phases within the anomalous temperature range [20, 25]. In temperature dependent X-ray diffraction (XRD) studies, Kong and Osherov *et al.* demonstrated independently that tetragonal and orthorhombic phases can coexist within an interval of 30 K around the transition temperature [25, 31]. However, the optical signature of lower energy emission sites can still be identified at temperatures below the predicted range. Therefore, endorsing the theoretical description of Yin *et al.* [32], Kong *et al.* proposed that this emission originates from inter-band gap defect states of the orthorhombic phase, by virtue of lead and iodide vacancies forming radiative recombination centres. More recent studies suggest that the low energy emission feature still originates from small tetragonal inclusions, potentially constrained to lattice defects or grain boundaries, but too scarce and confined to give detectable signal in XRD measurements [27, 31, 33]. The observed blue-shift between 170 and 130 K had been assigned to increased strain on the tetragonal domains caused by the orthorhombic environment and leading to an increase in band gap energy of the tetragonal phase [20, 27].

In the following, we performed fs-TA spectroscopy to assess the carrier transfer from the orthorhombic to the tetragonal domains at different temperatures, exciting the system at 530 nm. Figure 4.2 shows the TA spectra of a $MAPbI_3$ thin film on glass with ~ 1 µm crystallite sizes (see Fig. 4.6 (c)) taken at 77, 150 and 290 K. The dominant features in the spectra are the photo-bleach (PB) bands occurring by reason of state filling by the photo-excited carriers [21].

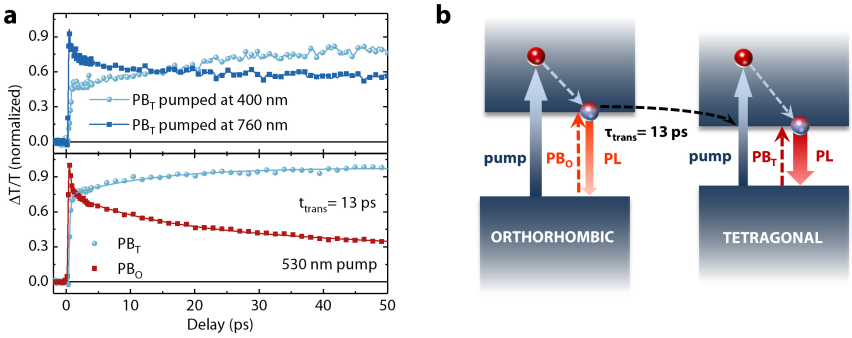

Figure 4.3
(a) Top panel: difference in temporal evolution of the tetragonal photobleach when only tetragonal sites (pump at 760 nm) and when both phases are excited (pump at 400 nm). Bottom panel: time evolution of both phases at 530 nm pump and corresponding fits according to Equation 4.1. All measurements are taken at 150 K. **(b)** Illustration of the suggested process (adapted from [1]).

In particular, below the phase transition temperature we identify two PB bands, peaking at 760 nm (PB_T) and 730 nm (PB_O), corresponding to the tetragonal and orthorhombic phase respectively. The time evolution reveals a quenching of PB_O and the accompanying growth of PB_T, most pronounced close to the phase transition temperature at 150 K. We can fit the dynamics of the two bleaches with simple exponentials including one term accounting for the transfer

$$\frac{\Delta T}{T}_{PB_O}(t) = \frac{1}{2}\left(1 + \mathrm{erf}\left(\frac{x}{w_p}\right)\right)\left[A_{O1}e^{-x\tau_{O1}} + A_{O2}\left(1 - e^{-x\tau_{O1}}\right)\cdot e^{x\tau_{O2}} + A_t e^{-x\tau_t}\right]$$
$$\frac{\Delta T}{T}_{PB_T}(t) = \frac{1}{2}\left(1 + \mathrm{erf}\left(\frac{x}{w_p}\right)\right)\left[A_{T1}e^{-x\tau_{T1}} + A_{T2}\left(1 - e^{-x\tau_{T1}}\right)\cdot e^{x\tau_{T2}} + A_t\left(1 - e^{-x\tau_t}\right)\right] \quad (4.1)$$

where the first term results from the convolution with the temporal pulse profile of width $w_p \sim 120$ fs, the first exponential term qualitatively describes the fast component τ_1 due to carrier cooling and A_t and τ_t are transfer strength and rate respectively. At 150 K we obtain a time constant of about $\sim 12 \pm 2$ ps for the transfer. The transfer behaviour can be observed down to 77 K, even though with lower efficiency and not only around the phase transition temperature, as claimed earlier [34]. Due to a decrease in density of tetragonal domains with lower temperature the efficiency of the process declines (the transfer rate and strength of transfer decreases, compare Table 4.1). To rule out other mechanisms, such as slow de-trapping and to unambiguously prove our hypothesis of population transfer we conduct a comparative TA experiment with two distinct pump wavelengths, to excite either only the tetragonal or both phases. Pumping at 400 nm and photo-exciting above the orthorhombic phase energy, we observe an increase of the tetragonal photo-bleach signal due to population transfer on ps timescales (Fig. 4.3 (b)). The dynamics change when exciting solely the tetragonal phase at

760 nm and exhibit the normal recombination behaviour of PB_T. Additionally, our experiment gives evidence for the presence of a distinct dual domain network for pumping and emission.

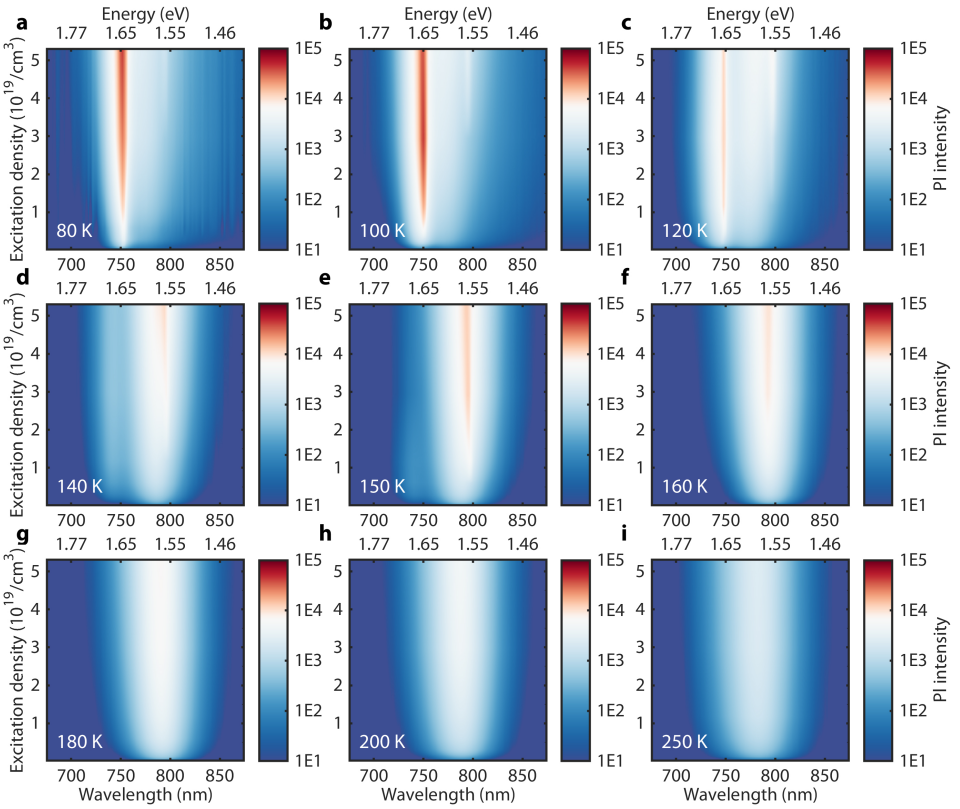

Figure 4.4
Steady-state photoluminescence as function of excitation density for 80 K **(a)**, 100 K **(b)**, 120 K **(c)**, 140 K **(d)**, 150 K **(e)**, 160 K **(f)**, 180 K **(g)**, 200 K **(h)** and 250 K **(i)** (adapted from [1]).

To test if the domain structure is able to lower the threshold for lasing, we performed power dependent steady-state photoluminescence measurements to determine the ASE thresholds. Figure 4.4 exhibits the resulting spectral maps as a function of excitation density for all investigated temperatures. To scrutinize the impact of population transfer, we performed measurements in 10 K steps around the phase transition temperature, represented in Figure 4.5. This relatively small range ensures immunity to major temperature induced effects and guarantees a critical density of tetragonal domains to observe a noticeable change. We find ASE thresholds at 1.45×10^{19} and 1.8×10^{19} cm^{-3} for 140 and 160 K respectively, whereas the threshold is lowered to 7×10^{18} at 150 K. This observation is backed by the fact, that transient absorption experiments showed the most efficient transfer at 150 K.

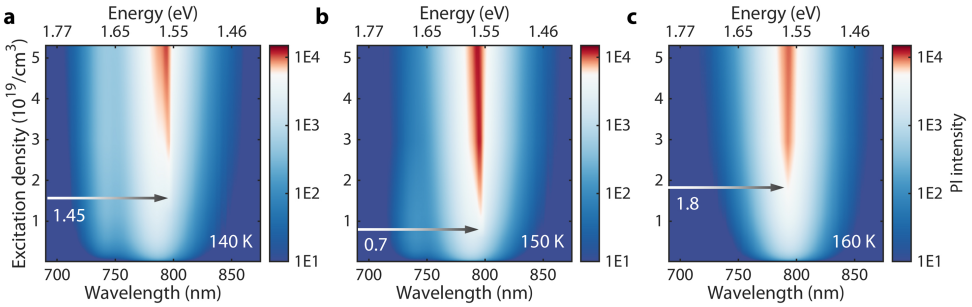

Figure 4.5
Detail of Figure 4 indicating the ASE thresholds for the tetragonal PL emission between 140-160 K ((**a**)-(**c**)) (adapted from [1]).

4.4 Discussion

Our results denote the possibility of population relocation from the orthorhombic to the tetragonal sites, thereby reducing the influence of non-radiative Auger recombination. This occurs due to efficient intermixing in a dual phase architecture, naturally developing in the crystalline semiconductor. If we want to implement and optimize such a principle in a potential system, which can operate at room temperature, it is necessary to devise specific design principles. The two important parameters are the transfer rate and transfer strength, influenced by the relative density and size of both domains. The key function of the transfer process is to restore the population losses. Transfer faster than Auger recombination in the emission sites would result in the loss of the transferred population. At the same time, the transfer has to be faster than recombination in the high energy phase, pointing out the necessity of precisely controlling this parameter.

We notice that the transfer rate is diffusion limited and therefore intrinsically coupled to the domain sizes and ratio between both phases, which follows from the observed temperature dependence. At lower temperatures, the transfer becomes slower and the amplitude of the transfer component decreases (compare Table 4.1). If we presume a mobility value of μ = 50 cm^{2}V^{-1}s^{-1}, as reported for $MAPbI_3$ at 150 K [35] we can estimate an effective distance traveled by the carriers before being quenched. With the observed transfer time of 13 ps and $L_D(n) = \sqrt{\tau_t \mu k_B T/e}$ we can estimate the mean effective extent of the orthorhombic domains to be 29 nm at 150 K. At 120 K, observing a transfer time of around 40 ps the effective length results to ~ 50 nm, indicating enlarging orthorhombic domains. If we compare the results with a film exhibiting smaller crystallites and hence a higher density of grain boundaries, we observe faster transfer times, due to a restriction of domain sizes but smaller transfer amplitudes. For efficient transfer, suitable engineering of the phase landscape is pivotal.

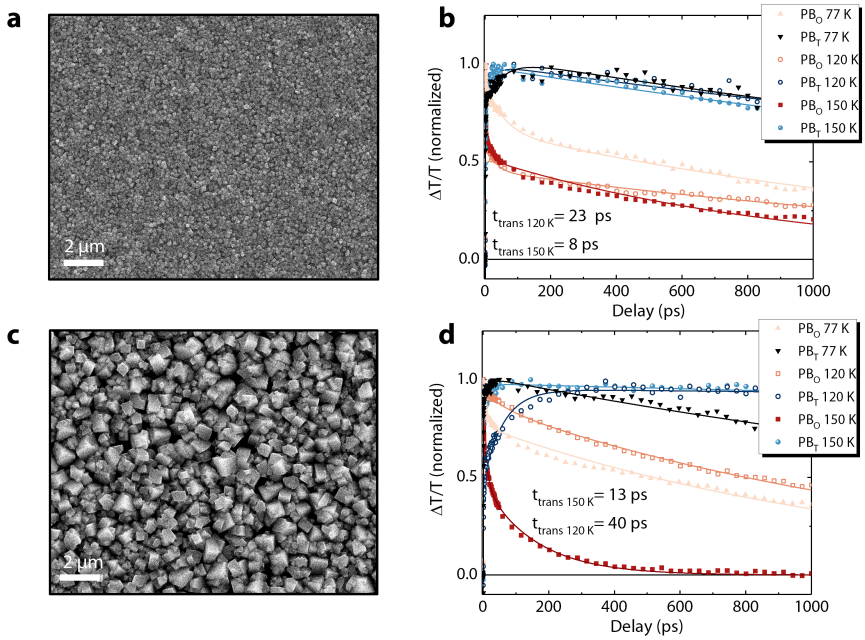

Figure 4.6
(a) SEM picture of a $MAPbI_3$-film with small crystallites (<200 nm) and **(b)** corresponding dynamics including fits for the tetragonal and orthorhombic bleach signals. **(c)** SEM picture of a $MAPbI_3$-film with large crystallites (1 µm) and **(d)** corresponding time evolution of the two photo bleach signals (adapted from [1]).

Fit parameters				
Temperature (K)	Crystal size (~ 1 µm)		Crystal size (<200 nm)	
	A_t	t_t (ps)	A_t	t_t (ps)
77	0.02 ± 0.01	40 ± 4	0.04 ± 0.02	160 ± 10
120	0.07 ± 0.005	39 ± 4	0.05 ± 0.004	23 ± 7
150	0.27 ± 0.01	12 ± 2	0.14 ± 0.01	8.1 ± 4

Table 4.1
Transfer amplitude and time after Equation 4.1 for the temperature dependent TA measurements of two $MAPbI_3$ films with different crystallite sizes, presented in Figure 4.6 (b), (d).

4.5 Conclusions and perspectives

In this chapter, we employed transient absorption spectroscopy to elucidate the interaction between the two structural phases in $MAPbI_3$ below the phase transition temperature. We gave evidence for the population transfer between orthorhombic and tetragonal domains forming around the phase transition temperature which could explain the previously observed anomalous photoluminescence behaviour in this material. Furthermore, we demonstrated that efficient transfer between the two phases can tackle the problem of Auger recombination and decrease the ASE threshold. We suggested fundamental design principles to develop mixed phase architectures for lasing applications. The concept pinpoints the balance between transfer and Auger rates, which are sensitive to the relative size and distribution of potential pumping and emission domains.

Recently, Jia *et al.* [36] demonstrated for the first time a $MAPbI_3$ based distributed feedback (DFB) laser operating under continuous wave conditions below the tetragonal-to-orthorhombic phase transition temperature, exploiting the here presented dual phase architecture for pumping and emission. These findings stress that engineering host-guest structures is a promising strategy to obtain efficient perovskite based gain media. Possible candidates for such systems could be matrices of perovskite nanocrystals [37], employing different halides and therefore bandgaps, to enable efficient charge transfer[3], multi-phase systems consisting of layered perovskites incorporating various inorganic layer thicknesses, which demonstrated already excellent photoluminescence properties for LED devices [38, 39] or core-shell structures, funneling the photo-excitations to the lower bandgap core [40].

Suitably engineered domain structures at room temperature, might finally pave the way towards the realization of the first electrically pumped hybrid perovskite laser.

[3]The main challenge here is to stabilize the domain landscape and avoid halide segregation.

References

[1] S. Neutzner et al. "A dual-phase architecture for efficient amplified spontaneous emission in lead iodide perovskites". In: *Journal of Materials Chemistry C* 4.21 (2016), pp. 4630–4633.

[2] P. J. Cegielski et al. "Integrated perovskite lasers on a silicon nitride waveguide platform by cost-effective high throughput fabrication". In: *Optics Express* 25.12 (2017), pp. 13199–13206.

[3] Q. Zhang et al. "Room-temperature near-infrared high-Q perovskite whispering-gallery planar nanolasers". In: *Nano Lett* 14.10 (2014), pp. 5995–6001.

[4] Y. Fu et al. "Nanowire lasers of formamidinium lead halide perovskites and their stabilized alloys with improved stability". In: *Nano letters* 16.2 (2016), pp. 1000–1008.

[5] H. Zhu et al. "Lead halide perovskite nanowire lasers with low lasing thresholds and high quality factors". In: *Nature materials* 14.6 (2015), pp. 636–642.

[6] S. Yakunin et al. "Low-threshold amplified spontaneous emission and lasing from colloidal nanocrystals of caesium lead halide perovskites". In: *Nature communications* 6 (2015), p. 8056.

[7] G. Xing et al. "Low-temperature solution-processed wavelength-tunable perovskites for lasing". In: *Nature materials* 13.5 (2014), pp. 476–480.

[8] M. Cadelano et al. "Can trihalide Lead perovskites support continuous wave lasing?" In: *Advanced Optical Materials* 3.11 (2015), pp. 1557–1564.

[9] A. Pisoni et al. "Ultra-low thermal conductivity in organic–inorganic hybrid perovskite $CH_3NH_3PbI_3$". In: *The journal of physical chemistry letters* 5.14 (2014), pp. 2488–2492.

[10] M. Saba et al. "Correlated electron–hole plasma in organometal perovskites". In: *Nature communications* 5 (2014), p. 5049.

[11] A. Uskov et al. "Theory of a self-assembled quantum-dot semiconductor laser with Auger carrier capture: Quantum efficiency and nonlinear gain". In: *Applied physics letters* 73.11 (1998), pp. 1499–1501.

[12] O. Gauthier-Lafaye et al. "Long-wavelength ($\approx$ 15.5 μ m) unipolar semiconductor laser in GaAs quantum wells". In: *Applied physics letters* 71.25 (1997), pp. 3619–3621.

[13] F. Julien et al. "Optically pumped intersub-band emission in quantum wells". In: *Electronics Letters* 31.10 (1995), pp. 838–839.

[14] T. Baikie et al. "Synthesis and crystal chemistry of the hybrid perovskite $(CH_3NH_3)PbI_3$ for solid-state sensitised solar cell applications". In: *Journal of Materials Chemistry A* 1.18 (2013), pp. 5628–5641.

[15] C. C. Stoumpos, C. D. Malliakas, and M. G. Kanatzidis. "Semiconducting tin and lead iodide perovskites with organic cations: phase transitions, high mobilities, and near-infrared photoluminescent properties". In: *Inorganic chemistry* 52.15 (2013), pp. 9019–9038.

[16] Y. Kawamura, H. Mashiyama, and K. Hasebe. "Structural study on cubic–tetragonal transition of $CH_3NH_3PbI_3$". In: *Journal of the Physical Society of Japan* 71.7 (2002), pp. 1694–1697.

[17] A. Poglitsch and D. Weber. "Dynamic disorder in methylammoniumtrihalogenoplumbates (II) observed by millimeter-wave spectroscopy". In: *The Journal of chemical physics* 87.11 (1987), pp. 6373–6378.

[18] J. Even, L. Pedesseau, and C. Katan. "Analysis of multivalley and multibandgap absorption and enhancement of free carriers related to exciton screening in hybrid perovskites". In: *The Journal of Physical Chemistry C* 118.22 (2014), pp. 11566–11572.

[19] C. Quarti et al. "Structural and optical properties of methylammonium lead iodide across the tetragonal to cubic phase transition: implications for perovskite solar cells". In: *Energy & Environmental Science* 9.1 (2016), pp. 155–163.

[20] C. Wehrenfennig et al. "Charge carrier recombination channels in the low-temperature phase of organic-inorganic lead halide perovskite thin films". In: *APL Materials* 2.8 (2014), p. 081513.

[21] G. Grancini et al. "Role of microstructure in the electron–hole interaction of hybrid lead halide perovskites". In: *Nature photonics* 9.10 (2015), pp. 695–701.

[22] V. D'Innocenzo et al. "Excitons versus free charges in organo-lead tri-halide perovskites". In: *Nature communications* 5 (2014), p. 3586.

[23] Y. P. Varshni. "Temperature dependence of the energy gap in semiconductors". In: *physica* 34.1 (1967), pp. 149–154.

[24] K. Wu et al. "Temperature-dependent excitonic photoluminescence of hybrid organometal halide perovskite films". In: *Physical Chemistry Chemical Physics* 16.41 (2014), pp. 22476–22481.

[25] W. Kong et al. "Characterization of an abnormal photoluminescence behavior upon crystal-phase transition of perovskite $CH_3NH_3PbI_3$". In: *Physical Chemistry Chemical Physics* 17.25 (2015), pp. 16405–16411.

[26] F. Panzer et al. "Reversible Laser-Induced Amplified Spontaneous Emission from Coexisting Tetragonal and Orthorhombic Phases in Hybrid Lead Halide Perovskites". In: *Advanced Optical Materials* 4.6 (2016), pp. 917–928.

[27] A. Dobrovolsky et al. "Defect-induced local variation of crystal phase transition temperature in metal-halide perovskites". In: *Nature communications* 8.1 (2017), p. 34.

[28] A. Levanyuk and A. Sigov. "Influence of defects on structural phase transitions". In: *Ferroelectrics* 63.1 (1985), pp. 39–48.

[29] R. Zeches et al. "A strain-driven morphotropic phase boundary in $BiFeO_3$". In: *science* 326.5955 (2009), pp. 977–980.

[30] H.-H. Fang et al. "Photophysics of organic–inorganic hybrid lead iodide perovskite single crystals". In: *Advanced Functional Materials* 25.16 (2015), pp. 2378–2385.

[31] A. Osherov et al. "The impact of phase retention on the structural and optoelectronic properties of metal halide perovskites". In: *Advanced Materials* 28.48 (2016), pp. 10757–10763.

[32] W.-J. Yin, T. Shi, and Y. Yan. "Unusual defect physics in $CH_3NH_3PbI_3$ perovskite solar cell absorber". In: *Applied Physics Letters* 104.6 (2014), p. 063903.

[33] K. Galkowski et al. "Spatially resolved studies of the phases and morphology of methylammonium and formamidinium lead tri-halide perovskites". In: *Nanoscale* 9.9 (2017), pp. 3222–3230.

[34] H. Wang, L. Whittaker-Brooks, and G. R. Fleming. "Exciton and free charge dynamics of methylammonium lead iodide perovskites are different in the tetragonal and orthorhombic phases". In: *The Journal of Physical Chemistry C* 119.34 (2015), pp. 19590–19595.

[35] R. L. Milot et al. "Temperature-Dependent Charge-Carrier Dynamics in $CH_3NH_3PbI_3$ Perovskite Thin Films". In: *Advanced Functional Materials* 25.39 (2015), pp. 6218–6227.

[36] Y. Jia et al. "Continuous-wave lasing in an organic–inorganic lead halide perovskite semiconductor". In: *Nature Photonics* 11.12 (2017), p. 784.

[37] D. Marongiu et al. "Self-Assembled Lead Halide Perovskite Nanocrystals in a Perovskite Matrix". In: *ACS Energy Letters* 2.4 (2017), pp. 769–775.

[38] M. Yuan et al. "Perovskite energy funnels for efficient light-emitting diodes". In: *Nature nanotechnology* 11.10 (2016), pp. 872–877.

[39] J. Byun et al. "Efficient Visible Quasi-2D Perovskite Light-Emitting Diodes". In: *Advanced Materials* 28.34 (2016), pp. 7515–7520.

[40] S. A. Veldhuis et al. "Benzyl Alcohol-Treated $CH_3NH_3PbBr_3$ Nanocrystals Exhibiting High Luminescence, Stability, and Ultralow Amplified Spontaneous Emission Thresholds". In: *Nano letters* 17.12 (2017), pp. 7424–7432.

Chapter 5

The Role of Crystal Structure in the Optical Properties and Excitonic Many Body Effects in Two Dimensional Lead Halide Perovskites

Layered hybrid organic-inorganic perovskites (2D HOIPs) have been intensely investigated before the success of their three dimensional counterpart in the field of photovoltaics. Owing to electronic and dielectric confinement effects, they sustain strongly bound excitons at room temperature. In this chapter we demonstrate that their particular electro-optical properties are heavily influenced by non-negligible contributions to their excitonic correlations from the peculiar lattice structure and its polar fluctuations, both of which are controlled via the chemical nature of the organic counter-cation.

First we elucidate the role of crystal structure in the particular broad-band emission of some 2D HOIPs. We compare two prototypical compounds, namely, $(NBT)_2PbI_4$ (NBT = n-butylammonium) and $(EDBE)PbI_4$ (EDBE = 2,2- (ethylenedioxy)bis(ethylammonium)), whereas the latter exhibits a higher degree of Pb-I bond and I-Pb-I bond angle deformation. We show, that an increased structural distortion influences the defectivity of the system by lowering defect formation energies, which favors exciton self-trapping.

Furthermore, we address the distinct fine-structure within the excitonic transition of 2D HOIPs at low temperatures. We present a phenomenological, yet quantitative framework to simulate the excitonic absorption line-shape in single-layer HOIPs, based on the two-dimensional Wannier formalism. We include four distinct excitonic states and additional vibronic progressions. Intriguingly, the associated Huang-Rhys factors and the relevant phonon energies show substantial variance with temperature and with the choice of the organic cation. This points to the hybrid nature of the line-shape, with a form well described by a Wannier formalism, but with signatures of strong coupling to localized vibrations and polaronic effects perceived through excitons.

Finally, we use two-dimensional coherent spectroscopy to investigate excitonic many-body effects in $(PEA)_2PbI_4$ (PEA = phenylethylammonium). We directly measure the biexciton binding energy which is similar to those reported for other two-dimensional materials such as the transition-metal dichalchogenides. We demonstrate, that the binding energy decreases at room temperature due to strong effects of dynamic disorder and lattice fluctuations.[1]

[1]The content of this chapter is adapted with permission from the following publications: Cortecchia *et al.*, "Broadband Emission in Two-Dimensional Hybrid Perovskites: The Role of Structural Deformation", *J. Am. Chem. Soc.*, 2017, 139, 1, 39-42, Copyright (2017) American Chemical Society [1] and Thouin and Neutzner *et al.*, "Stable Biexcitons in Two-Dimensional Metal-Halide Perovskites with Strong Dynamic Lattice Disorder"', manuscript accepted in *Phys. Rev. Mater.*, arXiv:**1712.04733**, Copyright (2018) American Physical Society [2]. A third manuscript is in preparation.

5.1 Introduction

Hybrid perovskites offer the appealing possibility to tune their dimensionality governing their electro-optical properties via the choice of the organic counter cation [3]. Albeit the frontier orbitals to the electronic structure are given by the metal-halide network, the organic cation plays a key role in defining the structural configuration as well as the stability of the lattice [4]. When the organic moieties are long enough to isolate the lattice planes electronically, the latter form quantum-well like structures with strong two dimensional electronic confinement within the metal-halide layer [5].

As a consequence of such confinement strongly bound excitons are created, which have been reported as early as 1989 by Ishihara *et al.* [6], with binding energies of 200-300 meV. In a general context, a variational approach of electron-hole correlations predicts that excitons in strongly confined quantum wells experience a four-fold enhancement in binding energy with respect to the bulk semiconductor [7, 8], assuming a smooth dielectric environment around the well. This enhancement is generally observed in systems such as GaAs and is reflected in an exciton binding energy of 4 meV in the bulk and 16 meV in quantum wells [9]. Intriguingly, there is more than a ten-fold increase in the binding energies going from 3D lead-halide perovskites (10-20 meV [10]) to their 2D counterparts [6]. Beyond quantum confinement, dielectric confinement arising from the comparably low dielectric function of the intercalating organic layers increases the Coulomb correlations substantially, resulting in such a strong increase in the exciton binding energy [4, 6, 11, 12]. Owing to the large binding energy, clear and distinct excitonic transitions are observed in the linear absorption spectrum usually accompanied by narrow-band photoluminescence features.

Although being members of the family of excitonic two dimensional semiconductors, 2D hybrid lead halide perovskites demonstrate unique photophysical properties due to their particular structural and chemical composition [13]. They are prone to static and dynamic structural disorder which modulates their energetic landscape. Size and bonding scheme of the embodied organic templating cation can induce structural lattice deformations, in particular octahedral distortions [14]. Moreover, owing to a polar lattice, electron-phonon interactions and local dynamic fluctuations induced by relative motions of the organic moiety [15] influence the electronic correlations and thus the electro-optical properties of the material [10, 16–18]. Consequences of this complex inter-play are the topic of the current chapter and will be discussed on examples of the lead-iodide 2D perovskite family.

5.2 Experimental

Sample preparation and treatment: Polycrystalline films and single crystals of $(NBT)_2PbI_4$, $(PEA)_2PbI_4$ and $(EDBE)PbI_4$ were prepared as detailed in the methods chapter. For the thin films of $(PEA)_2PbI_4$ measured via 2D spectroscopy a more diluted precursor solution (0.1 M) was used by dissolving 24.9 mg of (PEA)I and 23 mg of PbI_2 in 500 µL of DMSO. The deposition steps remained the same resulting in films of approximately 80 nm thickness. All samples were prepared by Daniele Cortecchia.

Steady-state optical and Raman characterization: most measurements were performed by means of the setups described in the methods chapter. For the steady-state PL characterization in the first section of this chapter also a commercial setup, NanoLog (Horiba Jobin Yvon) was employed. Temperature dependent measurements were carried out in an exchange gas (OptistatCF, Oxford Instruments) continuous flow helium cryostat in the heating up cycle after going to liquid helium temperatures.

Temperature dependent x-ray diffraction measurements: the measurements were performed by collaborators from the School of Materials Science and Engineering, Singapore, in particular Teddy Salim. A commercial BRUKER D8 ADVANCE setup with Bragg Brentano geometry was used for thin film x-ray diffraction, based on CuKα radiation (λ = 1.54056 Å), with a step increment of 0.02° and 1 s acquisition time. Perovskite powders, obtained by gently grinding single crystals in a mortar, were measured with a SAXS/WAXS system Nano-inXider from Xenocs (power range 50kV, 0.6 mA) equipped with Linkam HFSX350 temperature stage. The measurements were performed with a beam size of 200 µm, a flux of 4 Mph/s, and a cooling-heating rate of 3° C with 1 min stabilization and 5 min exposure time. The software TOPAS 3.0 allowed to perform the Pawley fit by a fundamental parameters approach, using the reference structure reported by J. Calabrese *et al.*[19] as starting lattice parameters. The peak profile and background were fit with a TCHZ Pseudo-Voigt function and a Chebichev polynomial of fifth order (1/x function), respectively. Zero error, linear absorption coefficient, scale factor and lattice parameters were refined during the fitting.

2D coherent spectroscopy measurements: the employed COLBERT system is detailed in chapter 2. The used fluence of 20 µJ/cm² corresponds to a photon density of 2.6×10^{13}ph/cm². If we take into account an optical penetration depth of 288 nm in $(PEA)_2PbI_4$ and consider a single layer thickness of 0.8 nm, it is possible to estimate the number of photons absorbed in the top layer by multiplying the thickness ratio of the single layer to the whole film with the incident fluence, which results to 7.2×10^{10}ph/cm². The Mott density can be roughly estimated, considering an exciton Bohr radius of about 12 nm ($R_y^* \sim 50$, $\varepsilon_r \sim 7.5$), to be 2.2×10^{11} excitons/cm².[2] This short calculation demonstrates, that the excitation densities for the experiments were well below the Mott density.

[2]The actual Mott density is expected to be higher than this estimate, since our simple calculation does not take into account the effects of dielectric confinement and exciton normalization.

5.3 The role of crystal structure in the emission properties of 2D hybrid lead iodide perovskites

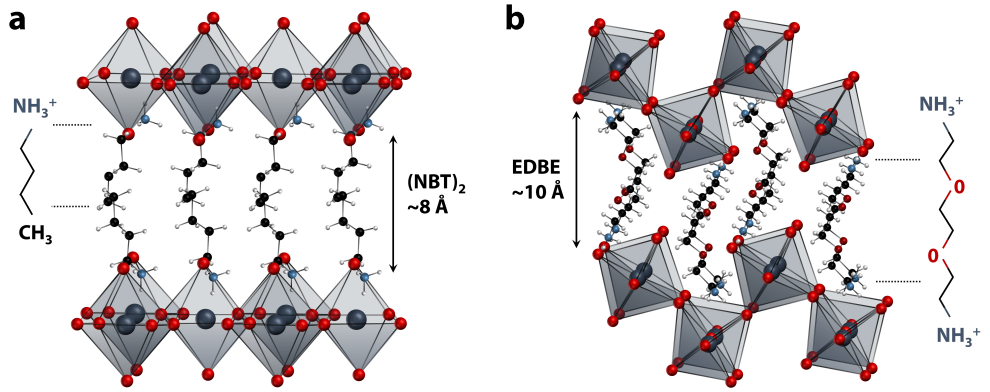

Figure 5.1
Crystal structures of **(a)** $(NBT)_2PbI_4$ and **(b)** $(EDBE)PbI_4$ including their organic cations: NBT=n-butylammonium and EDBE=2,2-(ethylenedioxy)bis(ethylammonium) (adapted from [1]).

A subclass of 2D perovskites shows broad Stokes-shifted photoluminescence bands with bandwidths of up to 700 meV [20], a particularity that has attracted interest due to its potential as white-light emitters for solid-state lighting. One important aspect is that this phenomenon has been observed without obvious correlations with crystal orientation or chemical composition [20–23]. The occurrence of broadband photoluminescence in Cl and Br-based compounds has been assigned to charge self-trapping [24–26], however, the question why self-trapping seems to be favored only in some compounds remains to be addressed. Structural deformations of 3D hybrid perovskites have been theoretically considered [14] and are known to play an important role in phenomena like piezo- and ferro-electricity or superconductivity [27]. Nevertheless, their influence on the emission properties of the material still requires detailed investigation. In the following we will demonstrate that structural deformations of the inorganic cage contribute to carrier localization and thus, broadband photoluminescence of the material.

5.3.1 Structural properties of $(NBT)_2PbI_4$ and $(EDBE)PbI_4$

In this work we consider two different 2D perovskites employing the same inorganic framework (PbI_4^{2+}) but different organic cations, the monotopic NBT (= n-butylammonium) and the ditopic EDBE (= (ethylenedioxy)bis(ethylammonium)). The two organic molecules link the inorganic sheets along different crystal directions, and the resulting structures are de-

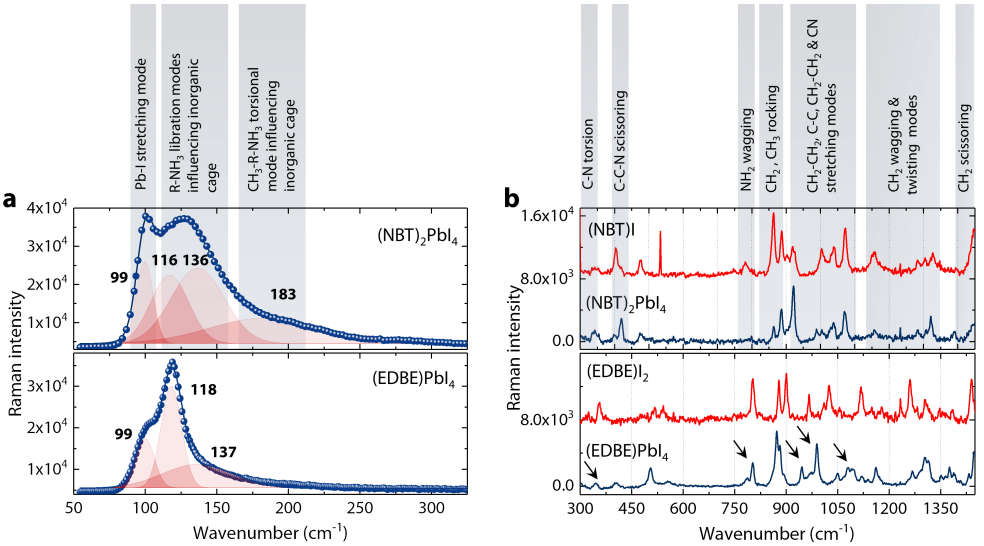

Figure 5.2
Raman spectra of $(NBT)_2PbI_4$ and $(EDBE)PbI_4$: **(a)** represents the vibrational modes affecting the inorganic cage. **(b)** shows the modes of the organic constituent (blue) in comparison to the vibrational modes of the pure iodide salts (red). The arrows indicate changes of $EDBE^{2+}$ modes when embedded in the perovskite structure. Modes in (NBT)I were assigned after [28] (adapted from [1]).

picted in Figure 5.1. $(NBT)_2PbI_4$ is flat and oriented along the <100> direction, resulting in an orthorhombic unit cell, whereas $(EDBE)PbI_4$ exhibits a <110>-oriented monoclinic crystal structure. [20, 22].

We used Raman spectroscopy on single perovskite crystals and their organic precursor salts to study the structural differences of the two compounds. Figure 5.3 (a) shows the low frequency range (80-300 cm^{-1}) of the two perovskite crystals. Following previous reports on the 3D parent $MAPbI_3$ [29–32], we can identify four bands between 80 and 300 cm^{-1} which can be assigned to the Pb-I stretching mode (99 cm^{-1}) and vibrational modes of the ammonium groups interacting with the inorganic cage. The bands at 116-118 and 136 cm^{-1} are formed by libration modes of the ammonium moiety and the signal at 183 cm^{-1} corresponds to a torsional movement between the NH_3 and CH_3 groups [29, 31]. Whereas the low energy Raman spectrum of $(NBT)_2PbI_4$ shows similarity to the mode spectrum of the 3D compound $MAPbI_3$, several bands are weakened or partly deactivated in $(EDBE)PbI_4$. $(EDBE)PbI_4$ exhibits higher octahedral distortions with respect to $(NBT)_2PbI_4$ leading to a decrease in signal at 99 cm^{-1}. The strength of the mode at 136 cm^{-1} is considerably diminished and the entire 183 cm^{-1} band missing. These observations can be explained by stronger conformational constraint of the ammonium groups at both ends of the molecular backbone due to their interactions with the inorganic cage.
The spectral range of 300 to 1500 cm^{-1} (Fig. 5.3 (b)) provides information about the Raman active modes of the organic constituents [30], amongst them various CH_2-CH_2 stretching, wag-

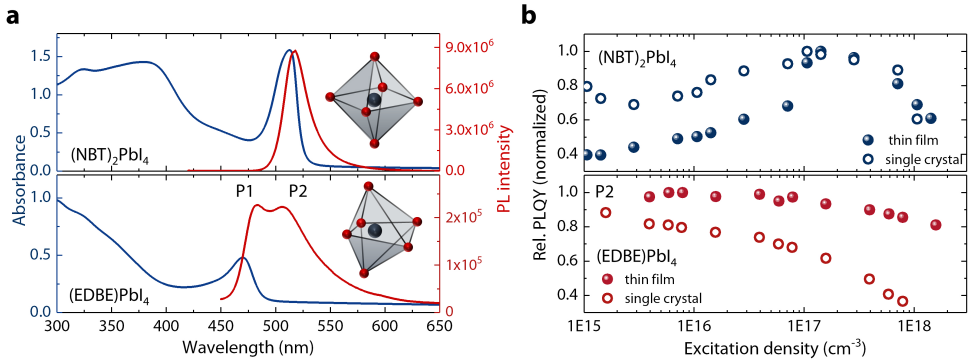

Figure 5.3
(a) Steady-state absorbance and photoluminescence of $(NBT)_2PbI_4$ (top panel) and $(EDBE)PbI_4$ (bottom panel). **(b)** Corresponding relative PLQY for the two compounds (adapted from [1]).

ging and twisting modes, CH_2 rocking as well as CCN deformation modes [28]. In Figure 5.3 (b) we compare the Raman spectra of the pristine precursor crystals (NBT)I and $(EDBE)I_2$ (red) with their corresponding 2D perovskites (dark blue). Whereas the organic modes of n-butyl-ammonium show only small changes in relative intensities when embedded in the perovskite crystal lattice, the Raman spectrum of $(EDBE)PbI_4$ exhibits significant differences in comparison to the pristine salt, with new modes appearing and intensities changing significantly. These changes suggest, that the perovskite framework imposes a different conformation of $EDBE^{2+}$, which in turn affects the distortion of the PbI_6 octahedral cage.

5.3.2 Optical properties of $(NBT)_2PbI_4$ and $(EDBE)PbI_4$

The structural peculiarities of the two perovskite compounds influence their optical properties. Figure 5.2 (a) shows the UV-vis absorption and steady-state PL spectra of the corresponding polycrystalline films. The band-edge of $(EDBE)PbI_4$ exhibits a blue-shift of 44 nm with respect to $(NBT)_2PbI_4$ and both films show excitonic resonances at 469 and 513 nm respectively. The significant increase in band-gap of $(EDBE)PbI_4$ is a characteristic fingerprint of <110> oriented perovskites due to the particular structural arrangement of the inorganic framework.
$(NBT)_2PbI_4$ exhibits a narrow PL band centered at 517 nm with a full width at half maximum (FWHM) of 25 nm. In contrast $(EDBE)PbI_4$ shows a narrow-band emission feature peaking at 483 nm (P1) overlapped by a broader band (FWHM = 70 nm) with a maximum at 507 nm (P2). Note that P1 can only be resolved in thinner films, thicker films show a broad mostly featureless PL band due to re-absorption losses. The absolute PLQY of both materials is below 1%, with $(NBT)_2PbI_4$ being the more emissive material. To obtain the relative PLQY over a meaningful range of excitation densities, all measurements were performed on thicker samples, where P1 could not be resolved in $(EDBE)PbI_4$, therefore, only P2 is shown in Figure 5.2 (b). Whereas the relative PLQY of $(NBT)_2PbI_4$ increases with excitation density until Auger recombination

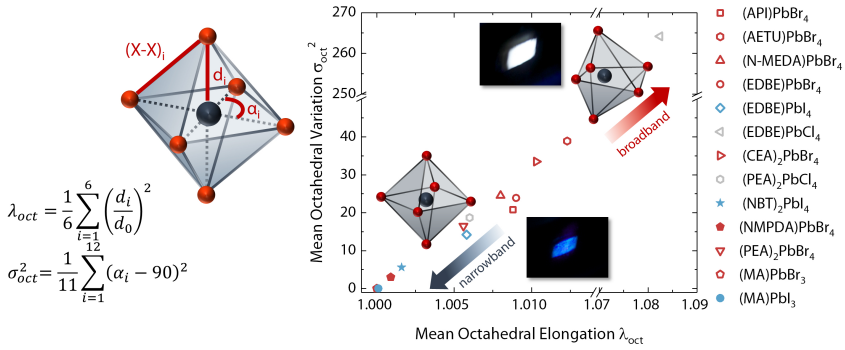

Figure 5.4
Left: definition of octahedral angle variance σ^2_{oct} and mean octahedral elongation λ_{oct} after K. Robinson *et al.* [36]. Right: octahedral angle variance σ^2_{oct} over mean octahedral elongation λ_{oct} for different hybrid perovskite compounds. Bromide based compounds are indicated in red, iodide based in blue and chloride based in gray. Open symbols denote compounds showing broadened photoluminescence features. Increased octahedral distortion is correlated with the appearance of broadened emission characteristics in hybrid perovskites. Structural parameters were calculated taking parameters from the following references [20–23, 37–41] (figure adapted and modified from [1]. Photographs of emitting crystals adapted from [21]).

starts to quench the excited state population, the intensity dependence of P2 in (EDBE)PbI_4 experiences a monotonic reduction, indicating that the emission stems from electronic states whose occupation probability diminishes with excitation density. Such a behavior relates to the emission from intra-gap defect states that start to saturate at higher densities, as has been observed in 3D perovskites [33–35] (compare also chapter 3). This suggests that (EDBE)PbI_4 is prone to a higher density of radiative colour centres than $(NBT)_2PbI_4$. Note that the same trends can be observed in thin films and single crystals.

To correlate the observed photoluminescence behaviour with the structural properties of 2D perovskites, the degree of structural distortion within the inorganic PbX_6 octahedral building blocks can be determined by following the classification of Robinson *et al.* [36]. To quantify deformations of the O_h symmetry, involving modifications of the Pb-X bond length (d) and X-Pb-X angle (α) which affect the edge lengths (X-X distances) and the O_h volume (V) [42], two parameters are introduced, the octahedral elongation λ_{oct} and octahedral angle variance σ^2_{oct}, defined as follows:

$$\lambda_{oct} = \frac{1}{6}\sum_{i=1}^{6}\left(\frac{d_i}{d_0}\right)^2 \tag{5.1}$$

$$\sigma^2_{oct} = \frac{1}{11}\sum_{i=1}^{12}(\alpha_i - 90)^2. \tag{5.2}$$

Here, d_i are the Pb-X bond length, d_0 stands for the center-to-vertex length of a regular octahe-

dron of same volume and α_i describe the X-Pb-X angles. Evaluating the structural parameters of different hybrid perovskite systems evidences that luminescence broadening is accompanied by increased structural distortion (see Fig. 5.4). In particular, $(NBT)_2PbI_4$ exhibits significantly less octahedral angle variance (σ^2_{oct} = 5.6; λ_{oct} = 1.0016) in comparison to $(EDBE)PbI_4$ (σ^2_{oct} = 14.2; λ_{oct} = 1.0058).
Ab initio calculations [1, 43] comparing defective and perfect crystals showed that in case of a neutral lead vacancy I^-_3 trimer formation by a proximate iodine moving towards the empty lattice site is favored in case of $(EDBE)PbI_4$, due to under-coordinated iodine at the interface between templating cation and inorganic cage. The formation of this defect is accompanied by strong local lattice rearrangements and can lower the energetic barrier for hole self-trapping [23, 24].

5.3.3 Conclusions 1

In summary, correlations between structure and photoluminescence broadening mechanisms in two prototypical 2D perovskites have been investigated. We showed that deformations of the inorganic building blocks in the <110> oriented $(EDBE)PbI_4$ can lower the defect formation energies and facilitate extrinsic charge self-trapping in the material, which results in the observed broad photoluminescence features. These findings underline the significance of understanding the structure-function relationship in hybrid perovskites to obtain full control over the electro-optical properties of these materials.

5.4 The origin of exciton fine structure in 2D hybrid lead iodide perovskites

In contrary to the characteristics of conventional 2D Wannier excitons which show only the strong optical signatures of the excitonic progression below the band edge, the spectra of 2D HOIPs develop a rich fine structure with the presence of multiple peaks distributed around the most intense one [44] at lower temperatures. Previously, the presence of similar spectral features has also been observed in the photoluminescence (PL) spectrum, which motivated the inclusion of vibronic progressions due to strong electron-phonon coupling [25, 44], as widely used in the case of localized states in molecular semiconductors. Here, we provide a more quantitative description of these spectral structures, invoking various considerations of exciton-lattice coupling. There is now an increasing consensus in the field that the charge carriers in 3D lead halide perovskites behave as large polarons within an intermediate electron-phonon coupling regime [45]. In addition to this conventional behaviour of any polar lattice, local lattice disorder induced by the relative motion of the organic cation has been suggested to affect the excitation dynamics substantially [10, 45]. Within such a context, we hypothesize the presence of distinct excitonic states, possibly generated via degeneracy lifting mechanisms

driven by polaronic effects. This, however, does not not discount for the contribution of low energy lattice vibrations to the optical absorption in the form of vibronic progressions. We analyze the vibrational and structural contributions to the excitonic correlations by systematically tuning the lattice parameters using temperature, the chemical nature of the organic cation, and the thickness of the quantum well. In the following, we introduce an empirical framework that reproduces such spectral structure quantitatively and provides insights into its origin.

5.4.1 Results

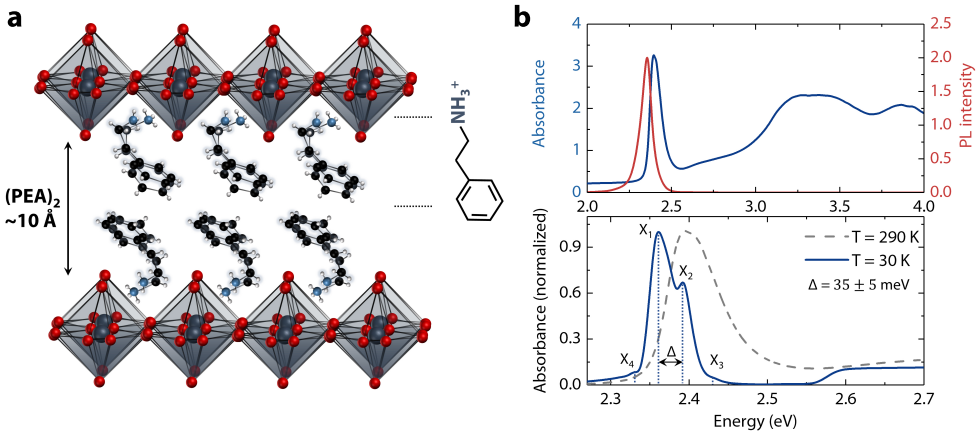

Figure 5.5
(a) Crystal structure of $(PEA)_2PbI_4$ including the organic cation PEA=phenylethylammonium. **(b)** Room temperature absorption and PL spectrum of $(PEA)_2PbI_4$ (top panel) and comparison of the excitonic absorption at low (30 K) and room temperature (290 K) (bottom panel) (adapted from [2]).

As first model system we consider a prototypical 2D HOIP, in particular polycrystalline films of the compound $(PEA)_2PbI_4$, consisting of monolayers of lead iodide octahedra lattices, separated by phenylethylammonium (PEA) cations. The structure is represented in Figure 5.5 (a) and confirmed to be monoclinic by wide-angle X-ray scattering (WAXS) measurements [2]. The steady-state absorption and photoluminescence of a typical sample at room temperature are shown in Figure 5.5 (b) with focus on the excitonic transition at 290 K and 30 K. The excitonic absorption peak is shifted by about 200 meV from the band edge and develops a fine structure at lower temperatures, consisting of four distinct excitonic transitions separated by ~ 35 ± 5 meV. Although they seem to appear only at low temperature due to reduced thermal disorder, they are also evident at room temperature as we will demonstrate in the next section. The evolution of the exciton absorption spectrum with temperature unveils the correlations between electronic and crystal structure. Figure 5.6 (c) presents the change of the excitonic absorption maximum as a function of temperature, which shows a monotonic red

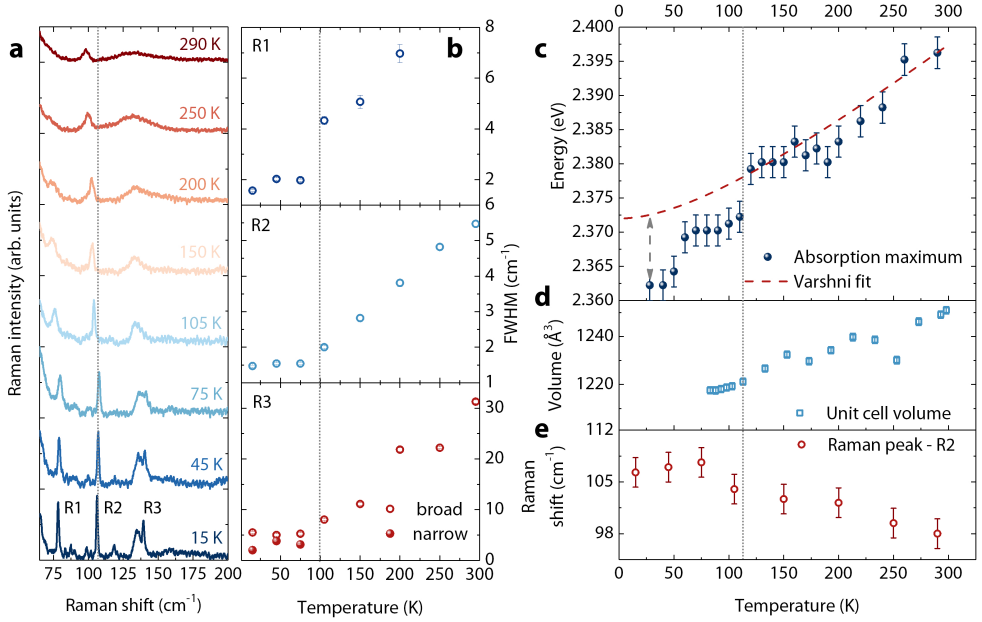

Figure 5.6
(a) Nonresonant Raman spectra of $(PEA)_2PbI_4$ as function of temperature and FWHM of the main modes R1, R2 and R3 **(b)**. **(c)** Excitonic peak position for various temperatures. The dotted line indicates the Varshni fit of the trend, assuming a temperature independent exciton binding energy. **(d)** Unit cell volume calculated from WAXS measurements for the different temperatures. **(e)** Position of the Raman peak R2 as function of temperature. The uncertainty bars in **(c)** and **(e)** represent the instrument resolution and spectral precision respectively (adapted from [2]).

shift with decreasing temperature until about 120 K. This trend can be explained due to lattice contraction, since the unit cell volume reduces concomitantly (see Fig. 5.6 (d)). If we assume that the exciton binding energy does not depend on temperature, the excitonic transition ($E_X(T) = E_G(T) - E_b$) will exhibit a similar trend, which can be fitted by a Varshni law [46] (compare equation 1.3) with the fit parameters $E_X = 2.372$ eV, $\alpha = 1.1 \times 10^{-4}$ eVK^{-1} and $\beta = 151$ K. We also observe a shift towards higher energies of the vibrational modes related to the inorganic cage, which is exemplarily shown for the Raman mode R2, corresponding to a longitudinal optical (LO) phonon mode [47] (see Fig. 5.6 (a) and (e)).

Below 100-120 K the behaviour starts to digress from the above trend and the excitonic absorption maximum experiences abrupt shifts at relatively well defined temperatures. We do not observe a first order phase transition over the experimentally accessible temperature of the WAXS measurements (lowest temperature was 83 K), which conforms with previous reports on this material [48]. It appears that, at lower temperatures, the volume reduction of the unit cell levels off (see Fig. 5.6 (d)). In addition, the Raman linewidths (in particular R1 and R2) are only weakly temperature dependent below 100 K. These observations can be interpreted as stiffening of the crystal lattice mainly caused by the steric hindrance between the

organic constituents.
Below 100 K, the Raman shift shows an anomalous behavior with a slight reduction in energy. Most strikingly, a well-defined peak appears in the vibrational band of mode R3, which increases in intensity at lower temperatures (see Fig. 5.6 (a)). This band can be assigned to a lattice phonon mode as we will show later. At higher temperatures, the large dynamic disorder in the perovskite lattice inhomogeneously broadens these vibrational modes. Considering a disorder-order transition at around 100 K, as suggested by the apparent stiffening of the crystal lattice, would explain the narrowing of the observed modes.

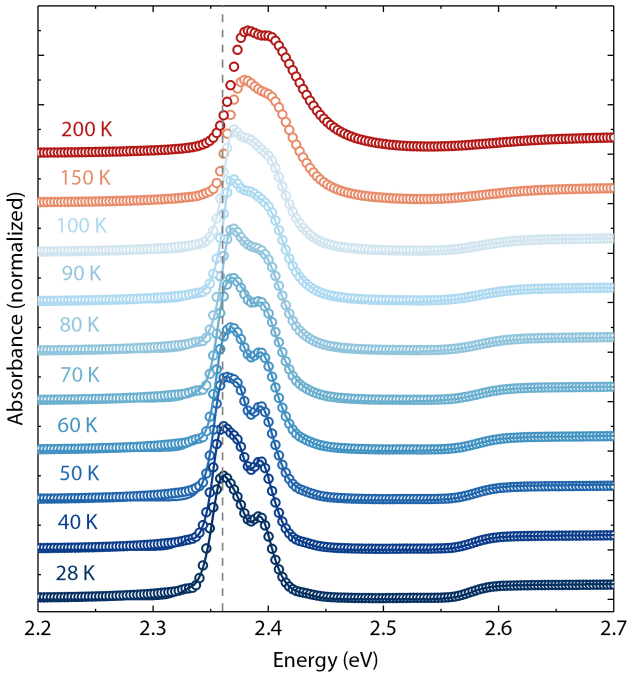

Figure 5.7
Experimental absorbance spectra of polycrystalline films of $(PEA)_2PbI_4$ taken at different temperatures (plotted as symbols) and numerical fits as described in the text (plotted as solid lines).

We use our model HOIP $(PEA)_2PbI_4$, to establish a formalism for the absorption spectral lineshape before exploring other systems incorporating different organic cations that induce various degrees of octahedral distortion. The absorbance spectra of a polycrystalline film of $(PEA)_2PbI_4$ taken at different temperatures are shown in Figure 5.7, focusing on the exciton resonance region and demonstrating the development of a rich fine structure with four distinct transitions separated by 35 ± 5 meV. The most intense peak also exhibits an asymmetric shape with a shoulder at higher energies, suggesting the presence of further buried structure within the broad lineshape. Upon increasing the temperature, there is a relative increase in absorption cross-section at higher energies and a reduction in clarity of the spectral fine structure.

Given the strong carrier confinement within the lead-iodide layer [4, 49], the absorption spectrum can be quantitatively modeled assuming a two-dimensional Wannier-Mott exciton [8, 50] (compare Eq. 1.20) and introducing two broadening parameters, Γ_{ex} and Γ_c for the exciton and free-carrier transitions, respectively. However, such a standard 2D exciton model is not sufficient to reproduce the observed fine-structure. To achieve a numerical fit, we introduce two modifications to Equation 1.20.

1. We conjecture that the four observed transitions correspond to distinct excitonic states and accordingly we re-distribute the intensity of the primary excitonic transition from Equation 1.20 among four equally spaced transitions of similar analytical form, but with binding energies approximately 35 meV and 70 meV higher and lower than the primary exciton binding energy. The relative intensities (X_i) of each of the four transitions are set as fit parameters.

2. To account for the asymmetric lineshapes, and more importantly to reproduce their temperature dependence, we introduce the contribution of electron-phonon coupling via appropriate Frank-Condon progressions on top of the exciton lines [51]. Due to the presence of multiple lattice vibrational modes that can couple to the electronic transitions, we employ a generalized Frank-Condon formalism as represented in Section 1.4.3 and redistribute the oscillator strength correspondingly.

Shown as solid lines in Figure 5.7 are the numerical fits of the experimental absorbance spectra, assuming a spacing between the excitonic states to be $\Delta = 35 \pm 5$ meV and considering three dominant phonon energies, $\hbar\omega_1 = 8$ meV, $\hbar\omega_2 = 9.8$ meV and $\hbar\omega_3 = 17.4$ meV, identified via the non-resonant Raman measurements presented in Figure 5.6 (a). Although it appears that the multitude of variable fit parameters can compromise the robustness of the formalism, it must be noted that the well-defined spectral features impose strict tolerance limits over most of the fit parameters. For example, given the clear separation between the excitonic transition and continuum edge, the bandgap and binding energies can be directly *read-out* from the experimental data and are constrained during the fitting procedure. Similarly, well defined rising edges for the primary excitonic line and the continuum impart rigid conditions over the choice of broadening parameters. Finally, the normal-mode frequencies used in the vibronic progression are constrained to those extracted from the Raman spectra. Thus, the only effective free-fit parameters are the Huang-Rhys factors and the relative intensities of the four excitonic transitions (X_i/X_1). The complete set of parameters used to obtain the fits is listed in Table 5.1.

The binding energy remains relatively unperturbed by the temperature change, except for a minor reduction at higher temperatures ($\sim$ 5%). Although one would expect a contribution to the electronic polarization, and thus to the exciton binding energy, from the polar lattice vibrations that are activated at higher temperatures [11], the small exciton radius (associated with the large binding energy) makes the excitonic characteristics virtually immune to such fluctuations. The relative intensities of the excitonic states also show a moderate variance with temperature. While the third and fourth transitions, which are at the highest and lowest en-

Fit parameters for $(PEA)_2PbI_4$										
T (K)	E_g (eV)	E_b (meV)	$\frac{X_2}{X_1}$	$\frac{X_3}{X_1}$	$\frac{X_4}{X_1}$	S_1	S_2	S_3	Γ_c (meV)	Γ_{ex} (meV)
28	2.576	197.95	0.86	0.055	0.055	2.15	—	0.44	10.4	7.0
40	2.578	199.32	0.86	0.055	0.065	2.49	—	0.44	11.3	6.4
50	2.579	199.72	0.86	0.055	0.000	2.77	—	0.44	12.1	6.2
60	2.580	199.70	1.20	0.050	0.050	2.75	1.13	0.44	14.1	5.6
70	2.581	198.50	1.30	0.045	0.050	2.55	1.20	0.44	15.8	6.0
80	2.581	196.25	1.59	0.040	0.030	1.20	1.20	0.44	18.0	6.8
90	2.581	195.70	1.50	0.045	0.030	—	1.20	0.44	20.0	6.5
100	2.581	195.37	1.42	0.045	0.010	—	1.20	0.44	22.0	6.4

Table 5.1
Parameters used to fit the temperature dependent linear absorption spectra of $(PEA)_2PbI_4$ shown in Fig. 5.7, using the modified Eq. 1.20. The Huang-Rhys parameters S_i correspond to modes with energy 8 meV ($i = 1$), 9.8 meV ($i = 2$), and 17.4 meV ($i = 3$), extracted from the non-resonant Raman spectra (see Fig.5.6 (a)).

ergies relative to $E_g - E_b$, have low cross section with respect to X_1, the second transition (X_2) gains in relative intensity at higher temperatures.
The other fit variables are the Huang-Rhys factors, S_i, ($i = 1$ (8 meV), 2 (9.8 meV), 3 (17.4 meV)), listed in Table 5.1. For spectra below 60 K, only two modes at 8 and 17.4 meV contribute to the absorption. For a brief temperature range between 60 and 80 K, all three modes are required to reproduce the experimental lineshape. At 90 and 100 K, it is again sufficient to consider only two modes, but at 9.8 and 17.4 meV to fit the spectra. At higher temperatures (150 and 200 K in Fig. 5.7), the spectrum develops a strong asymmetric shoulder extending towards the continuum. Such a lineshape, which probably stems from the creation of shallow defect states, cannot be accounted for by the considered theoretical framework. An intriguing observation here is the weak temperature dependence of the exciton linewidth, at least within the probed temperature range. While the primary excitonic linewidth (X_1) fluctuates around 6.45 ± 0.53 meV, the free-carrier linewidth exhibits a clear temperature dependence that can be effectively explained by a carrier-LO phonon scattering mechanism [18]. Such a behavior, in spite of the Frank-Condon contributions to the absorption, suggests an anomalous nature of the exciton-phonon interactions.

Our absorption lineshape analysis is difficult at temperatures higher than the range shown in Fig. 5.7 due to the loss of spectral structure. In order to explore further the temperature dependence of the exciton linewidth, we have carried out temperature-dependent PL measurements. Figure 5.8 (a) shows the PL spectral different temperatures. The PL spectrum displays structure that is consistent with that identified in the absorption spectrum, namely distinct spectral features separated by ~ 35 meV. Although the integrated PL intensity is linear over a broad laser intensity range (Fig. 5.8 (d)), careful spectral analysis is complicated by the underlying contribution of biexcitons (see Fig. 5.8 (e) and next section). Nevertheless, we can extract the

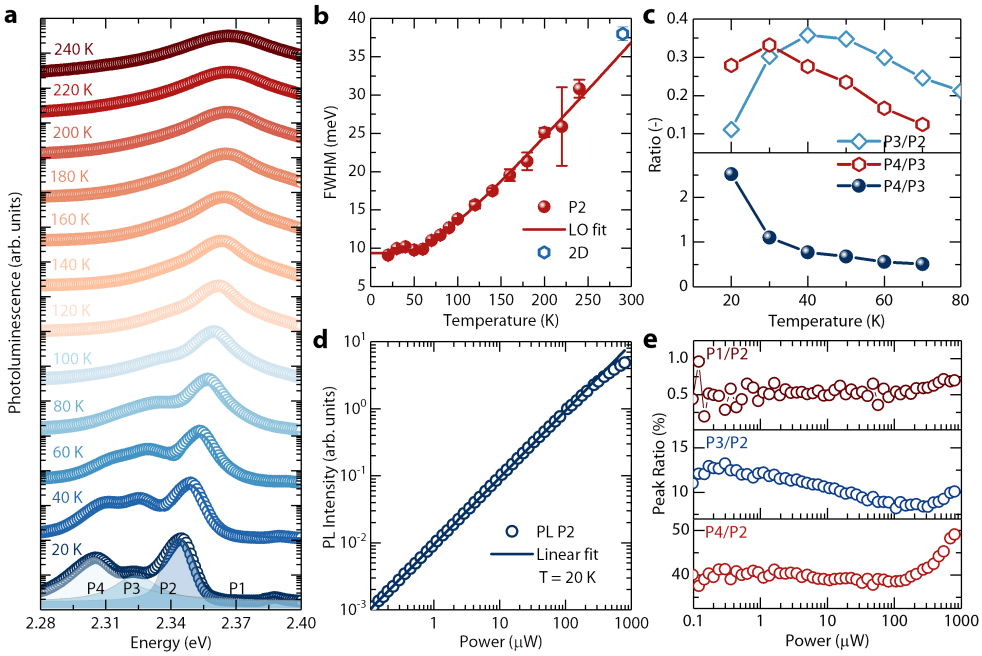

Figure 5.8
(a) PL spectra of polycrystalline films of $(PEA)_2PbI_4$ taken at different temperatures. **(b)** Full width at half maximum of the most intense PL peak as a function of temperature. **(c)** Ratio of intensities of various peaks plotted as a function of temperature. **(d)** Pump power dependence of the most intense PL peak at 20K. **(e)** Pump intensity dependence of the relative intensities of the peaks at 20 K.

full width at half maximum for the most intense peak as a function of temperature, shown in Figure 5.8 (b). We observe a clear temperature dependence over a range spanning up to room temperature with the trend indicating scattering from LO phonons[52] within the Fröhlich formalism (described by Eq. 1.42) The fit obtained using Equation 1.42 is shown in Figure 5.8 (b), with the temperature independent linewidth Γ_0 = 9.4 meV, the LO phonon energy E_{LO} = 17 meV and the exciton-phonon coupling parameter γ_{LO} = 25.6 meV. Intriguingly the extracted coupling parameter is much smaller than what has been reported for three dimensional hybrid perovskites. [18].

Let us consider the linewidths reported in Figure 5.8 (b) for PL measurement and Table 5.1 for absorption analysis, and consider to what extent they are due to inhomogeneous broadening mechanisms. Within linear spectroscopies, contributions from non-negligible inhomogeneous effects can hinder the direct measurement of the pure homogeneous linewidths that carry signatures of electron-phonon scattering. Non-linear spectroscopies, particularly two-dimensional coherent spectroscopies, offer an effective way to distinguish the homogeneous and inhomogeneous contributions [53]. The absolute value, zero-time rephasing spectra (obtained when the first pulse acts as a conjugate beam, compare methods chapter) of $(PEA)_2PbI_4$ polycrystalline films taken at room temperature is shown in Fig. 5.9 (a).

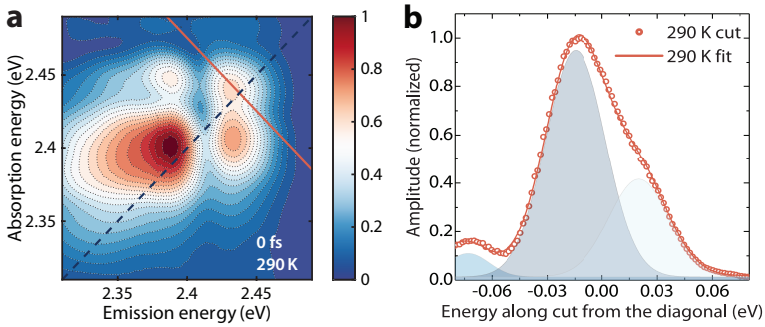

Figure 5.9
(a) Modulus of rephasing 2D spectrum of $(PEA)_2PbI_4$ taken at zero population time at room temperature. **(b)** Anti-diagonal cut taken along the line shown in the 2D maps plotted along with the Voigt profile fits.

This 2D spectrum shows rich spectral structure similar to that in the low temperature linear absorption spectra. The diagonal features correspond to the uncoupled excitations from the ground state to the excitonic states and the off-diagonal features are composed of contributions from inter-exciton correlations and transitions to higher lying biexcitonic states, as detailed in the next section. Of most relevance here is the specific spectral lineshape of the diagonal features at zero population time. It is well understood that the inhomogeneous contributions broaden the 2D rephasing spectra along the diagonal while the homogeneous rephasing effects are manifested along the anti-diagonal direction [54]. Figure 5.9 (b) shows anti-diagonal cuts along the line shown in the 2D spectra in Figure 5.9 (a) taken across a chosen peak on the diagonal with minimum overlap of off-diagonal features. The observed lineshape can be fitted using multiple Voigt functions (fits shown as solid lines in Fig. 5.9 (b)) yielding a linewidth of approximately 38 meV.
This homogeneous linewidth is similar to the total linewidth measured by PL at room temperature, suggesting that the observed exciton linewidths are dominated by homogeneous broadening effects. The corresponding dephasing times associated with the homogeneous linewidth at room temperature are ~ 138 fs, indicating the central importance of dynamic energetic disorder in this system (see next section).

Based on the empirical framework developed for $(PEA)_2PbI_4$, we now investigate the other 2D-HOIP systems, that we introduced in the first section. The absorption spectra of $(NBT)_2PbI_4$ films taken at various temperatures are shown in Figure 5.10 (a). Presented as solid lines in the same figure are the fits obtained using the extended Elliott model. Figure 5.10 (b) shows the spectrum taken at 20 K which includes the continuum contribution along with the fit thus substantiating the generality of the developed framework. The inter-exciton spacing considered here is again 35 ± 5 meV, similar to the case of $(PEA)PbI_4$ films. The relative intensities of the excitonic transitions follow a comparable trend. In addition, the linewidths of the free carrier states raise with temperature due to increased electron-phonon scattering while the

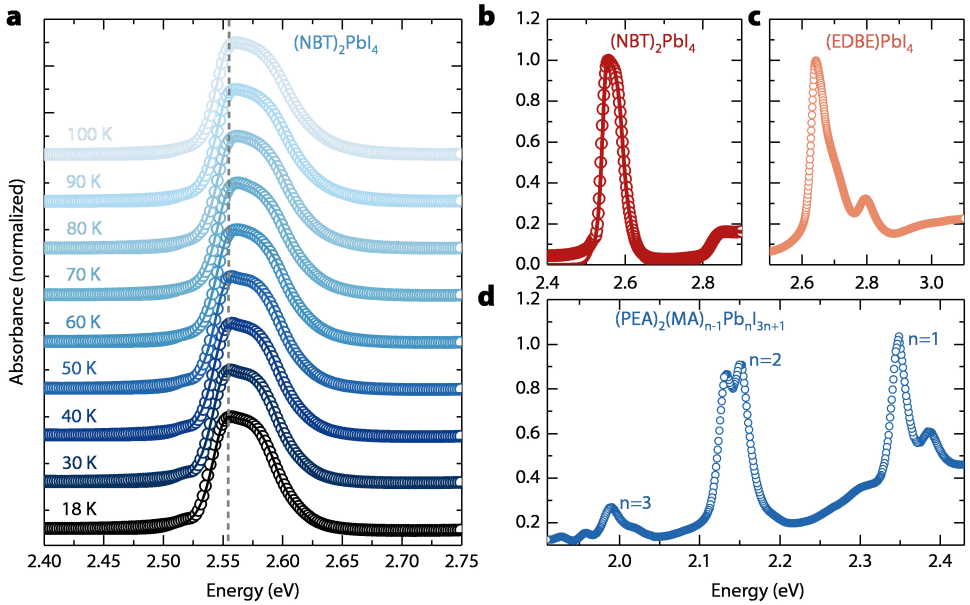

Figure 5.10
(a) Experimental absorbance spectra of polycrystalline films of $(NBT)_2PbI_4$ taken at different temperatures (plotted as symbols) and numerical fits (plotted as solid lines). **(b)** Experimental absorbance spectrum and numerical fit of $(NBT)_2PbI_4$ at 20 K showing both exciton and free carrier absorption. **(c)** Experimental absorbance spectrum of $(EDBE)PbI_4$ film taken at T=20 K. While the excitonic line shows fine structure, no clear band-edge is visible. **(d)** Low temperature absorbance spectrum of a polycrystalline film of $(PEA)_2(MA)_{n-1}Pb_nI_{3n+1}$.

excitonic linewidth remains approximately constant (see Table 5.2 for the complete list of fit parameters).

One of the pertinent differences with respect to the fits of $(PEA)_2PbI_4$ lie in the choice of the phonon energies used in the Franck-Condon analysis, which are set at 8.9 and 22 meV, the latter also appearing in the low-temperature PL spectra. The crystal structures of both films are very similar with regards to the PbI_6 connectivity, since they are both <100> oriented perovskites (see Fig. 5.1). However, the choice of the organic cation imposes different degrees of conformational constraint of the ammonium moieties and their interaction with the inorganic layer. This results in a variance in the extent of geometrical distortion of the lead-halide octahedra (compare first section [1]). In the present case, the $(NBT)_2PbI_4$ lattice exhibits greater octahedral distortion, and we hypothesize that this results in the increase in the energies of local lattice vibrations as can be seen in the change in the relevant vibrational frequencies. On the other hand, the re-organization energy of the excited state reduces as evidenced by the lower values for the Frank-Condon factors with respect to $(PEA)_2PbI_4$ (see Table 5.2).

The $(EDBE)PbI_4$ lattice exhibits larger octahedral distortion as we have seen in the first section. The absorption spectrum shown in Figure 5.10 (c) demonstrates that this not only modifies the

Fit parameters for $(NBT)_2PbI_4$									
T (K)	E_g (eV)	E_b (meV)	$\frac{X_2}{X_1}$	$\frac{X_3}{X_1}$	$\frac{X_4}{X_1}$	S_1	S_2	Γ_c (meV)	Γ_{ex} (meV)
20	2.818	253.40	0.89	0.004	0.190	1.4	0.70	12.5	9.5
30	2.819	253.37	0.97	0.027	0.215	1.4	0.70	13.2	9.6
40	2.820	253.35	0.99	0.025	0.220	1.4	0.70	13.8	9.6
50	2.821	253.65	1.00	0.025	0.220	1.4	0.70	14.0	9.5
60	2.823	253.53	1.02	0.025	0.220	1.4	0.70	14.8	9.7
70	2.824	253.35	1.05	0.025	0.230	1.4	0.70	15.6	9.8
80	2.824	253.28	1.13	0.01	0.230	1.4	0.70	16.4	9.7
90	2.824	253.53	1.20	0.01	0.240	1.4	0.69	17.2	9.7
100	2.824	253.65	1.25	0.01	0.240	1.4	0.69	17.6	9.7

Table 5.2
Parameters used to fit the temperature dependent linear absorption spectra of $(NBT)_2PbI_4$ shown in Fig. 5.10, using the modified Eq. 1.20. The Huang-Rhys parameters S_i correspond to modes with energy 8.9 meV (i = 1) and 22 meV (i = 2).

phonon landscape, but also increases the inter-exciton spacing. It can also be seen that there is no clear and distinct band-edge even at very low temperatures, suggesting a breakdown of the Wannier-like scenario. In fact, it is not possible to reproduce such a spectral structure in a robust way with the considered framework, pointing to a much higher degree of localization of both excitons and free-carriers induced by the large structural deformation. In spite of such strong localization, the presence of the exciton fine structure, albeit with larger energy spacing, indicates the role of lattice structure in their origin.
Similar spectral structure is also observed when the layer thickness is increased, as shown in Fig. 5.10 (d). Here, we investigate multi-layered films by introducing methylammonium ($CH_3NH_3^+$) cations to form $(PEA)_2(CH_3NH_3)_{n-1}Pb_nI_{3n+1}$ films, which contain n sheets of PbI_6 layers. Being grown from solution, such a film consists of polycrystalline grains with a varying number of connected PbI_6 layers between the organic barriers [55]. Absorption stemming from regions with different layer thickness can be clearly distinguished in the absorption spectrum shown in Figure 5.10 (d) due to the reducing bandgap with increasing number of layers. In particular, we identify excitonic peaks associated with 1 to 3 layer components and all of them exhibit a clear fine structure, albeit with variable relative intensities. While this observation re-iterates the importance of lattice structure, it also suggests that such a excitonic sub-structure may be intrinsic to the perovskite lattice and not just a consequence of confinement.

5.4.2 Discussion

We developed a quantitative framework to rationalize spectral lineshapes observed in the linear spectra in different 2D HOIPs. Albeit the formalism reproduces the spectra of systems

with no strong octahedral distortion, it is not sufficient for highly distorted lattices. More importantly we have identified various manifestations of electron-phonon coupling in the optical spectra, the most obvious being the phonon replicas. Different lattice degrees of freedom associated to both crystal phonons and local vibrations contribute to these lineshapes with varying Huang-Rhys factors.

Phonon replicas are not uncommon in the optical spectra of semiconductors with non-negligible electron-phonon interactions [56]. Interestingly, most of the reported replicas in inorganic semiconductors have been observed exclusively in the PL spectra and have been explained based on a phonon-assisted emission processes involving Fröhlich-like electron scattering with the polar lattice vibrations [56–59]. On the other hand, such signatures are clearly observed even in the absorption spectra of organic semiconductors [60], similar to the current scenario, and discussed as a consequence of the distinct lattice configuration of the excited electronic state. Some of us have recently demonstrated in the case of 3D perovskites that the excited photoexcitation indeed perceives a distinct lattice configuration [61] similar to molecular systems involving Frenkel states. Our observation here of the phonon replicas with large Huang-Rhys factors also suggests a similar scenario even in the case of 2D perovskites. We consider that deeper and more quantitative understanding is required to expand on this concept.

While all the three dominant Raman modes appear to be contributing to the observed phonon replicas, only one of them contributes strongly to the line broadening, as evidenced by the weak temperature dependence of the exciton linewidth in the absorption spectrum as well as the clear temperature dependence of the PL spectral width, shown in Fig. 5.8 (b). This can be understood by revealing the distinct mechanisms leading to broadening and the phonon replicas, although both of them involve exciton-phonon coupling. As proposed by Hochstrasser and Prasad [62] in the context of Frenkel excitons in molecular crystals or by Duke and Mahan [57] in the context of bound excitons associated to defect centers in inorganic lattices, the exciton-phonon coupling can be elaborated as:

$$H(\vec{r}) = H_{ex}(\vec{r}_0) + H_M(\vec{r}) + H_D(\vec{r}), \tag{5.3}$$

where H_D and H_M are the coordinate-dependent terms describing the exciton-phonon interactions in the vibrating lattice, and are composed of interaction energies that arise from the following distinct physical phenomena. H_M represents an exciton scattering with a phonon and is described by the excitation exchange interactions M_{nm} between two lattice sites m and n. Such a mechanism leads to the broadening of the excitonic transition in the optical spectra. On the other hand, H_D describes the energy required to displace the equilibrium lattice configuration in order to accommodate the photoexcitation. In other words, it is the lattice recoil (or deformation) energy which generates lattice vibrations at the site of the photoexcitation. As pointed out earlier, such a reconfiguration of the lattice manifests as strong vibronic replicas in the optical spectra.

Such a Frenkel-like perspective, however, contradicts the considered Wannier formalism described in Equation1.20. Given that the estimated exciton Rydberg energy ($R_y^* = E_b/4$) from the fits is around 50 meV implying a Bohr radius ($a_0 = e^2/\left(4\varepsilon_r\varepsilon_0 R_y^*\right)$) of approximately 12 nm (assuming $1/\varepsilon_r = 1/\varepsilon_\infty - 1/\varepsilon_s$ and $\varepsilon_\infty = 5$ and $\varepsilon_s = 15$) [63], the exciton is far from the Frenkel

limit when the exciton size is smaller than the lattice constant [64]. At the same time, such a treatment is necessary to account for the observed phonon replicas. This apparent inconsistency only highlights the limitation of both Wannier and Frenkel limits for these systems and calls for the development for more comprehensive treatment, especially with regards to exciton-phonon coupling.

With this discrepancy in mind, for molecular systems, the inequality $H_D >> H_M$ holds true due to the substantial localization of the Frenkel excitons which deform the lattice locally. In inorganic systems, the other extreme limit of exciton-phonon interaction is observed, termed as the weak coupling limit by Davydov [60], where $H_D << H_M$ and the excitons are delocalized. Based on the analysis of the 2D perovskites presented here, we suggest that we are in the intermediate limit where both localized and delocalized effects manifest albeit in distinct physical observables. For example, the large Huang-Rhys factors of the low energy phonon modes (at 8 meV for $(PEA)_2PbI_4$ films and 8.9 meV for $(NBT)_2PbI_4$ films) suggests their dominant role in the local lattice re-organization. At the same time, there is a well defined reciprocal lattice where the delocalized excitons scatter or a particular lattice phonon (17 meV and 22 meV for $(PEA)_2PbI_4$ and $(NBT)_2PbI_4$ respectively). For a more rigorous discussion there is a need for a robust assignment of the resonance Raman modes to specific lattice symmetries, which will be addressed in future work.

Another important observation is the presence of distinct transitions around the primary exciton line separated by around 35 ± 5 meV. As noted earlier, this separation energy does not correspond to any vibrational energy, at least to our knowledge, and thus cannot be considered as a simple vibronic progression. We consider them to originate from excitons with renormalized binding energies. We discuss a few mechanisms which can lead to such a renormalization. Polaronic effects have been considered extensively to explain the carrier transport and recombination dynamics in 3D perovskites. The polaron coupling coefficient, a measure of electron-phonon coupling assuming a Fröhlich interaction, is given as [65],

$$\alpha = \frac{e^2}{\hbar}\frac{1}{4\pi\varepsilon_0}\sqrt{\frac{m^*}{2\hbar\omega_{LO}}}\left[\frac{1}{\varepsilon_\infty} - \frac{1}{\varepsilon_s}\right]. \tag{5.4}$$

Considering a carrier effective mass m^* of $0.2m_0$ [49] and the LO phonon energy to be 17.4 meV, following the linewidth analysis of $(PEA)_2PbI_4$ films, we obtain a coupling constant of $\alpha = 1.69$ assuming $\varepsilon_s = 15$. Although there is no direct experimental measurement of the static dielectric permittivity, the maximum value is set by that of 3D perovskites ($\varepsilon_s = 35$) [63], considering which we obtain $\alpha = 2.2$. An estimate of the polaron binding energy (E_p) can be evaluated within a perturbative approach as [66],

$$E_p = -\hbar\omega_{LO}\left[\alpha + 0.0158\alpha^2 + 0.00081\alpha^3\right]. \tag{5.5}$$

Using the calculated value of α in Equation 5.5 gives a polaron energy between approximately 29.6 meV and 39 meV, very close to the observed inter-exciton spacing Δ. Thus, one may hypothesize that the multiple transitions are a consequence of polaronic effects in these systems [67, 68], as also suggested by Gauthron *et al.* [69]. The mechanism which stabilizes distinct

transitions instead of a single renormalized exciton, on the other hand, may lie in the lattice symmetry arguments driven by phonons with the interaction energy given by the polaron energy (E_p). It is worth noting that the system here is not strictly 2D, unlike transition-metal dichalcogenides, with a non-trivial extension of the carrier wavefunctions in the z-direction, perpendicular to the lattice plane. Any phonon driven distortions of the octahedra may lift hidden orbital degeneracies giving rise to the multiple transitions [70]. More systematic investigation of this process requires rigorous group theoretical analysis of the lattice in conjunction with the vibrational degrees of freedom.
Alternatively, the degeneracy lifting can also be driven by the large spin-orbit coupling (SOC) due to the presence of lead, which can result in Rashba-Dresselhaus effect [71] when coupled with the asymmetry intrinsic to the 2D HOIP lattice. Briefly, lack of symmetry creates a gradient in the crystal potential and thus a local electric field. An electron in the lattice will be accelerated by such a field, inducing a magnetic field in its frame of reference. Thus, even in the absence of external magnetic field, and merely by virtue of the SOC field, spin degeneracies will be lifted, splitting the carrier bands. In the case of stable-exciton states such an effect can lead to the mixing of singlet and triplet states and the lifting of associated degeneracy, perceived via excitonic signatures in optical absorption. In fact, Zhai *et al.* report a Rashba splitting of 40 meV in $(PEA)_2PbI_4$ [72], consistent with the observed energy spacing. Such a mechanism, on the other hand, must be very sensitive to the thickness of the metal-halide layer, which determines the strength of the crystal potential. As we do not observe a substantial change in the inter-exciton spacing as can be seen in the absorption spectrum of a multi-layered 2D-HOIP film shown in Figure 5.10(d), we deem this to be an unlikely mechanism for the fine-structuring of the exciton.

5.4.3 Conclusions 2

By means of temperature-dependent linear absorption measurements and modeling with a simple two-dimensional Wannier exciton formalism, supported by two-dimensional coherent excitation spectroscopy, we have identified excitation spectral lineshapes that are consistent with polaronic effects on the exciton. This is reflective of the highly polar nature of the lattice in this class of materials, as well as its hybrid organic-inorganic nature, in which delocalized phonons as well as more localized vibrations couple to the electronic degrees of freedom on the lead-halide single plane. Excitons in these complex quantum-well-like structures are well described by a Wannier model, appropriate for excitons in quantum-confined semiconductor materials, but also show signatures of strong lattice deformation effects induced by the photoexcitation itself, which are not generally manifested in common semiconductor nanostructures. We consider that understanding the intricate details of exciton-lattice coupling dynamics in 2D metal-halide perovskites will uncover a wealth of information on their electronic and optical properties.

5.5 The role of crystal structure in the excitonic many-body effects of $(PEA)_2PbI_4$

Considering their synthesis, 2D HOIPs constitute an easily accessible material to investigate low-dimensional many body physics, promising for applications in quantum optoelectronics. In this context, it is essential to comprehensively study all factors - electronic, chemical and structural - that determine and influence strong multi-exciton correlations. We have seen that the electro-optical properties of 2D HOIPs are sensitive to the organic-inorganic lattice interactions. In the following we will address the question if excitonic correlations in the material can sustain stable biexcitons at room temperature despite the complex nature of dynamic disorder. This question is of fundamental importance to understand the role of biexcitons in the photophysics of a material, e. g. relevant for lasing [73].
Bound exciton pairs in two-dimensional HOIPs have been discussed in previous reports [74–78]. Ishihara *et al.* [74] gave an estimate of ~ 50 meV for the biexciton binding energy (with respect to two unbound excitons) by analyzing the evolution of the PL spectrum with excitation density at low temperatures. Kondo *et al.* suggested biexcitonic lasing in a 2D HOIP [75] and Kato *et al.* [76] reported comparably large biexciton binding energies in a related 2D perovskite as reported by Ishihara *et al.*, based on multiphoton absorption and PL measurements. These findings were consistent with a later report by Fujisawa *et al.* on bismuth-doped lead-halide perovskites [77]. Recently, Elkins *et al.* demonstrated strong many-body interactions in multi-layered HOIPs, using two-quantum 2D coherent spectroscopy [78].
Here we investigate the excitonic correlations in the prototypical single-layer 2D perovskite $(PEA)_2PbI_4$ introduced in the previous section. Changing the temperature, as we have seen, allows us to control the degree of dynamic disorder in the material and to observe its influence on biexciton screening. Direct extraction of the biexciton binding energy via PL line-shape analysis can lead to questionable results due to temperature dependent linewidth broadening effects. Here, we employ two-dimensional coherent excitation spectroscopy [79] to unambiguously determine the biexciton binding energy of a single-layer perovskite quantum well structure, that turns out to be comparable to calculated [80] and measured [79] values from other strongly excitonic 2D semiconductors such as the transition-metal dichalcogenides. In the following, we will demonstrate that biexciton binding energies in 2D HOIPs are considerably affected by dynamic disorder due to both, local lattice vibrations induced by the organic constituent and optical phonons. This interaction has important implications for the understanding of electronic correlations in these materials, and can serve as benchmark to develop a detailed theoretical framework to treat their many-body physics.

5.5.1 Results

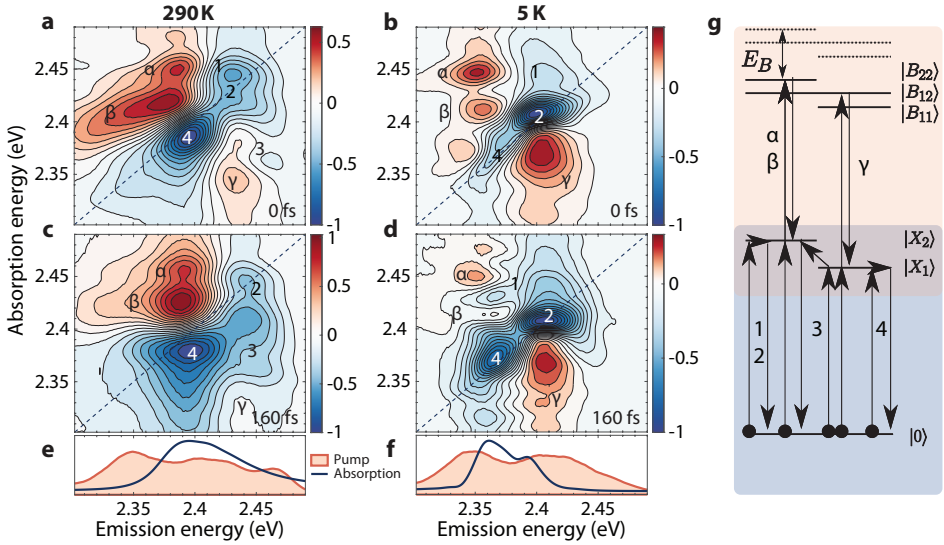

Figure 5.11
1Q total correlation spectra of $(PEA)_2PbI_4$ at room temperature **(a)**,**(c)** and 5 K **(b)**,**(d)** for the two population times 0 fs **(a)**,**(b)** and 160 fs **(c)**,**(d)**. The linear absorption and pump laser spectra for the monitored range are shown in **(e)** and **(f)**. The level scheme in **(g)** represents some of the coherent processes involved in the visible spectral features. Note, that transitions within the same exciton manifold have been drawn as degenerate to avoid a crowded diagram (adapted from [2]).

We have seen in the previous section that the change in order parameter of $(PEA)_2PbI_4$ renormalizes the exciton binding energy by about 10 meV (compare gray arrow in Fig. 5.6 (c)). Although this corresponds to a correction of less than 5% and indicates, that the intrinsic electron-hole interactions are not strongly perturbed by lattice fluctuations, we saw that there are non-trivial corrections in exciton-phonon coupling leading to the observed evolution of the exciton fine structure. They can have a significant effect on bound multi-excitons, which exhibit usually much smaller binding energies as suggested in earlier photoluminescence studies [74]. To investigate the impact of lattice fluctuations on many-exciton correlations we require a technique, which goes beyond steady-state PL and linear absorption and allows us to directly identify multi-quantum resonances, the spectral fingerprints of exciton-exciton correlations. Therefore, we employ two-dimensional coherent spectroscopy at 5 K and room temperature, to access the two extremes at opposite ends of the scale of dynamic disorder.

One-quantum (1Q) measurements

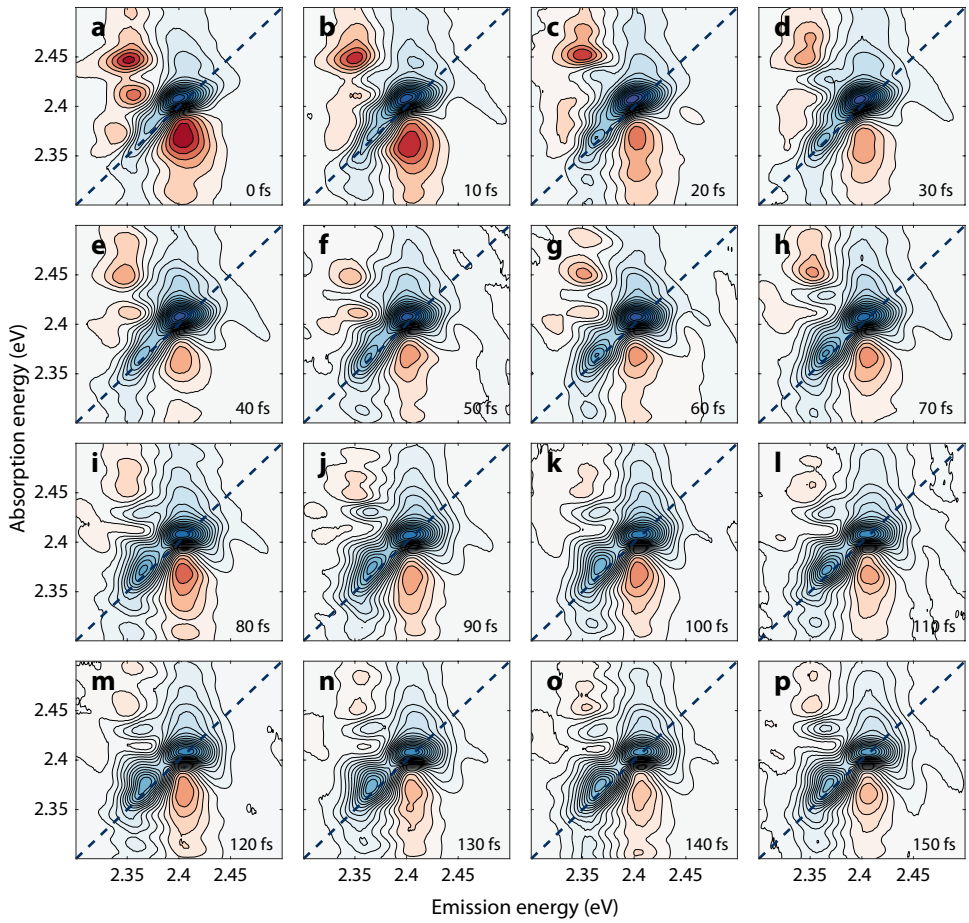

Figure 5.12
Spectral evolution of the 1Q total correlation maps of $(PEA)_2PbI_4$ over time till 150 fs at 5 K (adapted from [2]).

Figure 5.11 shows the 1Q total correlation spectra for $(PEA)_2PbI_4$ at room temperature (a),(c) and 5 K (b),(d) and two different population times (0 and 160 fs). The relative strength of the observed spectral features are weighted by the product of pump and absorption spectra, which are given in Figure 5.11 (e) and (f) for comparison. All spectra exhibit negative features along the diagonal (peaks 2 and 4) and off-diagonal crosspeaks (peaks 1 and 3) which can be assigned to the primary transitions between ground and excitonic states. Additionally, large positive features are visible (labeled α, β, and γ) indicating a non-trivial excited-state manifold from single-quantum to energetically higher-lying states. These features are partially overlapping with the negative cross-peaks, thereby obscuring their true line-shapes. However,

we can compare their position with respect to the emission axis to the upper cross-peak (1) and the diagonal feature (2) to give an estimate of the energy of the second excited-state manifold. The ESA signatures α and β imply the existence of a state energetically 55 ± 2 meV and 42 ± 2 meV below twice the energy of the excitonic transition for 5 K and room temperature respectively. Assuming that this excited state corresponds to a correlated two-electron, two-hole quasi-particle, a biexciton, the above energy difference gives an estimate of the biexciton binding energy E_B.[3]

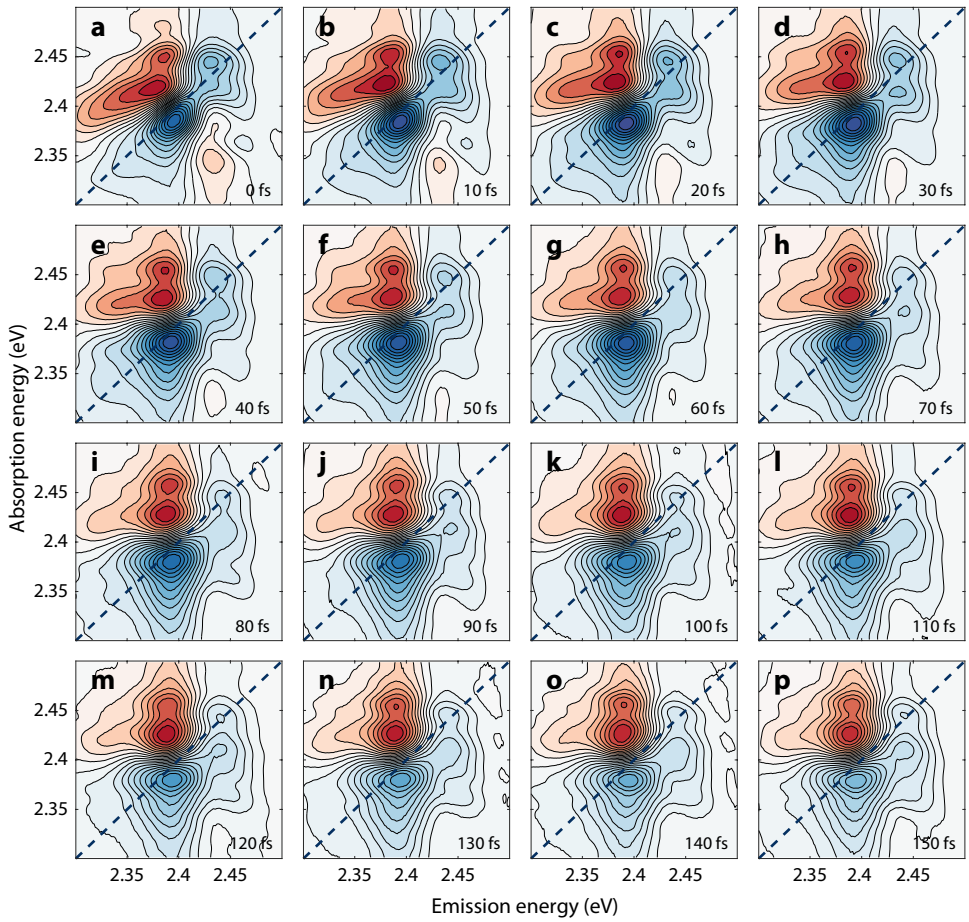

Figure 5.13
Spectral evolution of the 1Q total correlation maps of $(PEA)_2PbI_4$ over time till 150 fs at room temperature (adapted from [2]).

Figure 5.12 presents the spectral evolution of the 1Q maps at 5 K over time, showing the relax-

[3]Note, that the positive feature γ in the right lower corner could also be a biexciton signature, nevertheless, the strong interference with the underlying negative feature in this case renders an estimate of the corresponding binding energy vague.

ation between the excitonic states. It can be seen, that within 100 fs, the spectral weight of the higher energy feature is transferred to the lower-energy resonance by means of population relaxation. Simultaneously, the correlated cross peaks with this transitions gain in intensity and start to partially dominate the overlaying positive ESA signatures. In contrast, room temperature measurements (Fig. 5.13) reveal a monotonic decay in intensity over the entire spectrum and do not show such dominant relaxation dynamics. We presume that thermal disorder not only broadens the excitonic transitions, leading to a lack of spectral structure, but also stabilizes the population distribution within the excited-state manifold. Consequently, within the probed temporal window, we do not observe substantial relaxation. However, the dynamics show that the spectral line-shape, elongated along the diagonal at initial times broadens in anti-diagonal direction within tens of femtoseconds. This trend suggests the re-distribution of energy between inhomogeneously broadened oscillators and the surrounding environment via incoherent interactions, a phenomenon known as spectral diffusion [81]. Nevertheless, the observed dynamics require a more detailed analysis, despite of being compellingly similar to the timescales of ultrafast lattice reorganization, observed in three-dimensional hybrid perovskites [61].

Two-quantum (2Q) measurements

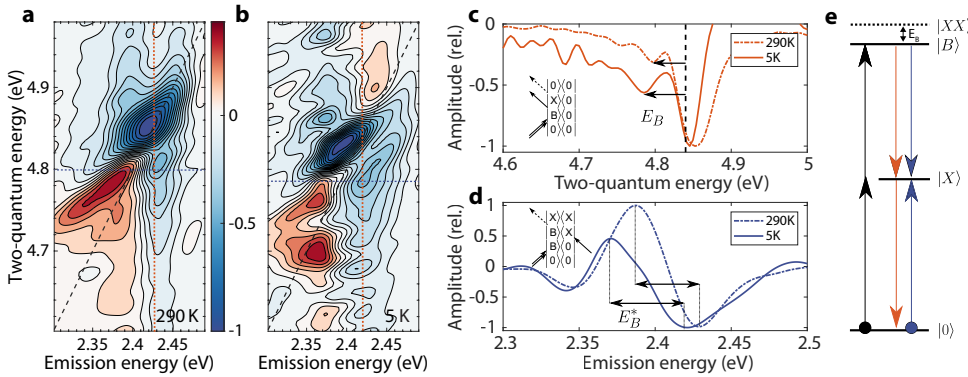

Figure 5.14
Real part of 2Q non-rephasing measurements of $(PEA)_2PbI_4$ at room temperature **(a)** and 5 K **(b)** for a 1Q waiting time of 20 fs. The dashed diagonal lines accentuate the two-quantum energies corresponding to twice the emission energy. Selective cuts along the dashed colored lines in **(a)** and **(b)** are shown in **(c)** and **(d)**, the dashed line in **(c)** indicates the crossing point between cut axis and diagonal. Horizontal cuts were taken at the energies corresponding to the biexcitonic feature on the vertical axis. The insets of **(c)** and **(d)** indicate the Feynman pathways responsible for the spectral position of the biexciton features. $|X\rangle$ and $|B\rangle$ denote the exciton and biexciton states. E_B and E_B^* can be read out from the shifts from the diagonal and the bound biexciton coherences respectively. **(e)** illustrates the coherent pathways indicated by the Feynman diagrams (adapted from [2]).

Although the ESA features allow for a first estimate of the biexciton binding energy, their convolution with the cross-peaks adds ambiguity to the retrieved value. Therefore, we performed

2Q experiments, to selectively probe the higher-lying excited states. 2Q measurements have been used to probe many-body interactions in various systems as e.g. GaAs quantum wells [82], monolayers of transition-metal dichalcogenides [83], semiconductor quantum dots [84] and multi-layered two-dimensional perovskites [78].
The real part of the non-rephasing 2Q spectra $(PEA)_2PbI_4$ for room temperature and 5 K is shown in Figure 5.14 together with the energy scheme depicting the levels of excitons $|X\rangle$ and biexcitons $|B\rangle$ and unbound correlated pairs (dashed states). To minimize possible contributions from undesired FWM signals while keeping a high signal to noise ratio (SNR), the 1Q waiting time between the first two pulses is set to 20 fs (FWHM of temporal pulse profile). Both spectra exhibit strong dispersive line-shapes on the two-quantum diagonal axis ($\omega_{2Q} = 2\omega_{emit}$), arising from unbound but correlated excitons due to many-body interactions, including excitation induced dephasing and excitation induced shift [85]. Features along the diagonal axis correspond to correlations without any attractive or repulsive contributions, whereas peaks above or below indicate bound exciton pairs of similar and different species respectively [86]. Signatures slightly below the diagonal arise from oscillating coherences between ground and 2 quantum states and their vertical shift gives a measure of the biexciton binding energy, yielding $E_B = 44 \pm 5$ and $E_B = 55 \pm 5$ meV for room temperature and 5 K respectively. This values conform to the estimate we retrieved from the 1Q measurements, suggesting that the positive features observed previously arise from excited-state absorption into a bound exciton-pair. Note, that this is the first direct measurement of biexcitons in a monolayered two-dimensional perovskite.

According to theory and the second quantum pathway depicted in Figure 5.14 (d) and (e) a positive feature shifted by the binding energy along the emission axis towards lower energies should be visible, due to coherences between a two quantum and single-exciton state [87]. The peak can be observed along a horizontal cut at the two-quantum energy of the negative biexcitonic feature and yields another estimate of the binding energy E_B^*. From the energetic difference between the two extrema we can extract $E_B^* = 42 \pm 5$ and $E_B^* = 50 \pm 5$ meV for room temperature and 5 K respectively, confirming our previous values.

Estimates of the biexciton binding energy are often retrieved from PL measurements, as has been done by Ishihara *et al.* [74]. In the previous section we discussed that the emission feature, energetically red-shifted by about 40 meV from the primary excitonic emission peak, exhibits overlapping spectral contributions from the excitonic fine-structure. Considering also effects of re-absorption due to small Stokes shifts this can result in an under-estimate of the binding energy. Moreover, the high pump powers required to identify the spectral signatures of biexcitons in PL spectra can heat up the sample and possibly degrade the material, thus resulting in unreliable estimates. Furthermore, a non-linear increase in the photoluminescence intensity with excitation density can arise also due to defect-related effects as we have seen in Chapter 3. At room temperature, the PL spectrum of $(PEA)_2PbI_4$ is broadened and featureless which makes it impossible to identify spectral signatures from biexcitons. These drawbacks of regular PL measurements highlight the advantage of 2D coherent spectroscopy employed here.

5.5.2 Discussion

In summary, we used 1Q and 2Q coherent multidimensional spectroscopy to directly observe biexcitons in single-layered $(PEA)_2PbI_4$. Our measured binding energies agree well with the values of previous reports by Ishihara *et al.* [74] and are close to those of other two-dimensional systems of technological interest like the transition metal dichalcogenides [79, 83]. It is essential, that biexcitons in 2D perovskites are similarly stable as in purely covalent low-dimensional semiconductors, despite of strong dynamic disorder due to the ionic and hybrid nature of the crystal structure. Our temperature-dependent investigation using 2Q measurements reveals a similar effect of temperature as observed for the exciton binding energy. The strong renormalization of the biexciton binding energy implies significant contributions of the lattice to the dielectric function and therefore Coulomb screening effects in two-dimensional perovskites.
The effect of lattice vibrations in excitonic polar crystals has been taken into account by an effective permettivity function, composed of the different frequency responses, as demonstrated by Pollmann-Buttner [88] and Kane [89]. This concept has been extended to the case of three-dimensional hybrid perovskites and it has been shown experimentally [90] and theoretically [4] that the motion of the organic cation can screen electron-hole correlations.[4] In contrast, dielectric confinement assures large exciton binding energies and small Bohr radii in two-dimensional perovskites. Therefore, the effect of lattice fluctuations remains relatively small, as can be seen by the moderate correction to the exciton binding energy upon lowering the temperature. Moreover, the spectral structure in the non-linear (1Q) spectra is similar comparing the two temperature extremes. On the other hand, the observed change in biexciton binding energy suggests dynamic disorder to be a crucial parameter in many-body-correlations, especially at high excitation densities ($> 10^{18}$ cm^{-3}).
Interestingly, the biexciton binding energy in 2D perovskites belongs to the highest of all semiconducting systems investigated to far [80]. Consequently, biexcitons will form the dominant photoexcitation at high excitation densities, and can constitute an important non-radiative loss channel for the exciton population. It is expected, that an Auger-like channel plays a dominant role in lasing devices by raising the thresholds for population inversion [73]. Therefore, the effect of dynamic disorder could be employed to optimize an appropriate material. If biexcitons form the emissive species in lasing action as proposed by Kondo *et al.* [75], the material should be optimized to house stable biexcitons.

[4] Due to the small exciton binding energies in 3D perovskites, this effect does not affect substantially the excitation dynamics, since free carriers are predominant after photo-excitation.

5.5.3 Conclusions 3

In summary, we demonstrate that biexcitons in $(PEA)_2PbI_4$, a single-layer two-dimensional hybrid semiconductor, form the primary photoexcitation at high excitation densities ($> 10^{18}$ cm^{-3}), although hybrid perovskites constitute energetically highly disordered systems. Lattice dynamics lead to renormalization of the exciton binding energy and have substantial impact on the binding energies of correlated electron-hole pairs. Using two-dimensional coherent spectroscopy, we measure at 5 K an increase in biexciton binding energy of 25% in comparison to room temperature. Nevertheless, an ambient value of 44 meV is sufficiently high to support stable biexcitons and only ~ 10% of the population would dissociate under steady-state conditions. This points to the importance of understanding the role of chemical and crystalline structure on many-body correlations. In the future, multi-dimensional coherent spectroscopy should be used as tool to systematically study many-body correlations in systems with increasing octahedral distortion (compare first section of this chapter) with the aim, to elaborate the parameter space allowing to control and fine-tune the degree of disorder by means of the employed organic templating cation. Multi-particle correlations are the basis of quantum phase transitions in semiconductors — Bose-Einstein condensation [91] and exciton-Mott transitions, which are the main mechanisms for polaritonic and photonic lasing, respectively. Elaborating and conceptualizing the effect of dynamic disorder on the induced co-operative behavior of the coherent electronic excitations upon phase transition is of technological significance and constitutes a new frontier for the physics of highly disordered excitonic semiconductors.

References

[1] D. Cortecchia et al. "Broadband Emission in Two-Dimensional Hybrid Perovskites: The Role of Structural Deformation". In: *J. Am. Chem. Soc* 139.1 (2017), pp. 39–42.

[2] F. Thouin et al. "Stable biexcitons in two-dimensional metal-halide perovskites with strong dynamic lattice disorder". In: *arXiv preprint arXiv:1712.04733* (2017).

[3] B. Saparov and D. B. Mitzi. "Organic–inorganic perovskites: structural versatility for functional materials design". In: *Chem. Rev.* 116.7 (2016), pp. 4558–4596.

[4] J. Even, L. Pedesseau, and C. Katan. "Analysis of multivalley and multibandgap absorption and enhancement of free carriers related to exciton screening in hybrid perovskites". In: *The Journal of Physical Chemistry C* 118.22 (2014), pp. 11566–11572.

[5] J. Even, L. Pedesseau, and C. Katan. "Understanding quantum confinement of charge carriers in layered 2D hybrid perovskites". In: *ChemPhysChem* 15.17 (2014), pp. 3733–3741.

[6] T. Ishihara, J. Takahashi, and T. Goto. "Exciton state in two-dimensional perovskite semiconductor $(C_{10}H_{21}NH_3)_2PbI_4$". In: *Solid State Commun.* 69.9 (1989), pp. 933–936.

[7] G. Bastard et al. "Exciton binding energy in quantum wells". In: *Phys. Rev. B* 26.4 (1982), pp. 1974–1979.

[8] H. Haug and S. W. Koch. *Quantum theory of the optical and electronic properties of semiconductors*. World Scientific, 1990.

[9] J. Maan et al. "Magneto-optical determination of exciton binding energy in GaAs-$Ga_{1-x}Al_x$As quantum wells". In: *Phys. Rev. B* 30.4 (1984), pp. 2253–2256.

[10] K. Miyata, T. L. Atallah, and X. Zhu. "Lead halide perovskites: Crystal-liquid duality, phonon glass electron crystals, and large polaron formation". In: *Sci. Adv.* 3.10 (2017), e1701469.

[11] J. Even et al. "Solid-state physics perspective on hybrid perovskite semiconductors". In: *The Journal of Physical Chemistry C* 119.19 (2015), pp. 10161–10177.

[12] O. Yaffe et al. "Excitons in ultrathin organic-inorganic perovskite crystals". In: *Physical Review B* 92.4 (2015), p. 045414.

[13] L. Pedesseau et al. "Advances and Promises of Layered Halide Hybrid Perovskite Semiconductors". In: *ACS Nano* 10.11 (2016), pp. 9776–9786.

[14] D. A. Egger, A. M. Rappe, and L. Kronik. "Hybrid organic–inorganic perovskites on the move". In: *Accounts of chemical research* 49.3 (2016), pp. 573–581.

[15] A. M. Leguy et al. "Dynamic disorder, phonon lifetimes, and the assignment of modes to the vibrational spectra of methylammonium lead halide perovskites". In: *Physical Chemistry Chemical Physics* 18.39 (2016), pp. 27051–27066.

[16] K. Hattori. "Exciton Binding Energies in Polar Crystals". In: *Physica Status Solidi (B)* 76.1 (1976), pp. 281–287.

[17] X. Wu et al. "Light-induced picosecond rotational disordering of the inorganic sublattice in hybrid perovskites". In: *Science advances* 3.7 (2017), e1602388.

[18] A. D. Wright et al. "Electron–phonon coupling in hybrid lead halide perovskites". In: *Nature communications* 7 (2016).

[19] J. Calabrese et al. "Preparation and characterization of layered lead halide compounds". In: *Journal of the American Chemical Society* 113.6 (1991), pp. 2328–2330.

[20] E. R. Dohner et al. "Intrinsic white-light emission from layered hybrid perovskites". In: *Journal of the American Chemical Society* 136.38 (2014), pp. 13154–13157.

[21] E. R. Dohner, E. T. Hoke, and H. I. Karunadasa. "Self-assembly of broadband white-light emitters". In: *Journal of the American Chemical Society* 136.5 (2014), pp. 1718–1721.

[22] Y. Li et al. "Novel <110>-Oriented Organic-Inorganic Perovskite Compound Stabilized by N-(3-Aminopropyl)imidazole with Improved Optical Properties". In: *Chemistry of materials* 18.15 (2006), pp. 3463–3469.

[23] A. Yangui et al. "Optical investigation of broadband white-light emission in self-assembled organic-inorganic perovskite $(C_6H_{11}NH_3)_2PbBr_4$". In: *The Journal of Physical Chemistry C* 119.41 (2015), pp. 23638–23647.

[24] T. Hu et al. "Mechanism for broadband white-light emission from two-dimensional (110) hybrid perovskites". In: *The journal of physical chemistry letters* 7.12 (2016), pp. 2258–2263.

[25] D. Cortecchia et al. "Polaron self-localization in white-light emitting hybrid perovskites". In: *Journal of Materials Chemistry C* 5.11 (2017), pp. 2771–2780.

[26] I. Pelant and J. Valenta. *Luminescence spectroscopy of semiconductors*. Oxford University Press, 2012.

[27] A. Herklotz et al. "Controlling octahedral rotations in a perovskite via strain doping". In: *Scientific reports* 6 (2016), p. 26491.

[28] J. Teixeira-Dias et al. "Conformational studies by Raman spectroscopy and statistical analysis of gauche interactions in n-butylamine". In: *Spectrochimica Acta Part A: Molecular Spectroscopy* 42.5 (1986), pp. 589–597.

[29] C. Quarti et al. "The Raman spectrum of the $CH_3NH_3PbI_3$ hybrid perovskite: interplay of theory and experiment". In: *The journal of physical chemistry letters* 5.2 (2013), pp. 279–284.

[30] F. Brivio et al. "Lattice dynamics and vibrational spectra of the orthorhombic, tetragonal, and cubic phases of methylammonium lead iodide". In: *Physical Review B* 92.14 (2015), p. 144308.

[31] R. Gottesman et al. "Photoinduced reversible structural transformations in free-standing $CH_3NH_3PbI_3$ perovskite films". In: *The journal of physical chemistry letters* 6.12 (2015), pp. 2332–2338.

[32] M. A. Pérez-Osorio et al. "Vibrational properties of the organic–inorganic halide perovskite $CH_3NH_3PbI_3$ from theory and experiment: factor group analysis, first-principles

calculations, and low-temperature infrared spectra". In: *The Journal of Physical Chemistry C* 119.46 (2015), pp. 25703–25718.

[33] S. G. Motti et al. "Photoinduced emissive trap states in lead halide perovskite semiconductors". In: *ACS Energy Letters* 1.4 (2016), pp. 726–730.

[34] W. Kong et al. "Characterization of an abnormal photoluminescence behavior upon crystal-phase transition of perovskite $CH_3NH_3PbI_3$". In: *Physical Chemistry Chemical Physics* 17.25 (2015), pp. 16405–16411.

[35] C. Wehrenfennig et al. "Charge carrier recombination channels in the low-temperature phase of organic-inorganic lead halide perovskite thin films". In: *APL Materials* 2.8 (2014), p. 081513.

[36] K. Robinson, G. Gibbs, and P. Ribbe. "Quadratic elongation: a quantitative measure of distortion in coordination polyhedra". In: *Science* 172.3983 (1971), pp. 567–570.

[37] Y. Li, G. Zheng, and J. Lin. "Synthesis, Structure, and Optical Properties of a Contorted <110>-Oriented Layered Hybrid Perovskite: $C_3H_{11}SN_3PbBr_4$". In: *European Journal of Inorganic Chemistry* 2008.10 (2008), pp. 1689–1692.

[38] D. G. Billing and A. Lemmerer. "Synthesis, characterization and phase transitions in the inorganic-organic layered perovskite-type hybrids $[(C_nH_{2n+1}NH_3)_2PbI_4]$, n= 4,5 and 6". In: *Acta Crystallographica Section B: Structural Science* 63.5 (2007), pp. 735–747.

[39] D. B. Mitzi. "A layered solution crystal growth technique and the crystal structure of $(C_6H_5C_2H_4NH_3)_2PbCl_4$". In: *Journal of Solid State Chemistry* 145.2 (1999), pp. 694–704.

[40] A. Jaffe et al. "High-pressure single-crystal structures of 3D lead-halide hybrid perovskites and pressure effects on their electronic and optical properties". In: *ACS central science* 2.4 (2016), pp. 201–209.

[41] C. C. Stoumpos, C. D. Malliakas, and M. G. Kanatzidis. "Semiconducting tin and lead iodide perovskites with organic cations: phase transitions, high mobilities, and near-infrared photoluminescent properties". In: *Inorganic chemistry* 52.15 (2013), pp. 9019–9038.

[42] N. W. Thomas. "Crystal structure–physical property relationships in perovskites". In: *Acta Crystallographica Section B: Structural Science* 45.4 (1989), pp. 337–344.

[43] E. Mosconi et al. "Light-induced annihilation of Frenkel defects in organo-lead halide perovskites". In: *Energy & Environmental Science* 9.10 (2016), pp. 3180–3187.

[44] D. B. Straus et al. "Direct observation of electron–phonon coupling and slow vibrational relaxation in organic–inorganic hybrid perovskites". In: *Journal of the American Chemical Society* 138.42 (2016), pp. 13798–13801.

[45] M. Bonn et al. "Role of Dielectric Drag in Polaron Mobility in Lead Halide Perovskites". In: *ACS Energy Letters* 2.11 (2017), pp. 2555–2562.

[46] Y. P. Varshni. "Temperature dependence of the energy gap in semiconductors". In: *physica* 34.1 (1967), pp. 149–154.

[47] L. Ni et al. "Real-Time Observation of Exciton–Phonon Coupling Dynamics in Self-Assembled Hybrid Perovskite Quantum Wells". In: *ACS nano* 11.11 (2017), pp. 10834–10843.

[48] T. Ishihara. "Optical properties of low-dimensional materials". In: *World Sci Singapore* 288 (1995), pp. 288–339.

[49] J.-C. Blancon et al. "Strongly bound excitons in Ruddlesden-Popper 2D perovskites". In: *arXiv preprint arXiv:1710.07653* (2017).

[50] R. Elliott. "Intensity of optical absorption by excitons". In: *Physical Review* 108.6 (1957), p. 1384.

[51] M. de Jong et al. "Resolving the ambiguity in the relation between Stokes shift and Huang–Rhys parameter". In: *Physical Chemistry Chemical Physics* 17.26 (2015), pp. 16959–16969.

[52] J. Lee, E. S. Koteles, and M. Vassell. "Luminescence linewidths of excitons in GaAs quantum wells below 150 K". In: *Physical Review B* 33.8 (1986), p. 5512.

[53] F. D. Fuller and J. P. Ogilvie. "Experimental implementations of two-dimensional Fourier transform electronic spectroscopy". In: *Annual review of physical chemistry* 66 (2015), pp. 667–690.

[54] A. Tokmakoff. "Two-dimensional line shapes derived from coherent third-order nonlinear spectroscopy". In: *The Journal of Physical Chemistry A* 104.18 (2000), pp. 4247–4255.

[55] M. Yuan et al. "Perovskite energy funnels for efficient light-emitting diodes". In: *Nature nanotechnology* 11.10 (2016), p. 872.

[56] X. Zhang et al. "Influence of electron-phonon interaction on the optical properties of III nitride semiconductors". In: *Journal of Physics: Condensed Matter* 13.32 (2001), p. 7053.

[57] C. Duke and G. Mahan. "Phonon-broadened impurity spectra. I. Density of states". In: *Physical Review* 139.6A (1965), A1965.

[58] A. Gurskii and S. Voitikov. "Quantum defect approach for the effect of electron–phonon coupling on impurity recombination in semiconductors". In: *Solid state communications* 112.6 (1999), pp. 339–343.

[59] E. Rashba. "Optical spectra of phonons bound to impurity centers". In: *Soviet Journal of Experimental and Theoretical Physics* 44 (1976), p. 166.

[60] A. Davydov. *Theory of molecular excitons*. Springer, 2013.

[61] G. Batignani et al. "Probing Femtosecond Lattice Displacement upon Photo-carrier generation in Lead Halide Perovskite". In: *arXiv preprint arXiv:1705.08687* (2017).

[62] R. M. Hochstrasser and P. N. Prasad. "Phonon sidebands of electronic transitions in molecular crystals and mixed crystals". In: *The Journal of Chemical Physics* 56.6 (1972), pp. 2814–2823.

[63] D. Sapori et al. "Quantum confinement and dielectric profiles of colloidal nanoplatelets of halide inorganic and hybrid organic–inorganic perovskites". In: *Nanoscale* 8.12 (2016), pp. 6369–6378.

[64] M. Pope and C. E. Swenberg. *Electronic processes in organic crystals and polymers*. Oxford University Press on Demand, 1999.

[65] D. Emin. *Polarons*. Cambridge University Press, 2013.

[66] O. Selyugin and M. Smondyrev. "Phase transition and Padé approximants for Fröhlich polarons". In: *physica status solidi (b)* 155.1 (1989), pp. 155–167.

[67] T. Itoh et al. "Polaron and exciton-phonon complexes in CuCl nanocrystals". In: *Physical Review Letters* 74.9 (1995), p. 1645.

[68] M. Geddo and G. Iadonisi. "Polaronic effects on two-dimensional excitons". In: *Il Nuovo Cimento D* 12.12 (1990), pp. 1641–1650.

[69] K. Gauthron et al. "Optical spectroscopy of two-dimensional layered $(C_6H_5C_2H_4NH_3)_2PbI_4$ perovskite". In: *Optics express* 18.6 (2010), pp. 5912–5919.

[70] P. Moran. "Effects of Dynamic Lattice Distortions on the Structure of the F Band in the Cesium Halides". In: *Physical Review* 137.3A (1965), A1016.

[71] A. Manchon et al. "New perspectives for Rashba spin–orbit coupling". In: *Nature materials* 14.9 (2015), p. 871.

[72] Y. Zhai et al. "Giant Rashba splitting in 2D organic-inorganic halide perovskites measured by transient spectroscopies". In: *Science advances* 3.7 (2017), e1700704.

[73] V. I. Klimov. "Mechanisms for photogeneration and recombination of multiexcitons in semiconductor nanocrystals: Implications for lasing and solar energy conversion". In: *Journal of Physical Chemistry B* 110.34 (2006), pp. 16827–16845.

[74] T. Ishihara et al. "Dielectric confinement effect for exciton and biexciton states in PbI_4-based two-dimensional semiconductor structures". In: *Surface science* 267.1-3 (1992), pp. 323–326.

[75] T. Kondo et al. "Biexciton lasing in the layered perovskite-type material $(C_6H_{13}NH_3)_2PbI_4$". In: *Solid state communications* 105.4 (1998), pp. 253–255.

[76] Y. Kato et al. "Extremely large binding energy of biexcitons in an organic–inorganic quantum-well material $(C_4H_9NH_3)_2PbBr_4$". In: *Solid state communications* 128.1 (2003), pp. 15–18.

[77] J.-i. Fujisawa and T. Ishihara. "Excitons and biexcitons bound to a positive ion in a bismuth-doped inorganic-organic layered lead iodide semiconductor". In: *Physical Review B* 70.20 (2004), p. 205330.

[78] M. H. Elkins et al. "Biexciton Resonances Reveal Exciton Localization in Stacked Perovskite Quantum Wells". In: *The Journal of Physical Chemistry Letters* 8.16 (2017), pp. 3895–3901.

[79] Y. You et al. "Observation of biexcitons in monolayer WSe_2". In: *Nature Physics* 11.6 (2015), p. 477.

[80] I. Kylänpää and H.-P. Komsa. "Binding energies of exciton complexes in transition metal dichalcogenide monolayers and effect of dielectric environment". In: *Physical Review B* 92.20 (2015), p. 205418.

[81] M. Koziński, S. Garrett-Roe, and P. Hamm. "Vibrational spectral diffusion of CN- in water". In: *Chemical Physics* 341.1-3 (2007), pp. 5–10.

[82] K. W. Stone et al. "Exciton- Exciton Correlations Revealed by Two-Quantum, Two-Dimensional Fourier Transform Optical Spectroscopy". In: *Accounts of chemical research* 42.9 (2009), pp. 1452–1461.

[83] K. Hao et al. "Neutral and charged inter-valley biexcitons in monolayer $MoSe_2$". In: *Nature communications* 8 (2017), p. 15552.

[84] G. Moody et al. "Coherent coupling of excitons and trions in a photoexcited CdTe/CdMgTe quantum well". In: *Physical review letters* 112.9 (2014), p. 097401.

[85] D. Karaiskaj et al. "Two-quantum many-body coherences in two-dimensional Fourier-transform spectra of exciton resonances in semiconductor quantum wells". In: *Physical review letters* 104.11 (2010), p. 117401.

[86] D. B. Turner and K. A. Nelson. "Coherent measurements of high-order electronic correlations in quantum wells". In: *Nature* 466.7310 (2010), pp. 1089–1092.

[87] L. Yang and S. Mukamel. "Two-dimensional correlation spectroscopy of two-exciton resonances in semiconductor quantum wells". In: *Physical review letters* 100.5 (2008), p. 057402.

[88] J. Pollmann and H. Büttner. "Effective Hamiltonians and bindings energies of Wannier excitons in polar semiconductors". In: *Physical Review B* 16.10 (1977), p. 4480.

[89] E. O. Kane. "Pollmann-Büttner variational method for excitonic polarons". In: *Physical Review B* 18.12 (1978), p. 6849.

[90] A. R. Srimath Kandada and A. Petrozza. "Photophysics of hybrid lead halide perovskites: the role of microstructure". In: *Accounts of chemical research* 49.3 (2016), pp. 536–544.

[91] I. Carusotto and C. Ciuti. "Quantum fluids of light". In: *Reviews of Modern Physics* 85.1 (2013), p. 299.

Chapter 6

Conclusions

Sustainability of our society requires technological developments towards improved energy conversion efficiencies and material consumption, which implies the need for highly optimized material systems. Hybrid semiconductors aim to combine the versatility of organic compounds with the advantage of inorganic materials to tune and engineer their optoelectronic properties. Since their discovery for photovoltaic applications, hybrid organic-inorganic lead halide perovskites have emerged as attractive materials among solution-processed semiconductors with excellent light harvesting and emission capabilities, prerequisites for high efficiency optoelectronic technologies. They form an intrinsically complex material system with a rich defect landscape and various types of interactions between the organic and inorganic constituents, affecting their electro-optical properties. Therefore, a clear understanding of the intricate inter-play of different contributions is crucial to control and engineer the material properties and expedite perovskite based technologies. The spectroscopic studies presented in this PhD thesis are part of the current scientific effort to elucidate the structure-function relationship in hybrid perovskites with the objective to disentangle their inherent physics. In the following the important conclusions from each chapter are summarized.

- **The role of defects in hybrid lead bromide perovskites:** an appealing aspect, contributing to the success of this class of materials is their facile synthesis from solution which exposes the material to a variety of external factors, i. a. influencing their defectivity. To understand the nature of defects and how they affect the charge carrier dynamics in the material is of fundamental importance for device optimization. Using ECPL spectroscopy, a technique inherently sensitive to the nonlinear contributions to the carrier recombination process, we could quantitatively assess the influence of unintentional doping and defects on the carrier dynamics in three exemplary lead bromide perovskite systems. We demonstrated that the predominance of energetically deep or shallow defects in $MAPbBr_3$ films depends on the employed synthesis route. Situated 20 meV below the conduction band, shallow defects can dope the material and alleviate the effects of nonradiative quenching. We provided quantitative models to fit the specific ECPL dynamics and showed, that the excitation dynamics of colloidal $CsPbBr_3$ nanocrystals

are mainly influenced by ultrafast Auger recombination at higher excitation densities. Hitting the limit of optical spectroscopy, refined information about the defect related energetic landscape and the identification of the "chemical" origin of defect states in the material demand for more sophisticated techniques. In the future, a combined spectroscopic investigation via photoelectron emission microscopy, ECPL and time-of flight spectroscopy could fill the current gap and provide in depth understanding of defect physics and the correlated carrier dynamics in this class of materials.

- **ASE and dual-phase architecture in $MAPbI_3$:** The main loss channel for the excited state population in $MAPbI_3$ pervoskites at high excitation densities is due to non-radiative Auger recombination, which constitutes a major obstacle for lasing. We used TA spectroscopy to investigate the effects of population transfer between orthorhombic and tetragonal domains, which form just below the structural phase transition temperature in the material and demonstrated that efficient transfer can lower the threshold for amplified spontaneous emission. Our finding imply design principles, similar to the strategies employed in quantum well lasers, of relocating the photo carrier population to mitigate the effect of Auger interactions and suggest that engineering host-guest structures constitutes an efficient approach to realize gain media in this class of materials. Integrated in high quality factor resonators they could pave the way towards electrically pumped perovskite based laser.

- **The role of structure in the optical properties of 2D perovskites:** 2D hybrid lead halide perovskites are self-assembled organic-inorganic quantum-well structures with strongly bound excitons, a desirable characteristic for photonic and quantum optoelectronic applications. In this first part we were addressing the origin of two peculiar phenomena appearing in the emission and absorption spectra of 2D HOIPs, namely broadband photoluminescence, showed by some compounds of this family and the fine-structure appearing in the optical absorption at lower temperatures. We gave evidence that deformations of the inorganic cage can lower the defect formation energies and promote charge self-trapping in the materials, giving rise to broadened photoluminescence bands. We provided a quantitative description of the spectral absorption lineshape by considering strong contributions due to exciton-lattice coupling. Using temperature dependent absorption measurements and modeling with a modified two-dimensional Wannier exciton formalism we could identify polaronic effects on the excitonic spectral signatures, due to coupling with localized vibrational and delocalized phonon modes. Our discussion stresses the need for a in depth investigation of the exciton-lattice coupling effects in this class of materials to develop a new theoretical framework for excitons in these systems.

- **The role of structure in the excitonic many-body effects of 2D perovskites:** After demonstrating how dynamic and static structural disorder can influence the linear optical properties of 2D HOIPS we investigated their effect on the excitonic correlations in a prototypical 2D perovskite, $(PEA)_2PbI_4$. We showed, that biexcitons are stable at room temperature and form the predominant population at high excitation densities. By means of 2D coherent spectroscopy, we measured their binding energy at liquid helium and ambient temperatures and demonstrated, that dynamic disorder in the material leads to a decrease in binding energy by over 20%. Our work highlights the urgency to incorporate and conceptualize the concept of disorder to extend the relevance of this class of materials towards applications beyond photovoltaics.

Disseminations

List of publications

[1] **S. Neutzner**, F. Thouin, D. Cortecchia, A. Petrozza, C. Silva, and A. R. S. Kandada . *Exciton-polaron spectral structures in two dimensional hybrid lead-halide perovskites*. manuscript in preparation (2018).

[2] F. Thouin ‡, **S. Neutzner** ‡, D. Cortecchia, V. A. Dragomir, C. Soci, T. Salim, Y. M. Lam, R. Leonelli, A. Petrozza, A. R. S. Kandada, C. Silva.
Stable biexcitons in two-dimensional metal-halide perovskites with strong dynamic lattice disorder.
Physical Review Materials, accepted. arXiv:**1712.04733** (2018).

[3] D. Cortecchia, **S. Neutzner**, A. R. S. Kandada, E. Mosconi, D. Meggiolaro, F. De Angelis, C. Soci, A. Petrozza.
Broadband emission in two-dimensional hybrid perovskites: the role of structural deformation.
Journal of the American Chemical Society **139**, 39-42 (2017).

[4] C. Tao, J. Van Der Velden, L. Cabau, N. F. Montcada, **S. Neutzner**, S. Kandada, A. Ram, S. Marras, L. Brambilla, M. Tommasini.
Fully solution-processed n-i-p-like perovskite solar cells with planar junction: how the charge extracting layer determines the open-circuit voltage.
Advanced Materials **29** (2017).

[5] P. J. Cegielski, **S. Neutzner**, C. Porschatis, H. Lerch, J. Bolten, S. Suckow, A. R. S. Kandada, B. Chmielak, A. Petrozza, T. Wahlbrink.
Integrated perovskite lasers on a silicon nitride waveguide platform by cost-effective high throughput fabrication.
Optics Express **25**, 13199-13206 (2017).

[6] M. De Bastiani, G. Dell'Erba, M. Gandini, V. D'Innocenzo, **S. Neutzner**, A. R. S. Kandada, G. Grancini, M. Binda, M. Prato, J. M. Ball.
Ion migration and the role of preconditioning cycles in the stabilization of the j-v characteristics of inverted hybrid perovskite solar cells.
Advanced Energy Materials **6** (2016).

[7] **S. Neutzner**, A. R. S. Kandada, G. Lanzani, A. Petrozza.
A dual-phase architecture for efficient amplified spontaneous emission in lead iodide perovskites.
Journal of Materials Chemistry C **4**, 4630-4633 (2016).

[8] A. R. Srimath Kandada ‡, **S. Neutzner** ‡, V. D'Innocenzo, F. Tassone, M. Gandini, Q. A. Akkerman, M. Prato, L. Manna, A. Petrozza, G. Lanzani.
Nonlinear carrier interactions in lead halide perovskites and the role of defects.
Journal of the American Chemical Society **138**, 13604-13611 (2016).

[9] J. P. C. Baena, L. Steier, W. Tress, M. Saliba, **S. Neutzner**, T. Matsui, F. Giordano, T. J. Jacobsson, A. R. S. Kandada, S. M. Zakeeruddin.
Highly efficient planar perovskite solar cells through band alignment engineering.
Energy & Environmental Science 8, 2928-2934 (2015).

[10] G. Grancini, M. Binda, **S. Neutzner**, L. Criante, V. Sala, A. Tagliaferri, G. Lanzani.
The role of higher lying electronic states in charge photogeneration in organic solar cells.
Advanced Functional Materials **25**, 6893-6899 (2015).

[11] C. Tao, **S. Neutzner**, L. Colella, S. Marras, A. R. S. Kandada, M. Gandini, M. De Bastiani, G. Pace, L. Manna, M. Caironi.
17.6 % stabilized efficiency in low-temperature processed planar perovskite solar cells.
Energy & Environmental Science **8**, 2365-2370 (2015).

‡authors contributed equally

Conference presentations

[1] *Stable biexcitons in two-dimensional metal-halide perovskites with strong dynamic lattice disorder.*
oral, MRS Boston, 26th of November-1st of December, 2017, Boston (US) .

[2] *Photo-Induced Mixing of Excitonic Spin States in Ruddlesden-Popper Lead Halide Perovskites.*
oral, PSCO conference, 18-20 September, 2017, Oxford (UK) .

[3] *Photo-Induced Mixing of Excitonic Spin States in Ruddlesden-Popper Lead Halide Perovskites.*
oral, Optical probes conference, 19-23 June, 2017, Québec (CA) .

[4] *Role of Structural Distortion in Photoluminescence Broadening of Hybrid Perovskites.*
poster, PSCO conference, 26-28 September, 2016, Genova (IT) .

[5] *Non-linear Carrier Interactions in Lead Halide Perovskites and the Role of Defects.*
oral, PSCO conference, 26-28 September, 2016, Genova (IT) .

Acknowledgements

"To try to make a model of an atom by studying its spectrum is like trying to make a model of a grand piano by listening to the noise it makes when thrown downstairs."

– Anonymous (in: The British Journal of Radiology: The Journal of the Röntgen Society. Röntgen Society section, Volumes 20-21, Wertheimer, 1924)

Science is a team achievement on various instances and I am deeply indebted to all people who supported me, from whom I learned and all those who simply contributed to a warm and pleasant working environment. Here, I would like to express my sincere gratitude to everybody, who made this PhD work not only possible but these three years at CNST also enjoyable.

I am particularly grateful to my supervisor Dr. Annamaria Petrozza for believing in my capabilities despite my non-linear curriculum vitae, welcoming me in her group and guiding me among the "Petrozzcopists". At this point, I would also like to thank Prof. Guglielmo Lanzani for inspiring spectroscopy discussions (featuring Francesco Tassone) and for giving me the opportunity to pursue my PhD at CNST.

I am grateful to all my present and former colleagues from the "dark side", aka spectroscopy crew. First and foremost, I would like to thank Ajay for his friendship, great support, encouragement and unbreakable enthusiasm for science. He had been an amazing teacher and mentor for his first "femto lab guinea pig" and made me aware of the little treasures, buried in apparently useless piles of data. Many thanks to Ilaria, Silvia and Alex, for lending me a helping hand when desperately needed and enduring my ups and downs during this PhD. And of course I am grateful to all other (and former) spectroscopy members, Marcelo, Valerio, Giuseppe, Tanja, Egle and Gabriel for a great working atmosphere with the right amount of humor.

A spectroscopist would be nothing without good samples. Therefore, I would like to thank all my colleagues from the "bright side", aka device crew for answering patiently my naive questions about rules and instrumentation whenever I got "lost" in ARCO and in particular Daniele, Marina and Chen for enduringly providing all kind of sample variations and replacements.

Many thanks to all colleagues at CNST for the pleasant environment, especially to the permanent staff, Alessandra (x2), Silvia, Tessa and the technicians, Luca, Martina, Stefano, Enrico and Andrea for managing the work life around the lab.

Acknowledgements

Without the input of and collaborations with other groups, crucial parts of this thesis would have never been written. Therefore, I am most grateful to Prof. Carlos Silva and his group, in particular Félix for the memorable time in Montréal and the amazing team work and I would also like to thank all members of the SYNCHRONICS network.

Finally, I am deeply indebted to my family, no words can express my gratitude for the constant support and love they have given me in all these years.

Milano, February 2018
Stefanie Claudia Neutzner